Politecnico di Torino

Computer Engineering – Automation and Intelligent Cyber-physical Systems
A.y. 2020/2021
Graduation Session October 2021

A Meteoroid Impact Recovery Control System for the LISA Gravitational Wave Observatory

Supervisors:
Prof. Carlo Novara
Dr. Simone Vidano

Candidate:
Mario Virdis

Declaration

I hereby declare that this Thesis with title "A Meteoroid Impact Recovery Control System for the LISA Gravitational Wave Observatory" is the result of my own work and has been carried out under the guidance of my supervisors Prof. Carlo Novara and Dr. Simone Vidano. Every reference to work or previously existing results made by others have been given due acknowledgement and every reference is explicitly reported.

Mario Virdis

Abstract

Gravitational waves are ripples in the fabric of space-time, that propagate almost undisturbed throughout the universe. These are generated by some of the most energetic and violent processes that take place in the universe, such as colliding black holes, supernovae, colliding neutron stars and more. The scientific community is measuring gravitational waves by using large scale interferometers. An Earth-based large scale interferometer basically consists of a building with two very long arms (in the case of LIGO 4km) that contain vacuum pipes where light can travel and be reflected by extremely accurate mirrors. The main issue with these type of detectors is that the Earth's seismic activity affects their measurement spectrum below 10 Hz, and it is below this frequency where most of the interesting information about celestial events is contained. To solve this inherent limitation of ground interferometers an alternative solution has been proposed: a laser interferometer space antenna (LISA).

LISA is a space–based gravitational wave detector, confirmed by ESA to be the third large class mission of the Cosmic Vision program. This kind of detection requires extremely high accuracy from laser–based sensor measurements; therefore impacts with meteoroids constitute a real threat to the mission, causing a waste of time and resources. In this work, this problem is addressed by comparing different possible recovery control systems. The recovery control system is composed by a set of controllers, each of which solves a specific recovery task. These tasks are the outcome of a preliminary data analysis of the impact data provided by ESA. In this data analysis a Spacecraft of the LISA system is modeled as a state machine and each impact–induced state transition is considered. Two main PID control recovery systems are selected, that make use of different sensor configurations: the first one requires the Constellation Acquisition Sensor, whereas the other can function without, but requires a model of the solar pressure disturbance. Finally, a set of complete impact simulations is performed in order to validate both recovery control systems.

Dedication

Questa tesi, come molti dei miei obiettivi raggiunti fin'ora, non sarebbe stata possibile senza l'aiuto di molte persone.

Prima di tutto, un ringraziamento speciale a mia madre Giovanna e mia nonna Lucia che mi hanno sempre supportato emotivamente ed economicamente, e mi hanno aiutato a superare diversi ostacoli incontrati durante il mio percorso. Un ringraziamento anche a mia sorella Lucia con cui ho la certezza di poter sempre fare una bella conversazione e che mi sopporta anche quando molti non lo farebbero. Anche a mio nonno Michele che mi fa sempre ridere e che dovrei ringraziare per aver ereditato la sua intelligenza, per lo meno stando a quanto dice lui.

A Orsola, che è stata sempre al mio fianco per gli ultimi due anni, avendo la pazienza di ascoltare tutti i miei discorsi sulle cose che faccio ed il cui supporto emotivo è stato fondamentale nel concludere questo lavoro.

Ultimi ma non ultimi, non avrei potuto concludere niente senza l'aiuto e i consigli dei miei migliori amici. Di quelli che conosco da sempre come Gianna, Nick, Daniel, Valeriano, Zambe, con cui sono cresciuto. Un grazie particolare anche ad Alberto, Niccolò, Ale "Totti", Roberto, con cui ho condiviso alcuni degli anni più belli e difficili della mia vita e che mi hanno aiutato a migliorare continuamente. Un grazie anche a Bianca, Lucrezia e Matilde per le belle serate passate insieme e per avermi ospitato molte volte.

This Thesis, like most of my achievements until now, would not have been possible without the help of many people.

First of all, a special thank you, to my mother Giovanna and my grandmother Lucia that have always supported me, emotionally and financially, and helped me overcome every obstacle encountered. A thank you also to my sister Lucia with whom I can always count on having a good talk and that tolerates me when most would not. Also to my grandfather Michele who always makes me laugh and who I should thank for having inherited his intellect, at least according to him.

To Orsola, that has been staying always by my side for the last two years, having the patience to listen to all the talks about the things I do and whose emotional support was fundamental in finishing this work.

Last but not least, nothing could have been accomplished without the amazing help and advice from my greatest friends. From Gianna, Nick, Daniel, Valeriano, Zambe, that I grew up with. A special thank you also from Alberto, Niccolò, Ale "Totti", Roberto, with whom I shared some of the most amazing and difficult years of my life and that helped me improve continuously. A thanks also to Bianca, Lucrezia and Matilde for all the funny moments together and for hosting me many times.

Acknowledgements

Fundamental for this work were the advice and guidance from my supervisors Dr. Simone Vidano and Prof. Carlo Novara, that I want to thank.

This work was carried out in collaboration with the European Space Agency/ESTEC, that provided us with the data and other useful insights. The view expressed in this work cannot be taken as the official position of the European Space Agency.

Contents

Acronyms

ADC	Analog to Digital Converter
AOCS	Attitude and Orbit Control System
BoL	Begin of Life
CAS	Constellation Acquisition Sensor
CRF	Constellation Reference Frame
DCM	Direction Cosine Matrix
DFACS	Drag Free Attitude Control System
DoF	Degree of Freedom
DWS	Differential Wavefront Sensing
EoL	End of Life
EoR	End of Recovery
EKF	Extended Kalman Filter
ESA	European Space Agency
GW	Gravitational Waves
IRF	Inertial Reference Frame
LIGO	Laser Interferometer Gravitational-Wave Observatory
LISA	Laser Interferometer Space Antenna
LTI	Linear Time–Invariant
MC	Monte Carlo
MPS	Micro Propulsion System
OMS	Optical Measurement System
OMU	Optical Measurement Unit
PD	Proportional Derivative
PF	Pathfinder
PID	Proportional Integral Derivative
SC	Spacecraft
SRF	Spacecraft Reference Frame
TM	Test Mass

1 | Introduction

Gravitational waves are ripples in the fabric of space-time, that propagate almost undisturbed throughout the universe. These are generated by some of the most energetic and violent processes that take place in the universe, such as colliding black holes, supernovae, colliding neutron stars and more.
For this reason GW provide a large amount of information about celestial bodies and gravity itself, therefore they are of major interest for the scientific community.

Their existence was first predicted by Einstein in 1916 as part of a much larger theory, known as General Relativity. A first proof of their existence arrived in 1974 by two astronomers observing a binary pulsar and since then different researchers found the same type of evidence, but still of an indirect and mathematical nature, not from direct sensing.

Direct measurement of GW was not possible until 2015, when LIGO physically measured undulations in space-time caused by gravitational waves generated by two colliding black holes 1.3 billion light-years away.

1.1 The LISA Observatory

The detection of gravitational waves is an extremely difficult task that requires incredible precision. While the events that generate them can be catastrophic and violent, the huge distances that divide the location of measurement from where the event itself took place, make the received signals extremely small.

Detecting GW means being able to measure a variation in length of one part in 10^{21}, that is the equivalent of measuring a variation equal to the thickness of a human hair of the distance between Earth and Alpha Centauri [2].

The scientific community is measuring gravitational waves by using large scale interferometers. An Earth-based large scale interferometer basically consists of a building with two very long arms (in the case of LIGO 4km) that contain vacuum pipes where light can travel and be reflected by extremely accurate mirrors.

The main issue with these type of detectors is that the Earth's seismic activity affects their measurement spectrum below 10 Hz, and it is below this frequency where most of the interesting information about celestial events is contained. Detecting activity in this low frequency band could shed light on some of the most fundamental questions of astrophysics and cosmology, such as the formation of the first massive black holes and the nature of gravity near them [7, p. 6].

To solve this inherent limitation of ground interferometers an alternative solution has been proposed: a laser interferometer space antenna. This antenna consists of a set of three spacecrafts orbiting in a triangular constellation. Each edge of the constellation is a laser communication between two of the spacecrafts. The constellation orbits the sun

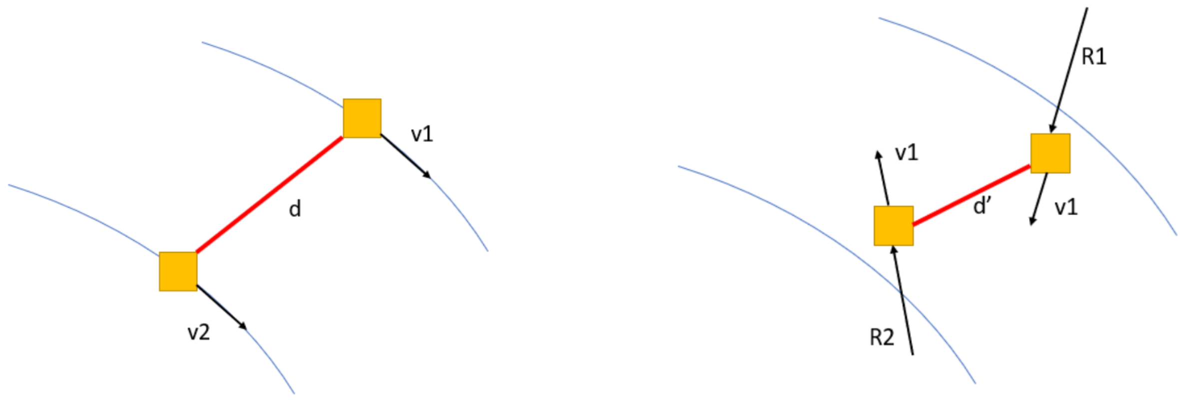

(a) Geodesics of two Test Masses

(b) Two Test Masses under disturbance

Figure 1.1: TM Geodesics

trailing the Earth by approximately 20°.

In 2015 LISA Pathfinder was launched: a preliminary system that allowed to study the requirements of the involved technologies and allowed to collect a lot of useful real data until 2017. The success of LISA Pathfinder, together with the first observations of gravitational waves by means of ground-based interferometers, resulted in the selection of LISA as the third large class mission in the ESA Cosmic Vision program. Hence, as part of the mission preparation, ESA started several development studies such as the system Phase-A and the LISA DFACS (Drag Free and Attitude Control System) design.

1.2 Wave Detection

Gravitational waves are undulations that propagate in the fabric of space-time. According to General Relativity two free falling masses will follow a path in space-time known as *geodesic*, a path on a curved hypersurface. A gravitational wave that happens to cross the geodesics of two free falling masses will perturb their relative distance: it is by measuring this tiny variation that one can detect them.

The task of detection can be seen as composed of two different problems: the first is the problem of measuring the relative distance between two masses with the required level of accuracy; the second is the task of ensuring that the two masses are actually free falling, that is, they are not subjected to any external force or disturbance.

1.2.1 Principles behind space detectors

In the simplified case of a one-arm space detector, there are two masses, also called *Test Masses* in the specific context of LISA, travelling free of every disturbance, along their respective *geodesics*, as predicted by General Relativity. In general there cannot be a truly drag free orbit of the two masses, because there will always be a certain amount of disturbances acting on them, e.g. solar pressure, noise from actuators. The direction along which lies the line connecting the two masses' center of mass is called *drag free dimension* and is shown in Fig. 1.1a, it is along that direction that the measurement has to be as accurate as possible.

External sources of disturbance could shadow the tiny variations caused by the GW themselves, making the detection impossible. That is why an active disturbance rejection device is needed in order to make the masses' movements as similar as possible to the drag free ideal case. Each of the spacecrafts employed in the LISA system serve a twofold purpose: it measures very accurately the distance between the two TMs along the drag free direction and it acts as an active disturbance rejection system. If the disturbance rejection system is accurate within the required performance along the drag free direction, then every other variation of the relative distance of the two TMs is due to gravitational waves.

The simplified case of only two free falling masses has already been tested for two years by the LISA Pathfinder mission. In this configuration only one spacecraft has been employed, it contained two test masses inside the spacecraft itself, floating in small vacuum chambers. All the science was done inside the Technology Package, shown in Fig.1.2a.

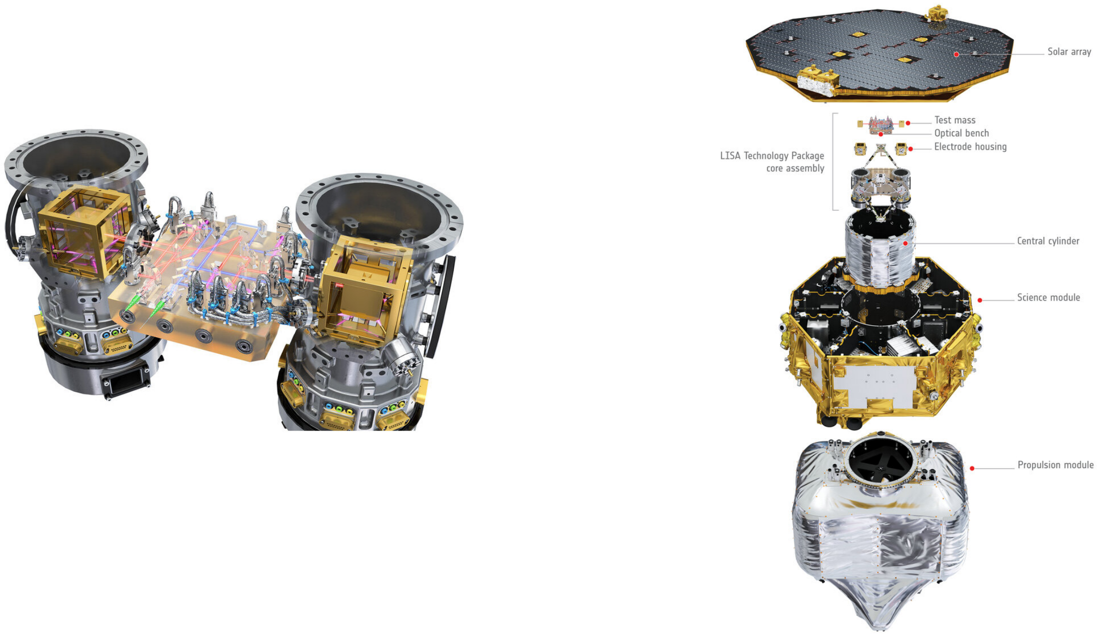

(a) Technology Package (b) Spacecraft

Figure 1.2: LISA Pathfinder [1]

If tiny variations in distance are to be measured with such high accuracy then very sophisticated and advanced tools are required. In the context of gravitational waves advanced versions of the Michelson interferometer are employed.

The principle behind this class of measurement tools is simple: they measure the difference in round-trip time of two light beams, travelling in non-parallel directions.

1.3 The DFAC System

The LISA observatory is much more complex than the simplified case discussed above. First of all, in LISA there are three different spacecrafts orbiting in a triangular configuration around the sun, trailing the Earth by about 20°, where the average length of one edge is approximately $2.5 \cdot 10^6$ km, as shown in Fig. 1.3b. Each SC contains two optical assemblies that have the vacuum cage with the TM on one end. The OA also handles the

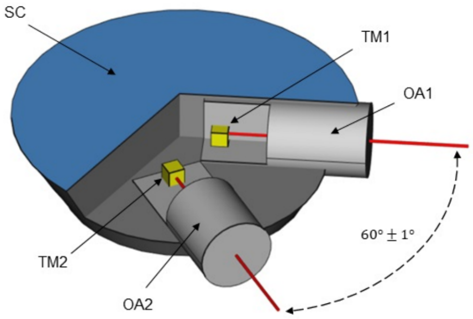

(a) Model of a LISA spacecraft

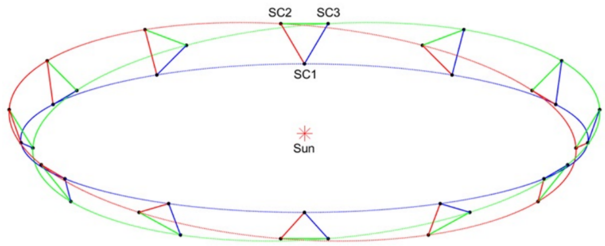

(b) LISA orbit

Figure 1.3: LISA System

laser link that forms the edge of the constellation triangle and is equipped with extremely accurate sensors that are able to measure azimuth and elevation of the incoming laser beams, generated by the other two SCs.

At the inner end of the OA there is a sealed module called Gravity Reference System, that contains a small cubical vacuum cage were the TM is kept suspended by six electrodes placed in pairs in correspondence of each of the cage's surfaces. These electrodes act both as actuators and sensor of the TM's attitude and position inside the cage. A model of the whole SC is illustrated in Fig. 1.3a

After being brought in orbit, this complex system goes through different mission phases:

1. **Test Mass Release**
   The Test Mass is initially kept fixed to the cage by some metal pins. During this phase these pins are removed and the TM has to be suspended, using the electrostatic field generated by the GRS electrodes. In addition the controller has also to maintain the spacecraft's attitude.

2. **Constellation Acquisition**
   The three spacecrafts have to perform some attitude maneuvers in order to establish the laser links between each other's optical assemblies.

3. **Drag Free**
   This is the final mode where the actual detection process takes place. During this phase the controller has to keep the constellation by controlling the attitude of the spacecraft and act as a noise shield along the drag free direction for both TMs at the same time.

The *DFACS* is the controller that handles the main and last mission phase with a duration of several years. The main disturbances that it has to reject are solar pressure, meteoroid impacts and various noises injected from sensors and particularly from actuators. By using GRS electrodes it can control directly the Test Mass' attitude and position along all dimensions except for the drag free dimension. For this last dimension it has to use the thrusters mounted on the spacecraft sides, that is, it has to move itself around the Test Mass and cannot act upon it directly. This is because GRS electrodes are too noisy and they introduce tidal accelerations that cannot be present in the data coming from the interferometer.

One last task that the DFACS has to perform is the correct pointing of the optical assemblies. This comes from the fact that the constellation triangle has breathing angles. This means that in order to maintain the communication with the other two SCs of the formation, it is not enough to keep the OAs in a fixed position, with a nominal angle of 60°, but instead the angle has to vary slightly during the whole mission, with a range of $\pm 1^{\circ}$.

1.4 Objectives of this study

This work is based on an already developed and tested system of controllers for the three different mission phases previously described. The detailed work can be found in [3]. That preliminary study contains the description of the whole system, review of the literature and extensive testing of the nonlinear models and of the mission controllers, including the *DFACS*.

The need to study the effects of meteoroid impacts on the LISA system arose after the ESA provided extensive data on meteoroids impacts, that can happen during the LISA orbit around the sun. The DFACS designed in [3] is a linear H∞ controller that can guarantee the required performances. Although it was accurately designed, tested and tuned and thus provided a very good performance, it was still a linear controller that worked best around the working point. After doing extensive simulations the results showed that for some particularly intense impacts the system was unstable, causing the satellite to spin excessively, making it lose the established laser links.

When a LISA spacecraft loses the links, it has to enter in *Constellation Acquisition* phase again and the process of acquiring the constellation is very slow and requires several hours. Considering the frequency at which impacts could happen, the final effect of leaving the system as is, would be that of spending most of the mission time (and money) in reacquiring constellation, instead of performing science, the goal of the whole mission.

The general objectives of this study can be described as follows:

1. Analysis of the impact data provided by ESA and research of stability and performance boundaries by means of simulations;

2. Design and implementation of a solution. This will lead to the creation of a controller that will be integrated in the system of controllers provided in [3] and will operate to assist the already designed DFACS;

3. Testing and validation of the combined system by performing a set of simulations and analysis of the results.

2 | LISA Spacecraft

In this Chapter the detailed structure of a LISA spacecraft is presented. All the details were extracted from the work [3] and works referenced by it. It is important to remember that during the present study the system is still under development (only Phase A was completed), thus, a complete description of all the physical components is not available. Some of them are known thanks to the LISA Pathfinder mission, that provided useful information. In particular, for those components also noise and uncertainty ranges are available, allowing for a more accurate modelling and control.

The spacecraft used in LISA is composed of different modules and subsystems:

1. Micro Propulsion System
2. Optical Measurement System
3. Gravity Reference System
4. Star Tracker
5. Constellation Acquisition Sensor

The latest concept available [12] can be modelled as a truncated cone section with a solar panel of area $14\,\mathrm{m}^2$ on the upper surface.

The sketched structure of the SC is shown in Fig. 1.3a, where in particular the two optical assemblies, with their respective TMs, are highlighted. The incoming laser beams are also shown, reflecting off the lateral surfaces of the cubic masses. The mass of the whole SC will vary during the whole mission, because of propellant consumption. The estimated values are 1500 kg at Begin of Life and 1360 kg at End of Life. In Table 2.1 the nominal mass and inertia parameters of the main parts are reported.

2.1 Micro Propulsion System

Detailed information is available about the MPS used in the spacecraft employed during the LISA Pathfinder mission. The configuration consisted in six thrusters grouped in three pods, that were mounted 120° apart on the lateral surface of the science module. The propulsion was obtained by expelling cold nitrogen gas. No thrusters were pointed towards the $+z$ direction, because in order to reduce propellant consumption the solar pressure was exploited as a virtual thruster. Nonetheless this reduced also the actuation authority of the MPS, that is, the system was not able to directly provide a thrust directed in the $-z$ direction. The system is shown in Fig. 2.1.

The LISA SC is three times more massive with respect to the one of LISA PF, so the LISA MPS will be able to provide more thrust than the previous propulsion system. In

Quantity	Value
SC Mass	1500 kg BoL – 1360 kg EoL
SC Inertia	$J_{\mathrm{BoL}} = \begin{bmatrix} 800 & 13 & 10 \\ 13 & 800 & 12 \\ 10 & 12 & 1000 \end{bmatrix} \mathrm{kgm}^2$ $J_{\mathrm{EoL}} = \begin{bmatrix} 778 & 11 & 6 \\ 11 & 751 & 11 \\ 6 & 11 & 953 \end{bmatrix} \mathrm{kgm}^2$
OA Mass OA Inertia OA Stiffness OA Damping	$71\,kg$ $17\,\mathrm{kgm}^2$ 90000 Nm/rad 80 Nms/rad
OA Mounting point from barycenter	36 cm
TM Mass	1.96 kg
TM Inertia	$J_{\mathrm{TM}} = \begin{bmatrix} 0.6912 & 0 & 0 \\ 0 & 0.6912 & 0 \\ 0 & 0 & 0.6912 \end{bmatrix} \cdot 10^{-3}\,\mathrm{kgm}^2$

Table 2.1: Spacecraft inertia and mass nominal values

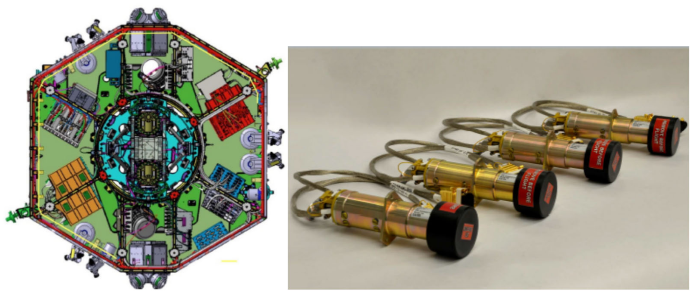

Figure 2.1: LISA PF MPS [16]

addition, in every lateral pod there will also be one of the three thrusters pointed in the $+z$ direction, in order to increase the actuation authority and facilitate the rejection of disturbances that could make the SC drift out of its orbit.

The obtained output resolution was $1\,\mu$N with an estimated delay within 300 ms, as reported in [15] and the forces recorded by the AOCS were, in general, within $\pm$ 5% of the commanded values. The response of the MPS is not immediate, but it behaves like a first/second order system.

The noise of the LISA PF MPS was reported in [15] and in [13] and the corresponding frequency plots are shown in Fig. 2.2
In Table 2.2 all the available parameters from ESA are summarized.

2.2 Optical Measurement System

The optical subsytem of a LISA SC is composed of two telescopes mounted at a nominal angle of 60° with the inner side near to the SC's center. The goal of this system is to

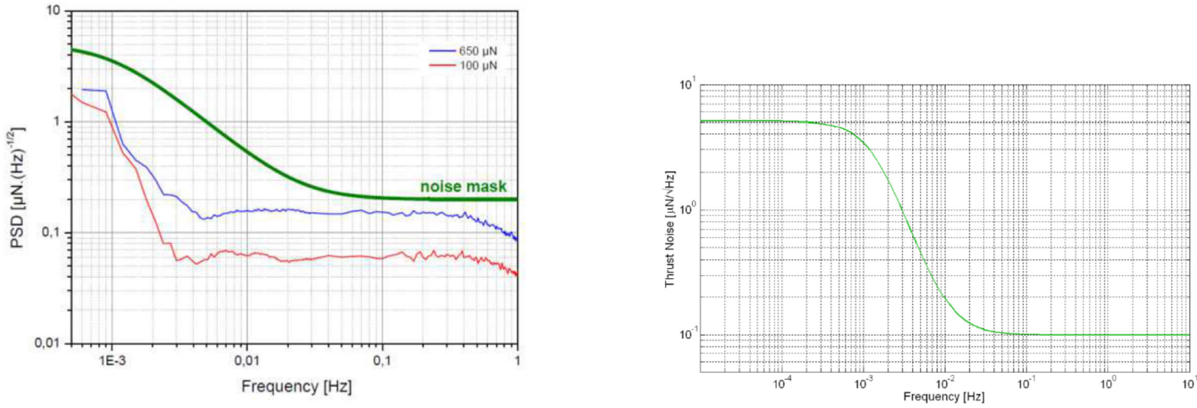

(a) Noise Mask as reported in [15] (b) Noise Mask as reported in [13]

Figure 2.2: LISA PF MPS Noise

Measurement	Value	
Maximum thrust	$500\,\mu$N	
Minimum thrust	$1\,\mu$N	
Thrust resolution	$0.3\,\mu$N $1\,\mu$N	$(1-100\,\mu\text{N})$ $(100-500\,\mu\text{N})$
Bias and linearity error	$0.5\,\mu$N $2\,\mu$N	$(<4\,\mu\text{N})$ $(>4\,\mu\text{N} \wedge <150\,\mu\text{N})$
Response time at 95% of thrust	<2 s	
Thrust overshoot	2% of steady state	
Thrust direction bias	0.5°	
Thrust update rate	10 Hz	
Noise	Figure 2.2	

Table 2.2: Parameters of LISA PF MPS

emit a laser beam, to receive the incoming laser beam from the other SCs and to perform the interferometry and angle-of-arrival measurements. In order to collect this data the laser needs to reflect on the Test Mass contained inside the GRS, located behind each telescope. An Optical Measurement Unit is a device that is interposed between the GRS and the telescope, that comprises different parts:

- *Reference Laser Unit* that generates the laser beam;
- *Laser Modulator* that splits the laser beam into many beams;
- *Optical Bench* that contains the set of mirrors and performs laser interferometry;
- *Phasemeter* the unit responsible for computing the phase of the received signals by means of photodiodes;
- *Data management unit* an on-board computer interfaced to the system with an ADC.

The overall structure is shown in Fig. 2.3.
Functionally the OMU is able to compute the following quantities:

- azimuth and elevation angles of the incoming laser beam by means of a technique called Differential Wavefront Sensing;
- pitch and yaw of the Test Mass reflecting the laser beam, also by DWS;
- the distance between the two OMUs on the two spacecrafts or inter-spacecraft distance;
- the local distance between the OMU and the Test Mass in the adjacent GRS or local TM-spacecraft distance.

The total distance between the two Test Masses along any arm can be computed as the sum of one inter-spacecraft distance and the two corresponding TM-spacecraft distances. The DWS technique provides very accurate measurements of the angles of the incoming laser beams, data that can be used to control the SC's attitude with respect to the constellation during the science mode, phase during which the Star Tracker system is turned off on purpose.

Measurement ranges and noises affecting this module, that is planned to be used in LISA, were provided by ESA in [13] and are listed in Tab. 2.3.

Measurement	Range	Noise Spectral Density
Local SC–TM distance along drag free dim.	$100\,\mu$m	$1.5\,\frac{\text{pm}}{\sqrt{\text{Hz}}}\sqrt{1+\left(\frac{2\,\text{mHz}}{f}\right)^4}$
Inter-spacecraft distance along drag free dim.	–	$2.25\,\frac{\text{pm}}{\sqrt{\text{Hz}}}\sqrt{1+\left(\frac{2\,\text{mHz}}{f}\right)^4}$
DWS angles: TM pitch/yaw	$2\,\mu$rad	$5\,\frac{\text{nrad}}{\sqrt{\text{Hz}}}\sqrt{1+\left(\frac{0.7\,\text{mHz}}{f}\right)^4}$
DWS angles: laser beam azimuth/elevation	$2\,\mu$rad	$0.15\,\frac{\text{nrad}}{\sqrt{\text{Hz}}}\sqrt{1+\left(\frac{0.7\,\text{mHz}}{f}\right)^4}$

Table 2.3: LISA OMS Sensing Performance

Due to the orbit dynamics the angle between the two OAs cannot remain fixed at 60°, but has to vary. This effect is called *breathing angle*. For this reason an Optical Assembly Actuator is present, that allows to control the OAs inter-angle. No information is available on this part, because the system is currently still under study. Nonetheless a few considerations can be made in order to estimate some of the parameters:

1. the pivot axis of rotation of both OAs should pass through the GRS' cage center in order to reduce disturbance on the TMs due to induced apparent forces;

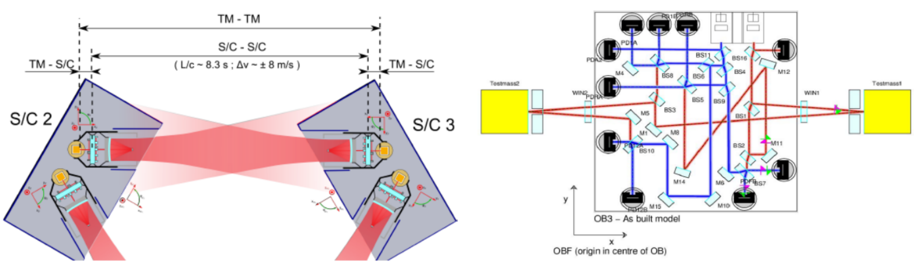

Figure 2.3: Optical Measurement System

2. the rotation range is expected to be $\pm 1°$ per year, this implies that the instantaneous rate shall not be greater than $6\,\frac{\text{nrad}}{\text{s}}$ in absolute value;

3. the rotation angle is assumed to be measurable within required precision.

Given these considerations a list of estimated parameters for the two OAs is reported in Table 2.4, where a white noise with constant spectral density and a resolution compatible with consideration 2 have been assumed.

Parameter	Value
Measurement range	$\pm 1°$
Angular resolution	1 nrad
Max. tracking speed	$5\,\mu$rad/s
Noise (assumed)	$1\,\text{nNm}/\sqrt{\text{Hz}}$

Table 2.4: Parameters of the OA Actuator

2.3 Gravitational Reference System

This subsystem is a complex devices that can be seen as composed of the following parts:

- *Test Mass* a cubical mass made of a particular gold–platinum alloy, that makes it reflective, engineered to weigh exactly 1.96 kg;

- *Electrostatic Suspension* a set of six electrodes, one for each surface of the cubical structure, that allow to control position and attitude of the Test Mass;

- *Caging mechanism* a mechanism that keeps the mass fixed in place during early stages of the mission;

- *Charge Management System* a system to manage the charge accumulated on the TM's surfaces;

- *Vacuum Chamber* that contains the whole system and manages the residual gas particles inside.

The Electrostatic Suspension is a device that contains the TM and can control all of the six DoFs at the same time. Each electrode is opposite to one of the outer surfaces of the TM and together they can be seen as two opposite armatures of a capacitor. By applying a voltage this will induce a charge into the TM and electrostatic forces can move and rotate the mass.

The mass is free to move so the distance that separates it from the surrounding electrodes will change over time. This will change the measured equivalent capacity of the virtual capacitors, therefore the GRS can also act as a sensor that is able to measure both position and attitude of the TM. The measurements are quite noisy when compared, for example, to the high precision DWS measurement obtained from the OMU. In particular, also the sensing capabilities of the GRS are subject to saturation; hence even if the gap between the TM and the cage is of 4 mm, only positions within 2 mm can be measured. ESA provided all the data regarding sensing capabilities, that are reported in Table 2.5.

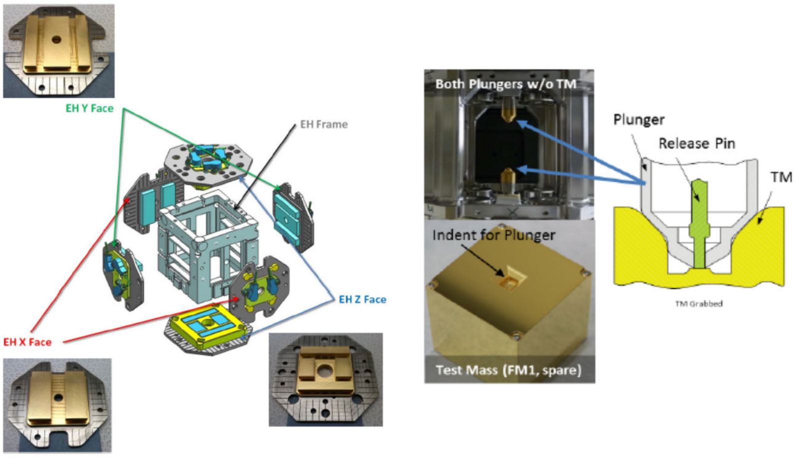

Figure 2.4: The Electrodes (left) and the Caging Mechanism (right)

The Caging Mechanism is a way of ensuring that the TM is stable and fixed in place during early phases of LISA, when high accelerations could make it impact the lateral surfaces of the cage, causing scratches and thus modifying the homogeneity of the mass and its measurement accuracy for the purpose of wave detection. Once LISA has reached orbital stability, the first phase is indeed *Test Mass Release*, during which the caging mechanism is released and the controller has to catch the TM by means of the Electrostatic Suspension before any impact with the cage can occur. The electrodes and caging mechanism are shown in Fig. 2.4.

It has been proven by LISA PF that the kinetic energy exchanged by trapped residual gas particles with the TM, during their Brownian motion, can be a major source of disturbance during the scientific activity. The Vacuum Chamber is thus equipped with a system that is capable of expelling regularly these trapped particles maintaining a good level of disturbance attenuation.

The Charge Management System has the task of managing the level of charge that is accumulated over time on the metallic TM by the GRS' electrodes and cosmic rays. It can autonomously discharge the mass by using UV lamps exploiting the photoelectric effect and keeping the voltages at the required levels.

The GRS has two different working modes: Wide Range (WR) mode and High Resolution (HR) mode. In WR the electrodes can apply a higher voltage, thus obtaining a higher actuation authority on the TM, at the price of increasing noise. This makes it not suitable to control the mass during science, where accuracy is of paramount importance, during which HR mode is recommended instead. The higher actuation authority makes WR mode useful during the Test Mass Release phase, where extremely bad initial conditions make the control problem challenging.

Noises of these actuators are provided in [11] and shown in Fig. 2.5. An important observation is that actuation noises on the linear forces on the y and z dimensions are up to 15 times worse with respect to the ones experienced on the x dimension. In addition, the torque noises along every dimension are up to 100 times lower w.r.t. the linear forces along the same directions. ESA provided the saturation values, that are reported in Table 2.6.

Mode	DoF	Range	Saturation	Noise
Wide Range	X	$100\,\mu$m	2 mm	$25\,\frac{\text{nm}}{\sqrt{\text{Hz}}}\sqrt{1+\left(\frac{1\,\text{mHz}}{f}\right)}$
	Y	$100\,\mu$m	2 mm	$25\,\frac{\text{nm}}{\sqrt{\text{Hz}}}\sqrt{1+\left(\frac{1\,\text{mHz}}{f}\right)}$
	Z	$150\,\mu$m	2 mm	$40\,\frac{\text{nm}}{\sqrt{\text{Hz}}}\sqrt{1+\left(\frac{1\,\text{mHz}}{f}\right)}$
	Φ	9 mrad	100 mrad	$3\,\frac{\mu\text{rad}}{\sqrt{\text{Hz}}}\sqrt{1+\left(\frac{1\,\text{mHz}}{f}\right)}$
	Θ	5 mrad	100 mrad	$1.8\,\frac{\mu\text{rad}}{\sqrt{\text{Hz}}}\sqrt{1+\left(\frac{1\,\text{mHz}}{f}\right)}$
	Ψ	9 mrad	100 mrad	$3\,\frac{\mu\text{rad}}{\sqrt{\text{Hz}}}\sqrt{1+\left(\frac{1\,\text{mHz}}{f}\right)}$
High Resolution	X	$25\,\mu$m	$100\,\mu$m	$1.8\,\frac{\text{nm}}{\sqrt{\text{Hz}}}\sqrt{1+\left(\frac{1\,\text{mHz}}{f}\right)}$
	Y	$25\,\mu$m	$100\,\mu$m	$1.8\,\frac{\text{nm}}{\sqrt{\text{Hz}}}\sqrt{1+\left(\frac{1\,\text{mHz}}{f}\right)}$
	Z	$25\,\mu$m	$150\,\mu$m	$3\,\frac{\text{nm}}{\sqrt{\text{Hz}}}\sqrt{1+\left(\frac{1\,\text{mHz}}{f}\right)}$
	Φ	2.5 mrad	9 mrad	$200\,\frac{\mu\text{rad}}{\sqrt{\text{Hz}}}\sqrt{1+\left(\frac{1\,\text{mHz}}{f}\right)}$
	Θ	2 mrad	5 mrad	$120\,\frac{\mu\text{rad}}{\sqrt{\text{Hz}}}\sqrt{1+\left(\frac{1\,\text{mHz}}{f}\right)}$
	Ψ	2.5 mrad	9 mrad	$200\,\frac{\mu\text{rad}}{\sqrt{\text{Hz}}}\sqrt{1+\left(\frac{1\,\text{mHz}}{f}\right)}$

Table 2.5: Sensing performance of the GRS

2.4 Star Tracker

The Star Tracker is a device that allows to measure the attitude of the SC with respect to the Heliocentric Inertial Reference System, also called inertial attitude. Two redundant star trackers are installed along the x-axis of the spacecraft's local reference system towards the constellation center. For what concerns the star trackers mounted in LISA PF, they were the Terma HE–5AS described in [18], which provided an attitude quaternion in the Hipparcos inertial reference frame. The attitude accuracy of $4.8\,\mu$rad around x–y axes and $48\,\mu$rad around z axis is not enough to acquire and keep the constellation links. Star trackers are used only during the first two phases and then turned off during science mode. Nonetheless they could be of use in this work because they are the only sensor to be able to measure the inertial attitude. For this reason in Table 2.7 are reported all the characteristics of the aforementioned Star Tracker taken directly from the data sheet [18].

2.5 Constellation Acquisition Sensor

The CAS is a CCD matrix of photodiodes, that is able to detect an incoming laser beam. It is placed inside the Optical Assembly and assists it in the acquisition and maintenance

Mode	DoF	Saturation Value
Wide Range	X	998 nN
	Y	1056 nN
	Z	595 nN
	Φ	11 nNm
	Θ	16 nNm
	Ψ	9 nNm
High Resolution	X	5.4 nN
	Y	5.7 nN
	Z	3.2 nN
	Φ	0.02 nNm
	Θ	0.03 nNm
	Ψ	0.015 nNm

Table 2.6: GRS saturation values

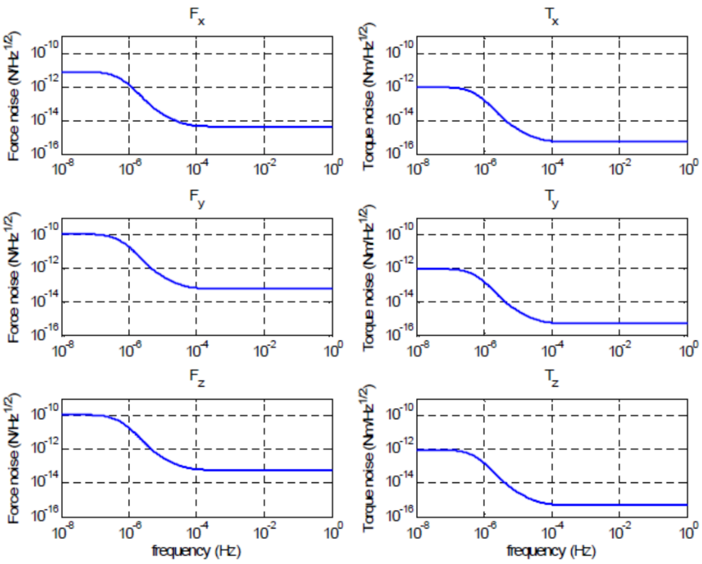

Figure 2.5: Noises of the GRS electrodes [11]

of the laser link. This sensor is mainly used during the *Constellation Acquisition* phase, but could also be employed to detect when a laser link has been lost, for example after a meteoroid impact.

For completeness the performance values of this sensor are reported in Table 2.8, taken from [13].

2.6 Disturbances

In the work [4] an extensive simulation is done of the disturbances affecting the TM at 1 mHz. The results show that the prevalent disturbances are the following, in descending order of magnitude:

1. *Electromagnetic noises* these are induced by on-board electronics, Lorentz accelerations due to interplanetary magnetic fields and cosmic radiation;

Parameter	Value
Field of View	$22° \times 22°$
Attitude accuracy	< 1 arcsec on the x–y axis < 5 arcsec on the z axis
Attitude re-acquisition	3s typical 10s worst case
Slew Rate	$< 3°$/s at full performance $> 0.3°/\text{s} \wedge < 2°$/s at reduced performance
Sampling Time	250 ms

Table 2.7: HE–5AS Star Tracker performance

Parameter	Value
Measurement Range	$\pm 250\,\mu$rad
Angular Resolution	$1\,\mu$rad
Angular Noise	–
Max. Tracking Speed	$2.5\,\mu$rad/s

Table 2.8: CAS Performance

2. *Pressure related noises* these are induced from momentum exchange with electromagnetic waves, out-gassing of the Test Masses, pressure from the laser reflecting off the surface, residual gas particles in the vacuum chamber and solar pressure.

3. *Thermo-elastic noises* these are due to the distortions in the spacecraft's mass distribution due to thermal effects and the time-varying self-gravity that exerts the SC on the TM itself.

For some of this disturbances estimated models are available, derived from theoretical studies or from real data collected during the LISA PF mission.

2.6.1 Test Mass Stiffness

The Test Mass can be seen as composed of an infinite number of infinitesimal volumes. Each of these volumes is attracted by the spacecraft's mass in different ways, according also to the position and attitude of the TM. The relative position of these tiny volumes with respect to the volumes of mass of the SC is also changing as a function of time, due to thermo-elastic deformations of the SC and propellant consumption. The macroscopic effect of all these disturbances is that the TM will have couplings between all of its Degrees of Freedom. According to [10] it can be modelled as a system of linear and torsional virtual springs connecting all of its DoFs:

$$\begin{bmatrix} a_x \\ a_y \\ a_z \\ \alpha_x \\ \alpha_y \\ \alpha_z \end{bmatrix} = \begin{bmatrix} \text{STT} & \text{SRT} \\ \text{STR} & \text{SRR} \end{bmatrix} \begin{bmatrix} \delta_x \\ \delta_y \\ \delta_z \\ \delta_\phi \\ \delta_\theta \\ \delta_\psi \end{bmatrix} = \begin{bmatrix} k_{xx} & k_{xy} & k_{xz} & k_{x\phi} & k_{x\theta} & k_{x\psi} \\ k_{yx} & k_{yy} & k_{yz} & k_{y\phi} & k_{y\theta} & k_{y\psi} \\ k_{zx} & k_{zy} & k_{zz} & k_{z\phi} & k_{z\theta} & k_{z\psi} \\ k_{\phi x} & k_{\phi y} & k_{\phi z} & k_{\phi\phi} & k_{\phi\theta} & k_{\phi\psi} \\ k_{\theta x} & k_{\theta y} & k_{\theta z} & k_{\theta\phi} & k_{\theta\theta} & k_{\theta\psi} \\ k_{\psi x} & k_{\psi y} & k_{\psi z} & k_{\psi\phi} & k_{\psi\theta} & k_{\psi\psi} \end{bmatrix} \begin{bmatrix} \delta_x \\ \delta_y \\ \delta_z \\ \delta_\phi \\ \delta_\theta \\ \delta_\psi \end{bmatrix}$$

Where a_x, a_y, a_z are the linear TM accelerations, α_x, α_y, α_z are the angular TM accelerations and δ_x, δ_y, δ_z, δ_ϕ, δ_θ, δ_ψ are the linear and angular displacements.

There are works that estimated the values of the stiffness matrix, such as [4] and [8], but during the mission lifetime there are certain parameters that are subject to variation, such as the Spacecraft mass due to propellant consumption, the consequent inertia variation, properties of center of mass and pivot locations. For most of these parametric uncertainties accurate estimations were not available as of the present study, among these also the TM stiffness. Therefore in [3] the stiffness matrix is assumed to vary within a symmetric interval around the null matrix, making its average value during mission the null matrix itself and simplifying subsequent computations. Nonetheless, in order to account for all possible disturbances and to effectively test the robustness of the designed drag free controller, during simulation some disturbances were considered with nominal values. TMs are acted upon by constant linear and angular disturbances, given by self-gravity:

$$\mathbf{d}_{\mathrm{sg1}} = \begin{bmatrix} 1 \\ 2 \\ 2 \end{bmatrix} \cdot 10^{-9}\,\mathrm{N}$$

$$\mathbf{d}_{\mathrm{sg2}} = \begin{bmatrix} 1 \\ -2 \\ 2 \end{bmatrix} \cdot 10^{-9}\,\mathrm{N}$$

$$\mathbf{D}_{\mathrm{sg1}} = \begin{bmatrix} 1 \\ 1 \\ 1 \end{bmatrix} \cdot 10^{-11}\,\mathrm{Nm}$$

$$\mathbf{D}_{\mathrm{sg2}} = \begin{bmatrix} 1 \\ 1 \\ 1 \end{bmatrix} \cdot 10^{-11}\,\mathrm{Nm}$$

In addition, every dimension of position and attitude is affected by a jitter component obtained by filtering a white noise. The linear acceleration filter and the angular acceleration filter have the following transfer functions:

$$\mathrm{H}_{\mathrm{TMd}}(s) = \frac{2 \cdot 10^{-15}\,(s + 9 \cdot 10^{-3})\,(s + 1.62 \cdot 10^{-3})\,(s + 2.88 \cdot 10^{-4})\,(s + 5.1 \cdot 10^{-5})}{(s + 7.74 \cdot 10^{-3})\,(s + 8.8 \cdot 10^{-4})\,(s + 1.3 \cdot 10^{-4})\,(s + 1.8 \cdot 10^{-5})}$$

$$\mathrm{H}_{\mathrm{TMD}}(s) = \frac{9.2 \cdot 10^{-17}\,(s + 9 \cdot 10^{-3})\,(s + 1.62 \cdot 10^{-3})\,(s + 2.88 \cdot 10^{-4})\,(s + 5.1 \cdot 10^{-5})}{(s + 7.74 \cdot 10^{-3})\,(s + 8.8 \cdot 10^{-4})\,(s + 1.3 \cdot 10^{-4})\,(s + 1.8 \cdot 10^{-5})}$$

The frequency response of both the noises is reported in Fig. 2.6. As concerns the stiffness

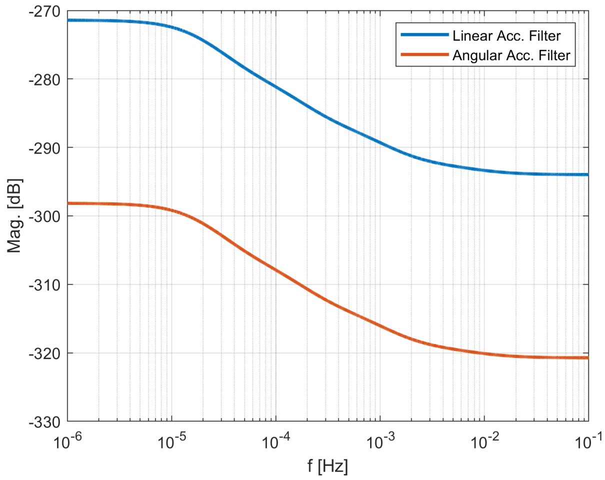

Figure 2.6: Frequency response of Self-Gravity noise filters

the latest available estimate [10] was used, obtained by means of a FEM model:

$$\begin{bmatrix} \mathbf{F}_{\mathrm{m}_j\mathrm{Stiff}} \\ \mathbf{M}_{\mathrm{m}_j\mathrm{Stiff}} \end{bmatrix} = \begin{bmatrix} \mathrm{STT} & \mathrm{SRT} \\ \mathrm{STR} & \mathrm{SRR} \end{bmatrix}$$

$$\mathrm{STT} = \begin{bmatrix} -5 \cdot 10^{-7} & -6 \cdot 10^{-8} & -6 \cdot 10^{-8} \\ -6 \cdot 10^{-8} & -2 \cdot 10^{-6} & -6 \cdot 10^{-8} \\ -6 \cdot 10^{-8} & -6 \cdot 10^{-8} & -2 \cdot 10^{-6} \end{bmatrix}$$

$$\mathrm{SRT} = \begin{bmatrix} -4.6 \cdot 10^{-10} & -4.6 \cdot 10^{-10} & -1 \cdot 10^{-9} \\ -4.6 \cdot 10^{-10} & -4.6 \cdot 10^{-10} & -4.6 \cdot 10^{-10} \\ -1 \cdot 10^{-9} & -4.6 \cdot 10^{-10} & -4.6 \cdot 10^{-10} \end{bmatrix}$$

$$\mathrm{STR} = \begin{bmatrix} -1.1 \cdot 10^{-6} & -1.1 \cdot 10^{-6} & -2.2 \cdot 10^{-6} \\ -1.1 \cdot 10^{-6} & -1.1 \cdot 10^{-6} & -1.1 \cdot 10^{-6} \\ -2.2 \cdot 10^{-6} & -1.1 \cdot 10^{-6} & -1.1 \cdot 10^{-6} \end{bmatrix}$$

$$\mathrm{SRR} = \begin{bmatrix} -2 \cdot 10^{-6} & -6 \cdot 10^{-8} & -6 \cdot 10^{-8} \\ -6 \cdot 10^{-8} & -1 \cdot 10^{-6} & -6 \cdot 10^{-8} \\ -6 \cdot 10^{-8} & -6 \cdot 10^{-8} & -1 \cdot 10^{-6} \end{bmatrix}$$

2.6.2 Solar Pressure

Data regarding the Solar Pressure disturbance was reported in [11]. It is modelled as composed of two contributions: a static DC component, that depends only on the SC's attitude and distance with respect to the Sun, and a jitter component whose spectral density is reported in Fig. 2.7.

In order to compute the vectorial disturbance to apply during simulation, the following computation, presented in [14], is implemented:

1. *Computation of the disturbance norm*: the norm is the sum of a constant term and a jitter component obtained by filtering white noise. The constant term is $\mathrm{k}_{\mathrm{dSC}} = 6.3513 \cdot 10^{-5}\,\mathrm{N}$ and the linear filter transfer function is

$$\mathrm{H}_{\odot\mathrm{press}} = \frac{7.875 \cdot 10^{-11}\,(s + 7.09 \cdot 10^{-2})\,(s^2 + 0.00578\,s + 2.954 \cdot 10^{-4})}{(s + 4.712 \cdot 10^{-3})\,(s^2 + 0.004\,s + 4 \cdot 10^{-4})}$$

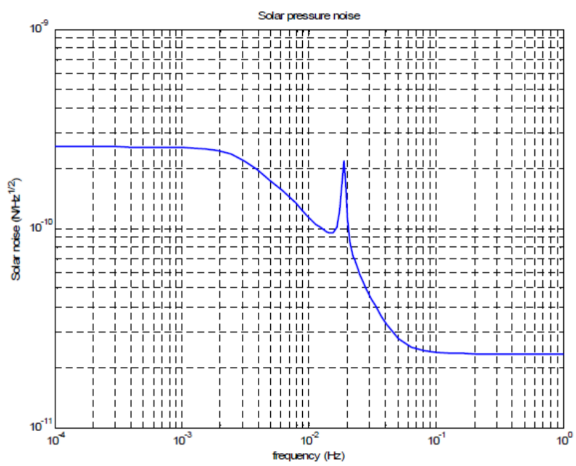

Figure 2.7: Solar Pressure Jitter

2. *Computation of the spacecraft IRF position*: the position of the SC expressed in the Inertial Reference Frame, with center in the Sun, and x axis in the direction of the Earth–Sun line at Vernal Equinox and z axis perpendicular to Earth's orbital plane, can be approximately expressed as

$$\mathbf{r}_{\mathrm{S}}^{\mathrm{I}} \approx \begin{bmatrix} 1 \\ 1 \\ 8.3 \cdot 10^{-3} \end{bmatrix} * \sin\left(\begin{bmatrix} 1.9924 \cdot 10^{-7} \\ 1.9924 \cdot 10^{-7} \\ 1.9924 \cdot 10^{-7} \end{bmatrix} t + \begin{bmatrix} \frac{\pi}{2} \\ 0 \\ \frac{3\pi}{2} \end{bmatrix} \right)$$

where $*$ is the element-wise product of two abstract vectors.

3. *Coordinate transformation from IRF to SRF*: this is implemented by measuring the attitude quaternion $\mathfrak{q}_{\mathrm{SI}}$ of the SC with respect to the IRF, obtained from the DFAC system, and converting it to the corresponding DCM matrix $\mathrm{T}(\mathfrak{q}_{\mathrm{SI}})$. Then applying the following expression:

$$\begin{aligned} \hat{\mathbf{r}}_{\mathrm{SI}}^{I} &= \frac{1}{\|\mathbf{r}_{\mathrm{SI}}^{I}\|_2} \mathbf{r}_{\mathrm{SI}}^{I} \\ \mathbf{d}_{\odot}^{\mathrm{S}} &= (\mathrm{k}_{\mathrm{dSC}} + \mathrm{H}_{\odot\mathrm{press}}\, \epsilon)\ \mathrm{T}(\mathfrak{q}_{\mathrm{SI}}) \cdot \hat{\mathbf{r}}_{\mathrm{S}}^{\mathrm{I}} \end{aligned}$$

where ϵ represents the white noise.

4. *Applying the Absorption coefficients*: the original method applied also some absorption coefficients $\boldsymbol{\gamma}$ in this way

$$\begin{aligned} \boldsymbol{\gamma} &= \begin{bmatrix} \gamma_1 \\ \gamma_2 \\ 1 \end{bmatrix} \\ \boldsymbol{d}_{\odot\mathrm{press}} &= \boldsymbol{\gamma} * \boldsymbol{d}_{\odot} \end{aligned}$$

however for this application the coefficients were all assumed equal to 1.

The vector $\boldsymbol{d}_{\odot\text{press}}$ is the force generated by the Sun on the SC. The torque $\mathbf{D}_{\odot\text{press}}$ is computed in the following way:

$$\mathbf{D}_{\odot\text{press}} = \begin{bmatrix} 0 & -0.6 & 0 \\ 0.6 & 0 & -0.1 \\ 0 & 0.1 & 0 \end{bmatrix} \boldsymbol{d}_{\odot\text{press}}$$

2.6.3 LISA Pathfinder Meteoroid Impacts

In this section the preliminary data derived from the LISA PF mission is presented. It comprises the measurements of linear and angular momentum transfers [5, 6]. This data and analysis was used in [3] to assess the performance and stability of the DFACS. Later in this work the new data will be presented with a more detailed study.

According to [6], the majority of impacts occurred on the lateral $+y$, $+z$, $-x$ and $-z$ surfaces of the spacecraft, as shown in Fig. 2.8. The frequency and intensity of the impacts was also depending on the spacecraft position on the Lissajous orbit around L1.

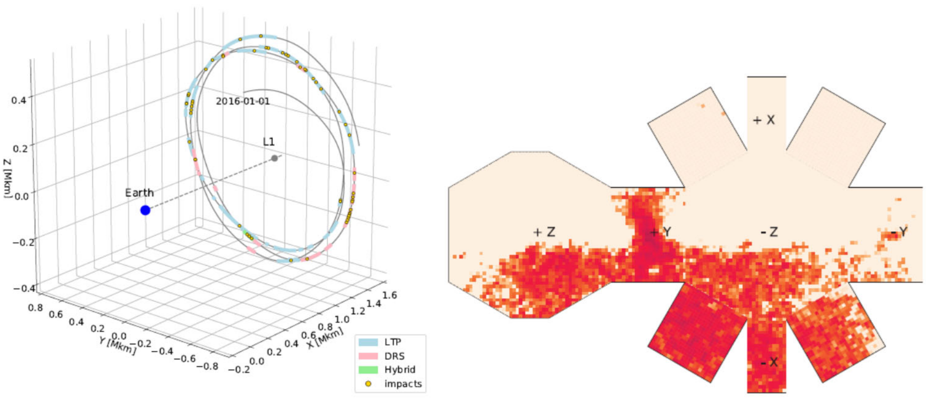

Figure 2.8: LISA PF Meteoroid Impacts [6]

The maximum transferred linear momentum was 230 μNs and a duration of 0.1 s has been used in [3]. This yields a maximum impulsive linear force of 2.3 mN. If the impact causes an angular displacement that is greater than the DWS measuring range the laser links are lost and the only solution is to enter again in acquisition phase, wasting several hours of useful science. The angular tolerance is 1 μrad, after that degree of rotation the other SC is not illuminated by the laser beam anymore, this situation is sketched in Fig. 2.9.

A set of MC simulations done in [3] highlighted that an error higher than 10^{-7} rad was experienced in the 28% of the cases. Only 2 simulations out of 30 exceeded the threshold of 10^{-6} rad: in this case the impact occurred on the panel perimeter and with a force modulus of 2.3 mN. Due to the higher modulus and the higher arm lengths, stronger disturbance torques were generated.

The laser beam can be seen as a cone of aperture 2 μrad and by considering an arm-length of $2.5 \cdot 10^6$ km, it approximately corresponds to a circle with a radius of 5 km at the receiving end. If the SC1 rotation induced by the micro-meteoroid impact is higher than 1 μrad, it means that SC2 will be no more illuminated by SC1. However, since SC1 is still illuminated by SC2 and SC3, its long-arm DWS sensor can still detect the incoming laser beams. The SC1 attitude control loop can still reconstruct the constellation frame and control the SC1 attitude recovering the pointing error.

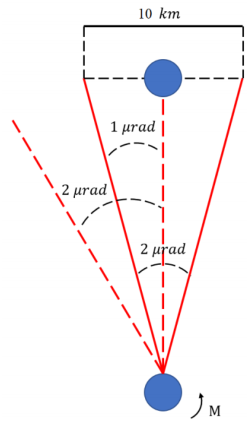

Figure 2.9: Condition for link loss

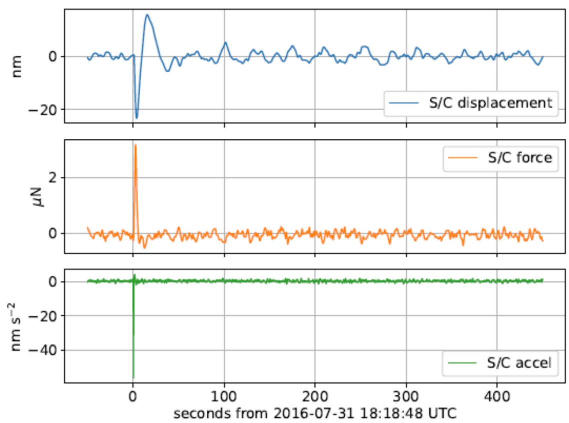

Figure 2.10: Effects of meteoroid impacts on TM acceleration

3 | Nonlinear Model

Although the complete final nonlinear model was already developed and validated in [9], in this chapter a possible derivation is still presented, in order to correctly identify the way in which each term enters into play, highlighting in particular the disturbances. All the figures that represent the model are taken from the cited work. Obviously, the final resulting equations will be the same, so the validation done in [9] is equally valid here.

The derivation starts by identifying the reference frames into play, the signals to be controlled (outputs) and the signals directly controlled (inputs); then proceeds with the simplifying assumptions.

During the three mission phases, already presented in Section 1.3, there are different sets of sensors available, thus, different quantities can be measured, with different accuracy. In this chapter the focus is put on the last of these stages, the Drag Free phase, so were necessary the operating conditions that characterize the sensors and actuators during that mission phase are assumed.

3.1 Reference Systems

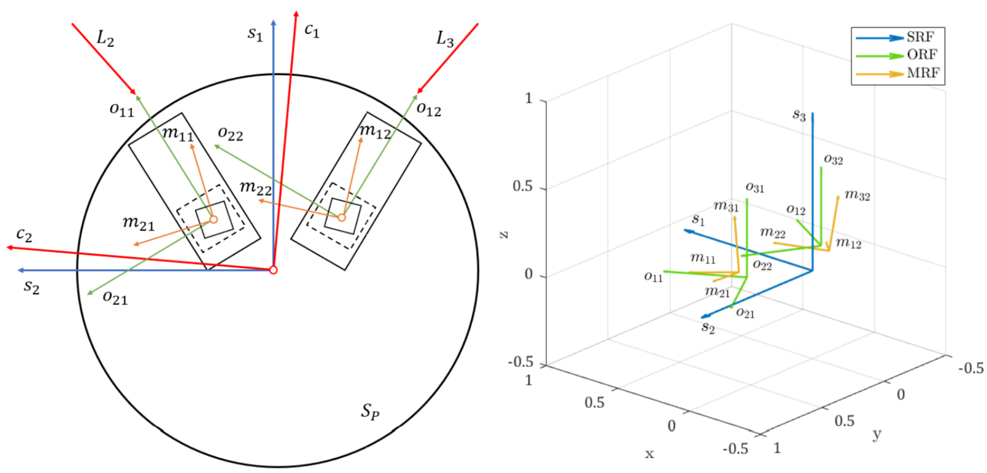

Figure 3.1: LISA Reference Systems

The general configuration of all the Reference Systems, or Reference Frames, is depicted in Fig. 3.1. The following frames are defined:

- *Inertial Reference Frame* IRF: is a quasi-inertial frame, that can be assumed inertial for this application, with its origin in the Sun. The $\mathbf{I}_3$ unitary vector is directed perpendicular to Earth's orbital plane around the Sun, $\mathbf{I}_1$ is directed along the line that connects the Sun to Earth at Vernal Equinox and $\mathbf{I}_2$ is obtained by the right-hand rule. It is defined by the set $\{\mathrm{O_I}, \mathbf{I}_1, \mathbf{I}_2, \mathbf{I}_3\}$ and represented with the letter S;

- *Constellation Reference Frame* CRF: this is a reference frame that is reconstructed on board and allows the spacecraft to evaluate its attitude with respect to the constellation formation. The origin is in the spacecraft's center, $\mathbf{c}_3$ is perpendicular to the plane defined by the two non-parallel incoming laser beams, $\mathbf{c}_1$ lies on the same plane and is defined as the bisectrix of the angle formed by the two incoming laser beams. CRF is defined by the set $\{\mathrm{O_C}, \mathbf{c}_1, \mathbf{c}_2, \mathbf{c}_3\}$ and represented with the letter C;

- *Spacecraft Reference Frame* SRF: this is the traditional frame of reference fixed with the spacecraft's body. Its origin is on the SC's center. The $\boldsymbol{s}_3$ unitary vector is orthogonal to the plane defined by the two Optical Assemblies, $\boldsymbol{s}_1$ lies on the same plane and is defined as the bisectrix of the nominal inter-telescope angle. It is defined by the set $\{\mathrm{O_S}, \boldsymbol{s}_1, \boldsymbol{s}_2, \boldsymbol{s}_3\}$ and represented with the letter S;

- Two *Optical Reference Frames* ORF: these have their origins on the OA's pivot point. The $\boldsymbol{o}_{1j}$ unitary vector is directed along the longitudinal symmetry line of the telescope, $\boldsymbol{o}_{3j}$ is parallel to $\boldsymbol{s}_3$. They are defined by $\mathrm{ORF}_j = \{\mathrm{O}_{\mathrm{o}j}, \boldsymbol{o}_{1j}, \boldsymbol{o}_{2j}, \boldsymbol{o}_{3j}\}$ and represented by the letter O_j;

- Two *Test Mass Reference Frames* TMRF: these are the frames fixed with the two TM's bodies and have their origins at the respective TMs' centers. The $\boldsymbol{m}_{1j}$ unitary vector is directed out of the TM's surface that faces the drag free direction at working conditions, $\boldsymbol{m}_{3j}$ points out of the top surface. They are defined by $\mathrm{TMRF}_j = \{\mathrm{O}_{\mathrm{m}j}, \boldsymbol{m}_{1j}, \boldsymbol{m}_{2j}, \boldsymbol{m}_{3j}\}$ and represented by the letter M_j.

It is useful to notice that the ORFs are not just rotated by a fixed amount around the z axis with respect to the SRF; but instead they also include the additional rotation of the OAs with respect to their nominal positions 60° apart.

This total of seven different Reference Frames are either directly measurable or computable on-board. Specifically, the CRF should be computed by implementing the following algorithm (here assumed to be carried out on Spacecraft 1, without loss of generality):

1. *Laser Beam Vector*: in this step the unitary vectors $\boldsymbol{\ell}_j^{\mathrm{S}}$ are computed starting from the measured azimuth α_j and elevation θ_j angles (measured by DWS). These unitary vectors represent the direction of the incoming laser beams in the local SRF. The subscript j refers to the three different spacecrafts, that are numbered 1 to 3. Thus, for example, SC1 will receive lasers $\boldsymbol{\ell}_2$ and $\boldsymbol{\ell}_3$. Recalling that the azimuth angle is the rotation from $\boldsymbol{o}_2$ in the direction of $\boldsymbol{o}_1$ along the $\boldsymbol{o}_1$–$\boldsymbol{o}_2$ plane and elevation is the angle from the $\boldsymbol{o}_1$–$\boldsymbol{o}_2$ plane, positive towards the $\boldsymbol{o}_3$ direction; to derive the

expression it is sufficient to apply the sequence of rotations to $\boldsymbol{o}_2$:

$$\mathrm{R} = \mathrm{R}_\mathrm{z}(-\alpha_j)\,\mathrm{R}_\mathrm{x}(\theta_j) = \begin{bmatrix} \cos(\alpha_j) & \sin(\alpha_j) & 0 \\ -\sin(\alpha_j) & \cos(\alpha_j) & 0 \\ 0 & 0 & 1 \end{bmatrix} \begin{bmatrix} 1 & 0 & 0 \\ 0 & \cos(\theta_j) & -\sin(\theta_j) \\ 0 & \sin(\theta_j) & \cos(\theta_j) \end{bmatrix}$$

$$\boldsymbol{\ell}_j^{\mathrm{O}_j} = \mathrm{R}\,\boldsymbol{o}_2 = \begin{bmatrix} \sin(\alpha_j)\cos(\theta_j) \\ \cos(\alpha_j)\cos(\theta_j) \\ \sin(\theta_j) \end{bmatrix}$$

$$\boldsymbol{\ell}_j^{\mathrm{S}} = \mathrm{T}_{\mathrm{O}_j}^{\mathrm{S}}\boldsymbol{\ell}_j^{\mathrm{O}_j} \tag{3.1}$$

where $\mathrm{T}_{\mathrm{O}_j}^{\mathrm{S}}$ is the attitude DCM of the Spacecraft with respect to the j-th Optical Assembly, more details are given later;

2. *Constellation Plane Normal*: computes the orthogonal vector to the plane P containing both laser vectors. The orthogonal unitary vector is obtained by using the cross-product:

$$\boldsymbol{c}_3 = \frac{\boldsymbol{\ell}_3^{\mathrm{S}} \times \boldsymbol{\ell}_2^{\mathrm{S}}}{\|\boldsymbol{\ell}_3^{\mathrm{S}} \times \boldsymbol{\ell}_2^{\mathrm{S}}\|_2} \tag{3.2}$$

then a unique plane P is defined by

$$\mathrm{P} = \{\boldsymbol{x} \in \mathbb{R}^3 \mid \boldsymbol{c}_3^\top \cdot \boldsymbol{x} = 0\} \tag{3.3}$$

notice that the order of the two vectors in the cross-product is such to allow $\boldsymbol{c}_3$ to have a positive component along $\boldsymbol{s}_3$;

3. *Bisectrix Computation*: the vector on plane P that bisects the angle between $\boldsymbol{\ell}_2^{\mathrm{S}}$ and $\boldsymbol{\ell}_3^{\mathrm{S}}$ can be found by noticing that both the laser vectors are unitary vectors, thus, they constitute the edges of an isosceles triangle, that has its main vertex in the origin. Therefore, $\boldsymbol{c}_1$ can be computed by finding the mid-point of the basis of the triangle and then normalizing it:

$$\begin{aligned} \Delta\boldsymbol{\ell} &= \boldsymbol{\ell}_2^{\mathrm{S}} - \boldsymbol{\ell}_3^{\mathrm{S}} && \text{basis segment} \\ \boldsymbol{\ell}_\mathrm{M} &= \boldsymbol{\ell}_3^{\mathrm{S}} + \frac{1}{2}\Delta\boldsymbol{\ell} = \frac{1}{2}\boldsymbol{\ell}_2^{\mathrm{S}} + \frac{1}{2}\boldsymbol{\ell}_3^{\mathrm{S}} && \text{mid-point} \\ \boldsymbol{c}_1 &= \frac{\boldsymbol{\ell}_\mathrm{M}}{\|\boldsymbol{\ell}_\mathrm{M}\|} = \frac{\boldsymbol{\ell}_2^{\mathrm{S}} + \boldsymbol{\ell}_3^{\mathrm{S}}}{\|\boldsymbol{\ell}_2^{\mathrm{S}} + \boldsymbol{\ell}_3^{\mathrm{S}}\|_2} \end{aligned} \tag{3.4}$$

4. *Remaining Axis*: the remaining unitary vector $\boldsymbol{c}_2$ is obtained by imposing the frame to be right-handed. In a right-handed frame it holds that $\boldsymbol{c}_2 = \boldsymbol{c}_3 \times \boldsymbol{c}_1$, where $\boldsymbol{c}_1$ an $\boldsymbol{c}_3$ were computed in the previous steps.

This algorithm was slightly modified with respect to the one presented in [3]. Specifically, the implementation of Step 3 reported here is simpler.

The new version has been tested on MATLAB with 100 million randomly generated laser vectors. The test ensured the following properties in the resulting bisectrix $\boldsymbol{c}_1$:

- $\boldsymbol{c}_3^\top \cdot \boldsymbol{c}_1 = 0$, that is, the bisectrix should belong to the plane P defined by the incoming laser beams;
- $\|\boldsymbol{c}_1\|_2 = 1$, because the vector has to be of unitary norm;
- $\arccos(\boldsymbol{\ell}_2^{\mathrm{S}\top} \cdot \boldsymbol{c}_1) = \arccos(\boldsymbol{\ell}_3^{\mathrm{S}\top} \cdot \boldsymbol{c}_1)$, that is, the angles between the bisectrix and both $\boldsymbol{\ell}_2^{\mathrm{S}}$ and $\boldsymbol{\ell}_3^{\mathrm{S}}$ should be equal, by definition of bisectrix.

3.2 Relevant Variables

During the Drag Free phase the controller should be able to perform the following tasks:

- *Maintain the Laser Links*: control the attitude of the spacecraft and the telescopes inter-angle in a way that keeps the lasers connected;
- *Control the Test Mass position*: the controller has to keep the TMs at the center of the cage. It can achieve it by moving the spacecraft around the Test Masses using the MPS or by directly affecting the single Test Mass. Note that a specific more stringent performance is required for position control along the Drag Free direction;
- *Control the Test Mass attitude*: the controller has to regulate the TM cube attitude so that the laser can reflect off its surface properly.

The aforementioned requirements make the following quantities relevant for control:

- $\mathfrak{q}_{\mathrm{SC}}$ the attitude of the spacecraft with respect to the constellation frame;
- $\boldsymbol{r}^{\mathrm{o}_1}_{\mathrm{m}_1\mathrm{o}_1}$ and $\boldsymbol{r}^{\mathrm{o}_2}_{\mathrm{m}_2\mathrm{o}_2}$ the position of the Test Masses with respect to the respective cage centers, in ORF coordinates;
- $\mathfrak{q}_{\mathrm{m}_1\mathrm{o}_1}$ and $\mathfrak{q}_{\mathrm{m}_2\mathrm{o}_2}$ the Test Masses' attitudes with respect to their ORFs;
- ξ_1 and ξ_2 the rotation angle of the two Optical Assemblies with respect to their nominal positions.

These quantities can be obtained in different ways:

- $\mathfrak{q}_{\mathrm{SC}}$ can be locally reconstructed starting by the SC–SC DWS measured angles, that allow for the reconstruction of the CRF frame, from which the quaternion rotation $\mathfrak{q}_{\mathrm{SC}}$ can be computed;
- $\boldsymbol{r}^{\mathrm{o}_1}_{\mathrm{m}_1\mathrm{o}_1}$ and $\boldsymbol{r}^{\mathrm{o}_2}_{\mathrm{m}_2\mathrm{o}_2}$ can be completely measured by the GRS or partially (only x–axis) by the local SC–TM interferometer;
- $\mathfrak{q}_{\mathrm{m}_1\mathrm{o}_1}$ and $\mathfrak{q}_{\mathrm{m}_2\mathrm{o}_2}$ can be completely measured by the GRS or partially (pitch and yaw) by the SC–TM DWS;
- ξ_1 and ξ_2 are assumed to be directly measured.

3.3 Spacecraft Attitude

In order to maintain both laser links during orbit, the SC attitude should follow the constellation attitude as close as possible. This is achieved by regulating $\mathfrak{q}_{\mathrm{SC}}$ to zero.

First of all the attitude quaternion can be obtained from the angular velocity by integrating the following kinematic relationship:

$$\dot{\mathfrak{q}}_{\mathrm{SC}} = \frac{1}{2}\,\mathfrak{q}_{\mathrm{SC}} \otimes \begin{bmatrix} 0 \\ \boldsymbol{\omega}^{\mathrm{S}}_{\mathrm{SC}} \end{bmatrix}$$

The angular velocity of the spacecraft with respect to the constellation is simply

$$\boldsymbol{\omega}_{\mathrm{SC}}^{\mathrm{S}} = \boldsymbol{\omega}_{\mathrm{SI}}^{\mathrm{S}} - \mathrm{T}_{\mathrm{C}}^{\mathrm{S}}\,\boldsymbol{\omega}_{\mathrm{CI}}^{\mathrm{C}}$$

where the SI or CI subscripts indicate the inertial attitudes and $\mathrm{T}_{\mathrm{C}}^{\mathrm{S}}$ is the coordinate transformation from the CRF to the SRF.

The angular velocity is affected only by applied torques, thus it is obtained by integrating the expression of its time derivative:

$$\dot{\boldsymbol{\omega}}_{\mathrm{SC}}^{\mathrm{S}} = \dot{\boldsymbol{\omega}}_{\mathrm{SI}}^{\mathrm{S}} - \mathrm{T}_{\mathrm{C}}^{\mathrm{S}}\,\dot{\boldsymbol{\omega}}_{\mathrm{CI}}^{\mathrm{C}} - \dot{\mathrm{T}}_{\mathrm{C}}^{\mathrm{S}}\,\boldsymbol{\omega}_{\mathrm{CI}}^{\mathrm{C}} = \dot{\boldsymbol{\omega}}_{\mathrm{SI}}^{\mathrm{S}} - \mathrm{T}_{\mathrm{C}}^{\mathrm{S}}\,\dot{\boldsymbol{\omega}}_{\mathrm{CI}}^{\mathrm{C}} + \boldsymbol{\omega}_{\mathrm{SC}}^{\mathrm{S}} \times \mathrm{T}_{\mathrm{C}}^{\mathrm{S}}\,\boldsymbol{\omega}_{\mathrm{CI}}^{\mathrm{C}}$$

In this expression $\boldsymbol{\omega}_{\mathrm{CI}}^{\mathrm{C}}$ and $\dot{\boldsymbol{\omega}}_{\mathrm{CI}}^{\mathrm{C}}$ depend on the directions of the incoming lasers and, in general, from the rotation of the whole satellite formation. In [3] approximate expressions were obtained by simulating LISA orbits:

$$\boldsymbol{\omega}_{\mathrm{CI}}^{\mathrm{C}} \approx \begin{bmatrix} 1.7266 \cdot 10^{-7} \\ 1.7266 \cdot 10^{-7} \\ -9.9687 \cdot 10^{-8} \end{bmatrix} * \sin\left(\begin{bmatrix} 1.9924 \cdot 10^{-7} \\ 1.9924 \cdot 10^{-7} \\ 0 \end{bmatrix} t + \begin{bmatrix} \frac{\pi}{2} \\ 0 \\ \frac{\pi}{2} \end{bmatrix}\right) \tag{3.5}$$

$$\dot{\boldsymbol{\omega}}_{\mathrm{CI}}^{\mathrm{C}} \approx \begin{bmatrix} 3.4425 \cdot 10^{-14} \\ 3.4425 \cdot 10^{-14} \\ 0 \end{bmatrix} * \sin\left(\begin{bmatrix} 1.9924 \cdot 10^{-7} \\ 1.9924 \cdot 10^{-7} \\ 0 \end{bmatrix} t + \begin{bmatrix} \pi \\ \frac{\pi}{2} \\ 0 \end{bmatrix}\right) \tag{3.6}$$

The Inertial angular acceleration of the Spacecraft can be derived from the Angular Momentum $\mathbf{H}_{\mathrm{SI}}^{\mathrm{I}}$:

$$\begin{aligned}
\dot{\mathbf{H}}_{\mathrm{SI}}^{\mathrm{S}} &= \mathrm{J}_{\mathrm{S}}\,\dot{\boldsymbol{\omega}}_{\mathrm{SC}}^{\mathrm{S}} \\
\mathbf{H}_{\mathrm{SI}}^{\mathrm{S}} &= \mathrm{T}_{\mathrm{I}}^{\mathrm{S}}\,\mathbf{H}_{\mathrm{SI}}^{\mathrm{I}} \\
\dot{\mathbf{H}}_{\mathrm{SI}}^{\mathrm{S}} &= \mathrm{T}_{\mathrm{I}}^{\mathrm{S}}\,\dot{\mathbf{H}}_{\mathrm{SI}}^{\mathrm{I}} + \dot{\mathrm{T}}_{\mathrm{I}}^{\mathrm{S}}\,\mathbf{H}_{\mathrm{SI}}^{\mathrm{I}} = \mathrm{T}_{\mathrm{I}}^{\mathrm{S}}\,\dot{\mathbf{H}}_{\mathrm{SI}}^{\mathrm{I}} - \boldsymbol{\omega}_{\mathrm{SI}}^{\mathrm{S}} \times \mathrm{T}_{\mathrm{I}}^{\mathrm{S}}\,\mathbf{H}_{\mathrm{SI}}^{\mathrm{I}} \\
\mathrm{J}_{\mathrm{S}}\,\dot{\boldsymbol{\omega}}_{\mathrm{SI}}^{\mathrm{S}} &= \dot{\mathbf{H}}_{\mathrm{SI}}^{\mathrm{S}} - \boldsymbol{\omega}_{\mathrm{SI}}^{\mathrm{S}} \times \left(\mathrm{J}_{\mathrm{S}}\,\boldsymbol{\omega}_{\mathrm{SI}}^{\mathrm{S}}\right)
\end{aligned}$$

where J_{S} is the SC Inertia Matrix with respect to the SRF.
The conservation of Angular Momentum provides the relation for $\dot{\mathbf{H}}_{\mathrm{SI}}^{\mathrm{S}}$:

$$\begin{aligned}
\dot{\mathbf{H}}_{\mathrm{SI}}^{\mathrm{S}} &= \text{External Torques} - \text{Internal Torques} \\
\text{External Torques} &= \mathbf{M}_{\mathrm{T}}^{\mathrm{S}} + \mathbf{D}_{\mathrm{T}}^{\mathrm{S}} + \mathbf{D}_{\odot\mathrm{press}}^{\mathrm{S}} + \mathbf{M}_{\mathrm{met}}^{\mathrm{S}} \\
\text{Internal Torques} &= \sum_{j=1,2} \mathrm{T}_{\mathrm{o}_j}^{\mathrm{S}}\,\mathrm{I}_{zz}\,\ddot{\boldsymbol{\xi}}_j^{\mathrm{o}_j} + \mathrm{T}_{\mathrm{o}_j}^{\mathrm{S}}\,\mathbf{M}_{\mathrm{E}_j}^{\mathrm{o}_j} + \boldsymbol{b}_j^{\mathrm{S}} \times \left(\mathrm{T}_{\mathrm{o}_j}^{\mathrm{S}}\,\mathbf{F}_{\mathrm{E}_j}^{\mathrm{o}_j}\right)
\end{aligned}$$

Overall the attitude equations are

$$\dot{\mathfrak{q}}_{\mathrm{SC}} = \frac{1}{2}\,\mathfrak{q}_{\mathrm{SC}} \otimes \begin{bmatrix} 0 \\ \boldsymbol{\omega}_{\mathrm{SC}}^{\mathrm{S}} \end{bmatrix} \tag{3.7}$$

$$\dot{\boldsymbol{\omega}}_{\mathrm{SC}}^{\mathrm{S}} = \dot{\boldsymbol{\omega}}_{\mathrm{SI}}^{\mathrm{S}} - \dot{\boldsymbol{\omega}}_{\mathrm{CI}}^{\mathrm{S}} + \boldsymbol{\omega}_{\mathrm{SC}}^{\mathrm{S}} \times \mathrm{T}_{\mathrm{C}}^{\mathrm{S}}\,\boldsymbol{\omega}_{\mathrm{CI}}^{\mathrm{C}} \tag{3.8}$$

$$\begin{aligned}
\dot{\boldsymbol{\omega}}_{\mathrm{SI}}^{\mathrm{S}} = &-\mathrm{J}_{\mathrm{S}}^{-1}\,\boldsymbol{\omega}_{\mathrm{SI}}^{\mathrm{S}} \times \left(\mathrm{J}_{\mathrm{S}}\,\boldsymbol{\omega}_{\mathrm{SI}}^{\mathrm{S}}\right) + \mathrm{J}_{\mathrm{S}}^{-1}\left(\mathbf{M}_{\mathrm{T}}^{\mathrm{S}} + \mathbf{D}_{\mathrm{T}}^{\mathrm{S}} + \mathbf{D}_{\odot\mathrm{press}}^{\mathrm{S}} + \mathbf{M}_{\mathrm{met}}^{\mathrm{S}}\right) + \\
&- \mathrm{J}_{\mathrm{S}}^{-1} \sum_{j=1,2} \mathrm{T}_{\mathrm{o}_j}^{\mathrm{S}}\,\mathrm{I}_{zz}\,\ddot{\boldsymbol{\xi}}_j^{\mathrm{o}_j} + \mathrm{T}_{\mathrm{o}_j}^{\mathrm{S}}\,\mathbf{M}_{\mathrm{E}_j}^{\mathrm{o}_j} + \boldsymbol{b}_j^{\mathrm{S}} \times \left(\mathrm{T}_{\mathrm{o}_j}^{\mathrm{S}}\,\mathbf{F}_{\mathrm{E}_j}^{\mathrm{o}_j}\right)
\end{aligned} \tag{3.9}$$

$$\mathrm{T}_{\mathrm{C}}^{\mathrm{S}} = \mathrm{R}(\mathfrak{q}_{\mathrm{SC}}^{*}) \tag{3.10}$$

$$\mathrm{T}_{\mathrm{o}_1}^{\mathrm{S}} = \mathrm{R}_z\left(\frac{\pi}{6} + \xi_1\right) \tag{3.11}$$

$$\mathrm{T}_{\mathrm{o}_2}^{\mathrm{S}} = \mathrm{R}_z\left(-\frac{\pi}{6} + \xi_2\right) \tag{3.12}$$

Where

- $\mathrm{J_S}$ is the SC Inertia Matrix with respect to the SRF;
- $\mathbf{M}_{\mathrm{T}}^{\mathrm{S}}$ is the Torque provided by the thrusters, that is given in SRF coordinates;
- $\mathbf{D}_{\mathrm{T}}^{\mathrm{S}}$ is the torque noise of the thrusters;
- $\mathbf{D}_{\odot\mathrm{press}}^{\mathrm{S}}$ is the Torque from Solar pressure described in Section 2.6.2;
- $\mathbf{M}_{\mathrm{met}}^{\mathrm{S}}$ is the Torque exerted by the Meteoroid impact onto the SC;
- I_{zz} is the Inertia of both Optical Assemblies along the z–axis, that passes through the pivot point;
- $\boldsymbol{\xi}_j^{\mathrm{o}_j}$ is the rotation vector that represents the rotation of the j-th OA, expressed in the ORF:

$$\boldsymbol{\xi}_j^{\mathrm{o}_j} = \begin{bmatrix} 0 \\ 0 \\ \xi_j \end{bmatrix}, \quad \boldsymbol{\xi}_j \in \mathbb{R}^3, \quad \xi_j \in \mathbb{R}$$

- $\mathbf{M}_{\mathrm{E}_j}^{\mathrm{o}_j}$ is the Torque generated by the j-th GRS electrodes on the j-th Test Mass, in ORF coordinates;
- $\mathbf{F}_{\mathrm{E}_j}^{\mathrm{o}_j}$ is the Force applied by the j-th GRS electrodes on the j-th Test Mass, in ORF coordinates;
- $\boldsymbol{b}_j^{\mathrm{S}}$ is the position with respect to the SC CoM (the SRF origin) of the cage center of the j-th GRS.

3.4 Optical Assembly Rotation

Another task that the controller needs to fulfill in order to keep the laser link active is the breathing of the OAs inter-angle. Previous works on LISA orbits showed that the internal angles of the triangular formation varies of $\pm 1°$ per year, due to the particular orbit dynamics.

The rotation is relative to the OA's nominal position. The acceleration on the OA is due to the Spacecraft's motion and to the OA's motion itself:

$$\ddot{\boldsymbol{\xi}}_{\mathrm{o}_j S}^{\mathrm{S}} = \ddot{\boldsymbol{\xi}}_{\mathrm{o}_j}^{\mathrm{S}} = \ddot{\boldsymbol{\xi}}_{\mathrm{o}_j I}^{\mathrm{S}} - \dot{\boldsymbol{\omega}}_{\mathrm{SI}}^{\mathrm{S}}$$

The angular acceleration of the Optical Assembly depends on its angular momentum $\mathbf{H}_{\mathrm{o}_j I}^{\mathrm{o}_j}$:

$$\begin{aligned}
\dot{\mathbf{H}}_{\mathrm{o}_j I}^{\mathrm{o}_j} &= \mathrm{I}_{zz}\, \ddot{\boldsymbol{\xi}}_{\mathrm{o}_j I}^{\mathrm{o}_j}, \quad \mathrm{I}_{zz} \in \mathbb{R} \\
\mathbf{H}_{\mathrm{o}_j I}^{\mathrm{o}_j} &= \mathrm{T}_{\mathrm{I}}^{\mathrm{o}_j}\, \mathbf{H}_{\mathrm{o}_j I}^{\mathrm{I}} \\
\dot{\mathbf{H}}_{\mathrm{o}_j I}^{\mathrm{o}_j} &= \dot{\mathbf{H}}_{\mathrm{o}_j I}^{\mathrm{o}_j} - \dot{\boldsymbol{\xi}}_{\mathrm{o}_j I}^{\mathrm{o}_j} \times \mathbf{H}_{\mathrm{o}_j I}^{\mathrm{o}_j} = \dot{\mathbf{H}}_{\mathrm{o}_j I}^{\mathrm{o}_j} - \mathrm{I}_{zz}\, \dot{\boldsymbol{\xi}}_{\mathrm{o}_j I}^{\mathrm{o}_j} \times \dot{\boldsymbol{\xi}}_{\mathrm{o}_j I}^{\mathrm{o}_j} = \mathrm{T}_{\mathrm{I}}^{\mathrm{o}_j}\, \dot{\mathbf{H}}_{\mathrm{o}_j I}^{\mathrm{I}} \\
\mathrm{I}_{zz}\, \ddot{\boldsymbol{\xi}}_{\mathrm{o}_j I}^{\mathrm{o}_j} &= \dot{\mathbf{H}}_{\mathrm{o}_j I}^{\mathrm{o}_j}
\end{aligned}$$

This last equation shows that for the OA, the variation in angular momentum in the ORF coordinates is simply given by the total torques acting on the part:

$$\mathrm{I}_{zz}\,\ddot{\boldsymbol{\xi}}^{\mathrm{o}_j}_{\mathrm{o}_j I} = \mathbf{M}^{\mathrm{o}_j}_{\mathrm{OA}_j} + \mathbf{D}^{\mathrm{o}_j}_{\xi_j} - \mathbf{M}^{\mathrm{o}_j}_{\mathrm{E}_j}$$

Where

- I_{zz} is the inertia of the OA, it is assumed that both have same inertia;
- $\mathbf{M}^{\mathrm{o}_j}_{\mathrm{OA}_j}$ is the input torque from the OA actuator;
- $\mathbf{D}^{\mathrm{o}_j}_{\xi_j}$ is the actuation noise;
- $\mathbf{M}^{\mathrm{o}_j}_{\mathrm{E}_j}$ is the torque applied by the j-th GRS electrodes to the j-th Test Mass. It appears with the negative sign because it is a reaction torque.

The response of the OA is assumed to be of the second order, like a torsional spring with damper. Therefore, other forces have to be included:

$$\mathrm{I}_{zz}\,\ddot{\boldsymbol{\xi}}^{\mathrm{o}_j}_{\mathrm{o}_j} = -\mathrm{I}_{zz}\,\mathrm{T}^{\mathrm{o}_j}_{\mathrm{S}}\,\dot{\boldsymbol{\omega}}^{\mathrm{S}}_{\mathrm{SI}} + \mathbf{M}^{\mathrm{o}_j}_{\mathrm{OA}_j} + \mathbf{D}^{\mathrm{o}_j}_{\xi_j} - \mathbf{M}^{\mathrm{o}_j}_{\mathrm{E}_j} - \mathrm{k}_\xi\,\boldsymbol{\xi}^{\mathrm{o}_j}_{\mathrm{o}_j} - \beta\,\dot{\boldsymbol{\xi}}^{\mathrm{o}_j}_{\mathrm{o}_j}$$

$$\ddot{\boldsymbol{\xi}}^{\mathrm{o}_j}_{\mathrm{o}_j} + \frac{\beta}{\mathrm{I}_{zz}}\,\dot{\boldsymbol{\xi}}^{\mathrm{o}_j}_{\mathrm{o}_j} + \frac{\mathrm{k}_\xi}{\mathrm{I}_{zz}}\,\boldsymbol{\xi}^{\mathrm{o}_j}_{\mathrm{o}_j} = -\mathrm{T}^{\mathrm{o}_j}_{\mathrm{S}}\,\dot{\boldsymbol{\omega}}^{\mathrm{S}}_{\mathrm{SI}} + \frac{1}{\mathrm{I}_{zz}}\left(\mathbf{M}^{\mathrm{o}_j}_{\mathrm{OA}_j} + \mathbf{D}^{\mathrm{o}_j}_{\xi_j} - \mathbf{M}^{\mathrm{o}_j}_{\mathrm{E}_j}\right)$$

Where k_ξ is the proportional constant and β is the damping. Recalling the general form of a second order system, the characteristic parameters are

$$\omega_n = \sqrt{\frac{\mathrm{k}_\xi}{\mathrm{I}_{zz}}} \quad \text{Natural Frequency}$$

$$\zeta = \frac{\beta}{2\sqrt{\mathrm{I}_{zz}\,\mathrm{k}_\xi}} \quad \text{Damping Coefficient}$$

Overall the equations of the OAs rotation are

$$\ddot{\boldsymbol{\xi}}^{\mathrm{o}_j}_{\mathrm{o}_j} = \frac{1}{\mathrm{I}_{zz}}\left(\mathbf{M}^{\mathrm{o}_j}_{\mathrm{OA}_j} + \mathbf{D}^{\mathrm{o}_j}_{\xi_j} - \mathbf{M}^{\mathrm{o}_j}_{\mathrm{E}_j}\right) - \mathrm{T}^{\mathrm{o}_j}_{\mathrm{S}}\,\dot{\boldsymbol{\omega}}^{S}_{\mathrm{SI}} - \frac{\beta}{\mathrm{I}_{zz}}\,\dot{\boldsymbol{\xi}}^{\mathrm{o}_j}_{\mathrm{o}_j} - \frac{\mathrm{k}_\xi}{\mathrm{I}_{zz}}\,\boldsymbol{\xi}^{\mathrm{o}_j}_{\mathrm{o}_j} \tag{3.13}$$

$$\mathrm{T}^{\mathrm{o}_1}_{\mathrm{S}} = \mathrm{T}^{\mathrm{S}^\top}_{\mathrm{o}_1} = \mathrm{R}_z(-\frac{\pi}{6} - \xi_1) \tag{3.14}$$

$$\mathrm{T}^{\mathrm{o}_2}_{\mathrm{S}} = \mathrm{T}^{\mathrm{S}^\top}_{\mathrm{o}_2} = \mathrm{R}_z(\frac{\pi}{6} - \xi_2) \tag{3.15}$$

The term $\dot{\boldsymbol{\omega}}^{S}_{\mathrm{SI}}$ is given in Eq. 3.9.

3.5 Test Mass Attitude

The Test Mass attitude is controlled by means of the GRS electrodes. It is important to keep the Test Mass aligned with the cage frame in order to let the lasers properly reflect off its front surface.

As for the SC attitude case, it is achieved by regulating the relative attitude $\mathfrak{q}_{\mathrm{m}_j}$ to zero. This quantity represents the relative attitude of the mass with respect to the cage frame. It is obtained by integration of the following kinematic expression:

$$\dot{\mathfrak{q}}_{\mathrm{m}_j} = \frac{1}{2}\,\mathfrak{q}_{\mathrm{m}_j} \otimes \begin{bmatrix} 0 \\ \boldsymbol{\omega}^{\mathrm{m}_j}_{\mathrm{m}_j\mathrm{o}_j} \end{bmatrix}, \quad \mathfrak{q}_{\mathrm{m}_j} = \mathfrak{q}_{\mathrm{m}_j\mathrm{o}_j}$$

The angular velocity $\boldsymbol{\omega}^{\mathrm{m}_j}_{\mathrm{m}_j\mathrm{o}_j}$ is given by the difference:

$$\boldsymbol{\omega}^{\mathrm{m}_j}_{\mathrm{m}_j\mathrm{o}_j} = \boldsymbol{\omega}^{\mathrm{m}_j}_{\mathrm{m}_j\mathrm{I}} - \mathrm{T}^{\mathrm{m}_j}_{\mathrm{o}_j}\,\dot{\boldsymbol{\xi}}^{\mathrm{o}_j}_{\mathrm{o}_j} - \mathrm{T}^{\mathrm{m}_j}_{\mathrm{S}}\,\boldsymbol{\omega}^{\mathrm{S}}_{\mathrm{SI}}$$

which implies the following expression for the accelerations:

$$\begin{aligned}\dot{\boldsymbol{\omega}}^{\mathrm{m}_j}_{\mathrm{m}_j\mathrm{o}_j} &= \dot{\boldsymbol{\omega}}^{\mathrm{m}_j}_{\mathrm{m}_j\mathrm{I}} - \mathrm{T}^{\mathrm{m}_j}_{\mathrm{o}_j}\,\ddot{\boldsymbol{\xi}}^{\mathrm{o}_j}_{\mathrm{o}_j} - \mathrm{T}^{\mathrm{m}_j}_{\mathrm{S}}\,\dot{\boldsymbol{\omega}}^{\mathrm{S}}_{\mathrm{SI}} - \dot{\mathrm{T}}^{\mathrm{m}_j}_{\mathrm{o}_j}\,\dot{\boldsymbol{\xi}}^{\mathrm{o}_j}_{\mathrm{o}_j} - \dot{\mathrm{T}}^{\mathrm{m}_j}_{\mathrm{S}}\,\boldsymbol{\omega}^{\mathrm{S}}_{\mathrm{SI}} = \\ &= \dot{\boldsymbol{\omega}}^{\mathrm{m}_j}_{\mathrm{m}_j\mathrm{I}} - \mathrm{T}^{\mathrm{m}_j}_{\mathrm{o}_j}\,\ddot{\boldsymbol{\xi}}^{\mathrm{o}_j}_{\mathrm{o}_j} - \mathrm{T}^{\mathrm{m}_j}_{\mathrm{S}}\,\dot{\boldsymbol{\omega}}^{\mathrm{S}}_{\mathrm{SI}} + \boldsymbol{\omega}^{\mathrm{m}_j}_{\mathrm{m}_j\mathrm{o}_j} \times \mathrm{T}^{\mathrm{m}_j}_{\mathrm{o}_j}\,\dot{\boldsymbol{\xi}}^{\mathrm{o}_j}_{\mathrm{o}_j} + \boldsymbol{\omega}^{\mathrm{m}_j}_{\mathrm{m}_j\mathrm{I}} \times \mathrm{T}^{\mathrm{m}_j}_{\mathrm{S}}\,\boldsymbol{\omega}^{\mathrm{S}}_{\mathrm{SI}}\end{aligned}$$

Again Angular Momentum provides the relation for finding the inertial angular acceleration of the Test Mass:

$$\begin{aligned}\mathrm{J}_{\mathrm{m}_j}\,\dot{\boldsymbol{\omega}}^{\mathrm{m}_j}_{\mathrm{m}_j\mathrm{I}} &= \dot{\mathbf{H}}^{\mathrm{m}_j}_{\mathrm{m}_j\mathrm{I}} - \boldsymbol{\omega}^{\mathrm{m}_j}_{\mathrm{m}_j\mathrm{I}} \times \left(\mathrm{J}_{\mathrm{m}_j\mathrm{I}}\,\boldsymbol{\omega}^{\mathrm{m}_j}_{\mathrm{m}_j\mathrm{I}}\right) \\ \dot{\mathbf{H}}^{\mathrm{m}_j}_{\mathrm{m}_j\mathrm{I}} &= \mathrm{T}^{\mathrm{m}_j}_{\mathrm{o}_j}\left(\mathbf{M}^{\mathrm{o}_j}_{\mathrm{E}_j} + \mathbf{D}^{\mathrm{o}_j}_{\mathrm{E}_j} + \mathbf{M}^{\mathrm{o}_j}_{\mathrm{m}_j\mathrm{Stiff}}\right)\end{aligned}$$

where

- $\mathrm{J}_{\mathrm{m}_j}$ is the inertia matrix of the cubic Test Mass;
- $\mathbf{M}^{\mathrm{o}_j}_{\mathrm{E}_j}$ is the torque applied by the j-th GRS electrodes to the j-th Test Mass;
- $\mathbf{D}^{\mathrm{o}_j}_{\mathrm{E}_j}$ is the noise on the torque provided by the GRS electrodes;
- $\mathbf{M}^{\mathrm{o}_j}_{\mathrm{m}_j\mathrm{Stiff}} = \mathrm{J}_{\mathrm{m}_j}\,\boldsymbol{\alpha}^{\mathrm{o}_j}_{\mathrm{m}_j\mathrm{Stiff}}$ is the stiffness torque discussed in Sec. 2.6.1.

Overall the equations describing the Test Mass attitude are

$$\dot{\boldsymbol{\omega}}^{\mathrm{m}_j}_{\mathrm{m}_j\mathrm{o}_j} = \dot{\boldsymbol{\omega}}^{\mathrm{m}_j}_{\mathrm{m}_j\mathrm{I}} - \mathrm{T}^{\mathrm{m}_j}_{\mathrm{o}_j}\,\ddot{\boldsymbol{\xi}}^{\mathrm{o}_j}_{\mathrm{o}_j} - \mathrm{T}^{\mathrm{m}_j}_{\mathrm{S}}\,\dot{\boldsymbol{\omega}}^{\mathrm{S}}_{\mathrm{SI}} + \boldsymbol{\omega}^{\mathrm{m}_j}_{\mathrm{m}_j\mathrm{o}_j} \times \mathrm{T}^{\mathrm{m}_j}_{\mathrm{o}_j}\,\dot{\boldsymbol{\xi}}^{\mathrm{o}_j}_{\mathrm{o}_j} + \boldsymbol{\omega}^{\mathrm{m}_j}_{\mathrm{m}_j\mathrm{I}} \times \mathrm{T}^{\mathrm{m}_j}_{\mathrm{S}}\,\boldsymbol{\omega}^{\mathrm{S}}_{\mathrm{SI}} \tag{3.16}$$

$$\dot{\boldsymbol{\omega}}^{\mathrm{m}_j}_{\mathrm{m}_j\mathrm{I}} = \mathrm{J}^{-1}_{\mathrm{m}_j}\,\mathrm{T}^{\mathrm{m}_j}_{\mathrm{o}_j}\left(\mathbf{M}^{\mathrm{o}_j}_{\mathrm{E}_j} + \mathbf{D}^{\mathrm{o}_j}_{\mathrm{E}_j}\right) + \boldsymbol{\alpha}^{\mathrm{o}_j}_{\mathrm{m}_j\mathrm{Stiff}} - \mathrm{J}^{-1}_{\mathrm{m}_j}\,\boldsymbol{\omega}^{\mathrm{m}_j}_{\mathrm{m}_j\mathrm{I}} \times \left(\mathrm{J}_{\mathrm{m}_j\mathrm{I}}\,\boldsymbol{\omega}^{\mathrm{m}_j}_{\mathrm{m}_j\mathrm{I}}\right) \tag{3.17}$$

$$\ddot{\boldsymbol{\xi}}^{\mathrm{o}_j}_{\mathrm{o}_j} \quad \text{is given in Eq. 3.13}$$

$$\dot{\boldsymbol{\omega}}^{\mathrm{S}}_{\mathrm{SI}} \quad \text{is given in Eq. 3.9}$$

$$\mathrm{T}^{\mathrm{m}_j}_{\mathrm{o}_j} = \mathrm{R}(\mathfrak{q}^{*}_{\mathrm{m}_j}) \tag{3.18}$$

$$\mathrm{T}^{\mathrm{m}_j}_{\mathrm{S}} = \mathrm{T}^{\mathrm{m}_j}_{\mathrm{o}_j}\,\mathrm{T}^{\mathrm{o}_j}_{\mathrm{S}} \tag{3.19}$$

$$\mathrm{T}^{\mathrm{o}_j}_{\mathrm{S}} \quad \text{are given in Eq. 3.14, 3.15}$$

3.6 Test Mass Position

The SC position is not directly controlled. Instead, it is controlled by acting on the quantity $\boldsymbol{r}^{\mathrm{o}_j}_{\mathrm{m}_j\mathrm{o}_j}$. This position is actuated by the GRS electrodes only along the x and y directions inside the ORF. Along the Drag Free direction it is the SC itself that follows the Test Mass by using the MPS. This is done in order to reduce the actuation noise that affects the TM along that direction.

The relative position between the TM and the Spacecraft can be obtained by the inertial position $\boldsymbol{r}^{\mathrm{I}}_{\mathrm{m}_j\mathrm{I}}$ expressed as the sum of different offsets, as shown in Fig. 3.2:

$$\begin{aligned}\boldsymbol{r}^{\mathrm{I}}_{\mathrm{m}_j\mathrm{I}} &= \mathrm{T}^{\mathrm{I}}_{\mathrm{o}_j}\,\boldsymbol{r}^{\mathrm{o}_j}_{\mathrm{m}_j\mathrm{o}_j} + \mathrm{T}^{\mathrm{I}}_{\mathrm{o}_j}\,\boldsymbol{b}^{\mathrm{o}_j}_{\mathrm{m}} + \mathrm{T}^{\mathrm{I}}_{\mathrm{S}}\,\boldsymbol{b}^{\mathrm{S}}_{\mathrm{S}} + \boldsymbol{r}^{\mathrm{I}}_{\mathrm{SI}} \\ \boldsymbol{r}^{\mathrm{o}_j}_{\mathrm{m}_j\mathrm{o}_j} &= \mathrm{T}^{\mathrm{o}_j}_{\mathrm{I}}\,\boldsymbol{r}^{\mathrm{I}}_{\mathrm{m}_j\mathrm{I}} - \boldsymbol{b}^{\mathrm{o}_j}_{\mathrm{m}} - \mathrm{T}^{\mathrm{o}_j}_{\mathrm{S}}\,\boldsymbol{b}^{\mathrm{S}}_{\mathrm{S}} - \mathrm{T}^{\mathrm{o}_j}_{\mathrm{I}}\,\boldsymbol{r}^{\mathrm{I}}_{\mathrm{SI}}\end{aligned}$$

where

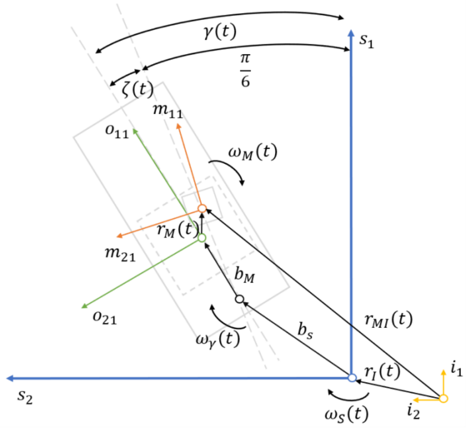

Figure 3.2: TM1 vector schema

- $\boldsymbol{b}_{\mathrm{m}}^{\mathrm{o}_j}$ is the position of the cage center with respect to the pivot point of the OA, in ORF coordinates;
- $\boldsymbol{b}_{\mathrm{S}}^{\mathrm{S}}$ is the position of the OA pivot point with respect to the Spacecraft's CoM;
- $\boldsymbol{r}_{\mathrm{SI}}^{\mathrm{I}}$ is the inertial position of the Spacecraft in the Heliocentric Inertial reference frame.

The relative velocity and acceleration of the TM can be found by taking successive time derivatives:

$$
\begin{aligned}
\dot{\boldsymbol{r}}_{\mathrm{m}_j\mathrm{o}_j}^{\mathrm{o}_j} &= \mathrm{T}_{\mathrm{I}}^{\mathrm{o}_j}\,\dot{\boldsymbol{r}}_{\mathrm{m}_j\mathrm{I}}^{\mathrm{I}} - \mathrm{T}_{\mathrm{I}}^{\mathrm{o}_j}\,\dot{\boldsymbol{r}}_{\mathrm{SI}}^{\mathrm{I}} - \boldsymbol{\omega}_{\mathrm{o}_j\mathrm{I}}^{\mathrm{o}_j} \times \mathrm{T}_{\mathrm{I}}^{\mathrm{o}_j}\left(\boldsymbol{r}_{\mathrm{m}_j\mathrm{I}}^{\mathrm{I}} - \boldsymbol{r}_{\mathrm{SI}}^{\mathrm{I}}\right) + \boldsymbol{\omega}_{\mathrm{o}_j\mathrm{S}}^{\mathrm{o}_j} \times \mathrm{T}_{\mathrm{S}}^{\mathrm{o}_j}\,\boldsymbol{b}_{\mathrm{S}}^{\mathrm{S}} = \\
&= \mathrm{T}_{\mathrm{I}}^{\mathrm{o}_j}\,\dot{\boldsymbol{r}}_{\mathrm{m}_j\mathrm{I}}^{\mathrm{I}} - \mathrm{T}_{\mathrm{I}}^{\mathrm{o}_j}\,\dot{\boldsymbol{r}}_{\mathrm{SI}}^{\mathrm{I}} - \boldsymbol{\omega}_{\mathrm{o}_j\mathrm{I}}^{\mathrm{o}_j} \times \boldsymbol{r}_{\mathrm{m}_j\mathrm{o}_j}^{\mathrm{o}_j} - \boldsymbol{\omega}_{\mathrm{o}_j\mathrm{I}}^{\mathrm{o}_j} \times \boldsymbol{b}_{\mathrm{m}}^{\mathrm{o}_j} - \mathrm{T}_{\mathrm{S}}^{\mathrm{o}_j}\,\boldsymbol{\omega}_{\mathrm{SI}}^{\mathrm{S}} \times \boldsymbol{b}_{\mathrm{S}}^{\mathrm{S}} \\
\ddot{\boldsymbol{r}}_{\mathrm{m}_j\mathrm{o}_j}^{\mathrm{o}_j} &= \mathrm{T}_{\mathrm{I}}^{\mathrm{o}_j}\left(\ddot{\boldsymbol{r}}_{\mathrm{m}_j\mathrm{I}}^{\mathrm{I}} - \ddot{\boldsymbol{r}}_{\mathrm{SI}}^{\mathrm{I}}\right) - \dot{\boldsymbol{\omega}}_{\mathrm{o}_j\mathrm{I}}^{\mathrm{o}_j} \times \boldsymbol{r}_{\mathrm{m}_j\mathrm{o}_j}^{\mathrm{o}_j} - \boldsymbol{\omega}_{\mathrm{o}_j\mathrm{I}}^{\mathrm{o}_j} \times \dot{\boldsymbol{r}}_{\mathrm{m}_j\mathrm{o}_j}^{\mathrm{o}_j} - \dot{\boldsymbol{\omega}}_{\mathrm{o}_j\mathrm{I}}^{\mathrm{o}_j} \times \boldsymbol{b}_{\mathrm{m}} + \\
&\quad + \boldsymbol{\omega}_{\mathrm{o}_j\mathrm{S}}^{\mathrm{o}_j} \times \mathrm{T}_{\mathrm{S}}^{\mathrm{o}_j}\left(\boldsymbol{\omega}_{\mathrm{SI}}^{\mathrm{S}} \times \boldsymbol{b}_{\mathrm{S}}^{\mathrm{S}}\right) - \mathrm{T}_{\mathrm{S}}^{\mathrm{o}_j}\,\dot{\boldsymbol{\omega}}_{\mathrm{SI}}^{\mathrm{S}} \times \boldsymbol{b}_{\mathrm{S}}^{\mathrm{S}} - \boldsymbol{\omega}_{\mathrm{o}_j\mathrm{I}} \times \mathrm{T}_{\mathrm{I}}^{\mathrm{o}_j}\left(\dot{\boldsymbol{r}}_{\mathrm{m}_j\mathrm{I}}^{\mathrm{I}} - \dot{\boldsymbol{r}}_{\mathrm{SI}}^{\mathrm{I}}\right) \\
\left(\dot{\boldsymbol{r}}_{\mathrm{m}_j\mathrm{I}}^{\mathrm{I}} - \dot{\boldsymbol{r}}_{\mathrm{SI}}^{\mathrm{I}}\right) &= \mathrm{T}_{\mathrm{o}_j}^{\mathrm{I}}\,\boldsymbol{\omega}_{\mathrm{o}_j\mathrm{I}}^{\mathrm{o}_j} \times \boldsymbol{r}_{\mathrm{m}_j\mathrm{o}_j}^{\mathrm{o}_j} + \mathrm{T}_{\mathrm{o}_j}^{\mathrm{I}}\,\dot{\boldsymbol{r}}_{\mathrm{m}_j\mathrm{o}_j}^{\mathrm{o}_j} + \mathrm{T}_{\mathrm{o}_j}^{\mathrm{I}}\,\boldsymbol{\omega}_{\mathrm{o}_j\mathrm{I}}^{\mathrm{o}_j} \times \boldsymbol{b}_{\mathrm{m}}^{\mathrm{o}_j} + \mathrm{T}_{\mathrm{S}}^{\mathrm{I}}\,\boldsymbol{\omega}_{\mathrm{SI}}^{\mathrm{S}} \times \boldsymbol{b}_{\mathrm{S}}^{\mathrm{S}} \\
\boldsymbol{\omega}_{\mathrm{o}_j\mathrm{I}}^{\mathrm{o}_j} &= \mathrm{T}_{\mathrm{S}}^{\mathrm{o}_j}\,\boldsymbol{\omega}_{\mathrm{SI}}^{\mathrm{S}} + \boldsymbol{\omega}_{\mathrm{o}_j\mathrm{S}}^{\mathrm{o}_j}
\end{aligned}
$$

Finally, by substituting and cancelling all the terms:

$$
\begin{aligned}
\ddot{\boldsymbol{r}}_{\mathrm{m}_j\mathrm{o}_j}^{\mathrm{o}_j} &= \mathrm{T}_{\mathrm{I}}^{\mathrm{o}_j}\left(\ddot{\boldsymbol{r}}_{\mathrm{m}_j\mathrm{I}}^{\mathrm{I}} - \ddot{\boldsymbol{r}}_{\mathrm{SI}}^{\mathrm{I}}\right) - 2\,\boldsymbol{\omega}_{\mathrm{o}_j\mathrm{I}}^{\mathrm{o}_j} \times \dot{\boldsymbol{r}}_{\mathrm{m}_j\mathrm{o}_j}^{\mathrm{o}_j} - \Omega(\boldsymbol{\omega}_{\mathrm{o}_j\mathrm{I}}^{\mathrm{o}_j})\,\boldsymbol{r}_{\mathrm{m}_j\mathrm{o}_j}^{\mathrm{o}_j} - \Omega(\boldsymbol{\omega}_{\mathrm{o}_j\mathrm{I}}^{\mathrm{o}_j})\,\boldsymbol{b}_{\mathrm{m}}^{\mathrm{o}_j} + \\
&\quad - \mathrm{T}_{\mathrm{S}}^{\mathrm{o}_j}\,\Omega(\boldsymbol{\omega}_{\mathrm{SI}}^{\mathrm{S}})\,\boldsymbol{b}_{\mathrm{S}}^{\mathrm{S}} \\
\Omega(\boldsymbol{\omega}_{\mathrm{o}_j\mathrm{I}}^{\mathrm{o}_j}) &= [\dot{\boldsymbol{\omega}}_{\mathrm{o}_j\mathrm{I}}^{\mathrm{o}_j}\times] + [\boldsymbol{\omega}_{\mathrm{o}_j\mathrm{I}}^{\mathrm{o}_j}\times]^2 \\
\Omega(\boldsymbol{\omega}_{\mathrm{SI}}^{\mathrm{S}}) &= [\dot{\boldsymbol{\omega}}_{\mathrm{SI}}^{\mathrm{S}}\times] + [\boldsymbol{\omega}_{\mathrm{SI}}^{\mathrm{S}}\times]^2
\end{aligned}
$$

where

- $-[\dot{\boldsymbol{\omega}}\times]$ represents the terms relative to the Euler force or Azimuthal force: a fictitious force acting in the inverse direction of the tangential velocity, generated from the angular acceleration of the Optical Assembly with respect to the inertial frame;
- $-[\boldsymbol{\omega}\times]^2$ represents the terms relative to the centrifugal force: a fictitious force pushing the TM radially away from an axis parallel to the axis of rotation of the OA and passing through the cage center;

- $-2\,[\boldsymbol{\omega}\times]$ represents the terms relative to the Coriolis force: a fictitious force acting always orthogonal to the motion of the Test Mass and to the axis of rotation of the OA.

The previous equations show the effects of rotating frames on the relative acceleration between Test Mass and Spacecraft. They suggest also that in order to reduce accelerations on the TMs due to OA and SC rotations, the quantities $\|\boldsymbol{b}_{\mathrm{m}}\|$ and $\|\boldsymbol{b}_{\mathrm{S}}\|$ should be as small as possible.

In order to derive a complete expression, the inertial accelerations have to be examined by using simple Newtonian mechanics. First the forces acting on the Test Mass:

$$\mathrm{m}_j\,\ddot{\boldsymbol{r}}^{\mathrm{I}}_{\mathrm{m}_j\mathrm{I}} = -\mu_{\odot}\,\frac{\mathrm{m}_j}{\left\|\boldsymbol{r}^{\mathrm{I}}_{\mathrm{m}_j\mathrm{I}}\right\|_2^3}\,\boldsymbol{r}^{\mathrm{I}}_{\mathrm{m}_j\mathrm{I}} - \mu_{\oplus}\,\frac{\mathrm{m}_j}{\left\|\boldsymbol{r}^{\mathrm{I}}_{\mathrm{m}_j\mathrm{I}}\right\|_2^3}\,\boldsymbol{r}^{\mathrm{I}}_{\mathrm{m}_j\mathrm{I}} + \mathrm{T}^{\mathrm{I}}_{\mathrm{o}_j}\left(\mathbf{F}^{\mathrm{o}_j}_{\mathrm{E}_j} + \mathbf{d}^{\mathrm{o}_j}_{\mathrm{E}_j} + \mathbf{F}^{\mathrm{o}_j}_{\mathrm{m}_j\mathrm{Stiff}}\right)$$

where

- $\mu_{\odot}$ and $\mu_{\oplus}$ are the Gravitational Parameters respectively of the Sun and the Earth;
- m_j is the mass of the j-th Test Mass;
- $\mathbf{d}^{\mathrm{o}_j}_{\mathrm{E}_j}$ is the disturbance on the force provided by the GRS electrodes;
- $\mathbf{F}^{\mathrm{o}_j}_{\mathrm{m}_j\mathrm{Stiff}} = \mathrm{m}_j\,\boldsymbol{a}^{\mathrm{o}_j}_{\mathrm{m}_j\mathrm{Stiff}}$ is the force applied by the Stiffness term discussed in Section 2.6.1.

Next the forces acting directly on the Spacecraft:

$$\begin{aligned}\mathrm{m}_{\mathrm{S}}\,\ddot{\boldsymbol{r}}^{\mathrm{I}}_{\mathrm{SI}} = {} & -\mu_{\odot}\,\frac{\mathrm{m}_{\mathrm{S}}}{\|\boldsymbol{r}^{\mathrm{I}}_{\mathrm{SI}}\|_2^3}\,\boldsymbol{r}^{\mathrm{I}}_{\mathrm{SI}} - \mu_{\oplus}\,\frac{\mathrm{m}_{\mathrm{S}}}{\|\boldsymbol{r}^{\mathrm{I}}_{\mathrm{SI}}\|_2^3}\,\boldsymbol{r}^{\mathrm{I}}_{\mathrm{SI}} - \sum_{j=1,2}\mathrm{T}^{\mathrm{I}}_{\mathrm{o}_j}\left(\mathbf{F}^{\mathrm{o}_j}_{\mathrm{E}_j} + \mathbf{d}^{\mathrm{o}_j}_{\mathrm{E}_j}\right) + \\ & + \mathrm{T}^{\mathrm{I}}_{\mathrm{S}}\left(\mathbf{F}^{\mathrm{S}}_{\mathrm{T}} + \mathbf{d}^{\mathrm{S}}_{\odot\mathrm{press}} + \mathbf{F}^{\mathrm{S}}_{\mathrm{met}}\right) - \dot{\mathrm{m}}_{\mathrm{S}}\,\dot{\boldsymbol{r}}^{\mathrm{S}}_{\mathrm{SI}}\end{aligned}$$

where

- $\mathbf{F}^{\mathrm{S}}_{\mathrm{T}}$ is the force generated by the thrusters;
- $\mathbf{d}^{\mathrm{S}}_{\odot\mathrm{press}}$ is the force generated by the Solar pressure discussed in Section 2.6.2;
- $\mathbf{F}^{\mathrm{S}}_{\mathrm{met}}$ is the force generated by the Meteoroid Impact.

In addition, the following simplifying assumptions have been made:

1. $\dot{\mathrm{m}}_{\mathrm{S}}/\mathrm{m}_{\mathrm{S}} \approx 0$ because in science mode, during the main mission phase, the amount of thruster propellant expelled at any given instant is very low, because it is used only to apply small corrections;
2. perturbations due to Earth's gravity have been considered approximately zero in [9];
3. the *Gravity Gradient* has been approximated in the following way:

$$-\mu_{\odot}\left(\frac{\boldsymbol{r}^{\mathrm{I}}_{\mathrm{m}_j\mathrm{I}}}{\left\|\boldsymbol{r}_{\mathrm{m}_j\mathrm{I}}\right\|_2^3} - \frac{\boldsymbol{r}^{\mathrm{I}}_{\mathrm{SI}}}{\|\boldsymbol{r}^{\mathrm{I}}_{\mathrm{SI}}\|_2^3}\right) \approx \mathrm{k_g}\,\Delta\boldsymbol{r}^{\mathrm{I}}_{\mathrm{SI}}$$

   where $\Delta\boldsymbol{r}^{\mathrm{I}}_{\mathrm{SI}}$ is a small displacement vector.

The final equations are

$$\begin{aligned}
\ddot{\boldsymbol{r}}^{\mathrm{o}_j}_{\mathrm{m}_j\mathrm{o}_j} &= \mathrm{T}^{\mathrm{o}_j}_{\mathrm{I}}\,\mathrm{k_g}\,\Delta\boldsymbol{r}^{\mathrm{I}}_{\mathrm{SI}} + \frac{1}{\mathrm{m}_j}\left(\mathbf{F}^{\mathrm{o}_j}_{\mathrm{E}_j} + \mathbf{d}^{\mathrm{o}_j}_{\mathrm{E}_j}\right) + \boldsymbol{a}^{\mathrm{o}_j}_{\mathrm{m}_j\mathrm{Stiff}} - \frac{1}{\mathrm{m_S}}\,\mathrm{T}^{\mathrm{o}_j}_{\mathrm{S}}\left(\mathbf{F}^{\mathrm{S}}_{\mathrm{T}} + \mathbf{d}^{\mathrm{S}}_{\odot\mathrm{press}} + \mathbf{F}^{\mathrm{S}}_{\mathrm{met}}\right) + \\
&\quad + \frac{1}{\mathrm{m_S}}\sum_{i=1,2}\mathrm{T}^{\mathrm{o}_j}_{\mathrm{o}_i}\left(\mathbf{F}^{\mathrm{o}_i}_{\mathrm{E}_i} + \mathbf{d}^{\mathrm{o}_i}_{\mathrm{E}_i}\right) - \Omega(\boldsymbol{\omega}^{\mathrm{o}_j}_{\mathrm{o}_j\mathrm{I}})\,\boldsymbol{b}^{\mathrm{o}_j}_{\mathrm{m}} - \mathrm{T}^{\mathrm{o}_j}_{\mathrm{S}}\,\Omega(\boldsymbol{\omega}^{\mathrm{S}}_{\mathrm{SI}})\,\boldsymbol{b}^{\mathrm{S}}_{\mathrm{S}} - 2\,\boldsymbol{\omega}^{\mathrm{o}_j}_{\mathrm{o}_j\mathrm{I}} \times \dot{\boldsymbol{r}}^{\mathrm{o}_j}_{\mathrm{m}_j\mathrm{o}_j} + \\
&\quad - \Omega(\boldsymbol{\omega}^{\mathrm{o}_j}_{\mathrm{o}_j\mathrm{I}})\,\boldsymbol{r}^{\mathrm{o}_j}_{\mathrm{m}_j\mathrm{o}_j} && (3.20)\\
\Omega(\boldsymbol{\omega}^{\mathrm{o}_j}_{\mathrm{o}_j\mathrm{I}}) &= [\dot{\boldsymbol{\omega}}^{\mathrm{o}_j}_{\mathrm{o}_j\mathrm{I}}\times] + [\boldsymbol{\omega}^{\mathrm{o}_j}_{\mathrm{o}_j\mathrm{I}}\times]^2 && (3.21)\\
\Omega(\boldsymbol{\omega}^{\mathrm{S}}_{\mathrm{SI}}) &= [\dot{\boldsymbol{\omega}}^{\mathrm{S}}_{\mathrm{SI}}\times] + [\boldsymbol{\omega}^{\mathrm{S}}_{\mathrm{SI}}\times]^2 && (3.22)\\
\boldsymbol{\omega}^{\mathrm{o}_j}_{\mathrm{o}_j\mathrm{I}} &= \mathrm{T}^{\mathrm{o}_j}_{\mathrm{S}}\,\boldsymbol{\omega}^{\mathrm{S}}_{\mathrm{SI}} + \boldsymbol{\omega}^{\mathrm{o}_j}_{\mathrm{o}_j\mathrm{S}} && (3.23)\\
\boldsymbol{\omega}^{\mathrm{o}_j}_{\mathrm{o}_j\mathrm{S}} &= \dot{\boldsymbol{\xi}}^{\mathrm{o}_j}_{j} && (3.24)\\
\boldsymbol{\omega}^{\mathrm{S}}_{\mathrm{SI}} &\quad \text{given in Eq. 3.9}\\
\mathrm{T}^{\mathrm{o}_j}_{\mathrm{I}} &= \mathrm{T}^{\mathrm{o}_j}_{\mathrm{S}}\,\mathrm{T}^{\mathrm{S}}_{\mathrm{I}} && (3.25)\\
\mathrm{T}^{\mathrm{o}_j}_{\mathrm{S}} &\quad \text{are given in Eq. 3.14,3.15}\\
\mathrm{T}^{\mathrm{o}_2}_{\mathrm{o}_1} &= \mathrm{T}^{\mathrm{o}_1\,\top}_{\mathrm{o}_2} = \mathrm{T}^{\mathrm{o}_2}_{\mathrm{S}}\,\mathrm{T}^{\mathrm{o}_1\,\top}_{\mathrm{S}} && (3.26)\\
\mathrm{T}^{\mathrm{o}_1}_{\mathrm{o}_2} &= \mathrm{T}^{\mathrm{o}_2\,\top}_{\mathrm{o}_1} = \mathrm{T}^{\mathrm{o}_1}_{\mathrm{S}}\,\mathrm{T}^{\mathrm{o}_2\,\top}_{\mathrm{S}} && (3.27)
\end{aligned}$$

3.7 Linearized Model

The DFAC System was designed by means of the mixed sensitivity H_∞ design. Therefore, it is based on the linearized plant.

The linearized plant can be obtained from the nonlinear model by neglecting the nonlinear terms and by linearizing all coordinate transformations.
In addition, instead of considering a whole three dimensional vector for the angular position of each Optical Assembly, only one scalar variable ξ is used. Indeed the vector $\boldsymbol{\xi}^{\mathrm{o}_j}_{j}$ has always the same structure, with the first two components equal to zero and the last one that determines its norm. The breathing angle effect requires the whole OA inter-angle to vary of $\pm1^\circ$ per year. This implies that each of the telescopes needs to independently rotate of the same amount each year, with opposite signs. For this reason the following relations hold true:

$$\begin{aligned}
\xi &= \xi_1 = -\xi_2\\
\dot{\xi} &= \dot{\xi}_1 = -\dot{\xi}_2\\
\mathbf{M}_{\mathrm{OA}} &= \mathbf{M}_{\mathrm{OA}_1} = -\mathbf{M}_{\mathrm{OA}_2}
\end{aligned}$$

This simplification assumes that the OA assemblies will be rotated by the controller in such a way to only follow the breathing angles, and not, for example, to correct other rotations or disturbances. In other words, the OA actuation is only partially exploited, because it is just assigned with the task of tracking the nominal varying angles. This is part of the decoupling principle applied during the design process of the DFACS in [3], that will explained later in this section. If, on one hand, this technique leads to an extreme simplification of the design procedure, on the other hand, it could also limit the control effectiveness in certain situations, such as a meteoroid impact, when it could be handy to slightly adjust the OA rotations in order to better track the moving lasers coming from the other Spacecrafts in the formation.

The state is defined by the vectors

$$\begin{aligned}
\boldsymbol{p} &= \left(\boldsymbol{q}_{\mathrm{SC}},\ \boldsymbol{r}^{\mathrm{o}_1}_{\mathrm{m}_1\mathrm{o}_1},\ \boldsymbol{q}_{\mathrm{m}_1\mathrm{o}_1},\ \boldsymbol{r}^{\mathrm{o}_2}_{\mathrm{m}_2\mathrm{o}_2},\ \boldsymbol{q}_{\mathrm{m}_2\mathrm{o}_2},\ \xi\right), \quad \boldsymbol{p} \in \mathbb{R}^{16} \\
\boldsymbol{v} &= \left(\boldsymbol{\omega}^{\mathrm{S}}_{\mathrm{SC}},\ \dot{\boldsymbol{r}}^{\mathrm{o}_1}_{\mathrm{m}_1\mathrm{o}_1},\ \boldsymbol{\omega}^{\mathrm{o}_1}_{\mathrm{m}_1\mathrm{o}_1},\ \dot{\boldsymbol{r}}^{\mathrm{o}_2}_{\mathrm{m}_2\mathrm{o}_2},\ \boldsymbol{\omega}^{\mathrm{o}_2}_{\mathrm{m}_2\mathrm{o}_2},\ \dot{\xi}\right), \quad \boldsymbol{v} \in \mathbb{R}^{16} \\
\boldsymbol{x} &= \begin{bmatrix} \boldsymbol{p} \\ \boldsymbol{v} \end{bmatrix}, \quad \boldsymbol{x} \in \mathbb{R}^{32}
\end{aligned}$$

and the input vector by

$$\begin{aligned}
\boldsymbol{u} &= \left(\mathbf{F}^{\mathrm{S}}_{\mathrm{T}},\ \mathbf{M}^{\mathrm{S}}_{\mathrm{T}},\ \mathbf{f}^{\mathrm{o}_1}_{\mathrm{E}_1},\ \mathbf{M}^{\mathrm{o}_1}_{\mathrm{E}_1},\ \mathbf{f}^{\mathrm{o}_2}_{\mathrm{E}_2},\ \mathbf{M}^{\mathrm{o}_2}_{\mathrm{E}_2},\ M^{\mathrm{S}}_{\mathrm{OA}}\right), \quad \boldsymbol{u} \in \mathbb{R}^{17} \\
\mathbf{f}^{\mathrm{o}_j}_{\mathrm{E}_j} &= \begin{bmatrix} 0 & 1 & 0 \\ 0 & 0 & 1 \end{bmatrix} \mathbf{F}^{\mathrm{o}_j}_{\mathrm{E}_j}, \quad \mathbf{f}^{\mathrm{o}_j}_{\mathrm{E}_j} \in \mathbb{R}^2
\end{aligned}$$

where the electrode along the direction $\boldsymbol{o}_1$ is not employed to apply a force on the TM's CoM.
The linearization of the quaternion derivative is simply:

$$\dot{\boldsymbol{q}} \approx \frac{1}{2}\boldsymbol{\omega}$$

and the linearization of the coordinate transformations:

$$\bar{\mathrm{T}}^{\mathrm{o}_1}_{\mathrm{S}} = \mathrm{R}_z(-\frac{\pi}{6}) \tag{3.28}$$

$$\bar{\mathrm{T}}^{\mathrm{o}_2}_{\mathrm{S}} = \mathrm{R}_z(\frac{\pi}{6}) \tag{3.29}$$

$$\bar{\mathrm{T}}^{\mathrm{o}_1}_{\mathrm{o}_2} = \mathrm{R}_z(-\frac{\pi}{3}) \tag{3.30}$$

$$\bar{\mathrm{T}}^{\mathrm{o}_2}_{\mathrm{o}_1} = \mathrm{R}_z(\frac{\pi}{3}) \tag{3.31}$$

The final state space representation of the linear model is

$$\dot{\boldsymbol{x}} = \begin{bmatrix} \dot{\boldsymbol{p}} \\ \dot{\boldsymbol{v}} \end{bmatrix} = \begin{bmatrix} A_{pp} & A_{pv} \\ A_{vp} & A_{vv} \end{bmatrix} \boldsymbol{x} + \begin{bmatrix} 0 \\ \mathrm{B}_v \end{bmatrix} \boldsymbol{u} \tag{3.32}$$

$$A_{pp} = 0$$

$$A_{pv} = \begin{bmatrix} \frac{1}{2}\,\mathrm{I}_3 & 0 & 0 & 0 & 0 & 0 \\ 0 & \mathrm{I}_3 & 0 & 0 & 0 & 0 \\ 0 & 0 & \frac{1}{2}\,\mathrm{I}_3 & 0 & 0 & 0 \\ 0 & 0 & 0 & \mathrm{I}_3 & 0 & 0 \\ 0 & 0 & 0 & 0 & \frac{1}{2}\,\mathrm{I}_3 & 0 \\ 0 & 0 & 0 & 0 & 0 & 1 \end{bmatrix}$$

$$A_{vp} = \begin{bmatrix} 0 & 0 & 0 & 0 & 0 & 0 \\ 0 & \mathrm{STT} & \mathrm{STR} & 0 & 0 & 0 \\ 0 & \mathrm{SRT} & \mathrm{SRR} & 0 & 0 & 0 \\ 0 & 0 & 0 & \mathrm{STT} & \mathrm{STR} & 0 \\ 0 & 0 & 0 & \mathrm{STT} & \mathrm{STR} & 0 \\ 0 & 0 & 0 & 0 & 0 & -\frac{\mathrm{k}_\xi}{\mathrm{I}_{zz}} \end{bmatrix}$$

$$A_{vv} = \begin{bmatrix} 0 & \mathbf{0} \\ \mathbf{0}^\top & -\frac{\beta}{\mathrm{I}_{zz}} \end{bmatrix}$$

$$B_v = \begin{bmatrix} 0 & \mathrm{J}_\mathrm{S}^{-1} & -\mathrm{J}_\mathrm{S}^{-1}\,\boldsymbol{b}_1 \times \bar{\mathrm{T}}_{\mathrm{o}_1}^{\mathrm{S}} P^\top & -\mathrm{J}_\mathrm{S}^{-1}\,\bar{\mathrm{T}}_{\mathrm{o}_1}^{\mathrm{S}} & -\mathrm{J}_\mathrm{S}^{-1}\,\boldsymbol{b}_2 \times \bar{\mathrm{T}}_{\mathrm{o}_2}^{\mathrm{S}} P^\top & -\mathrm{J}_\mathrm{S}^{-1}\,\bar{\mathrm{T}}_{\mathrm{o}_2}^{\mathrm{S}} & 0 \\ -\mathrm{m}_\mathrm{S}^{-1}\bar{\mathrm{T}}_{\mathrm{S}}^{\mathrm{o}_1} & 0 & (\mathrm{m}_\mathrm{S}^{-1} + \mathrm{m}_\mathrm{M}^{-1})P^\top & 0 & \mathrm{m}_\mathrm{S}^{-1}\bar{\mathrm{T}}_{\mathrm{o}_2}^{\mathrm{o}_1} P^\top & 0 & 0 \\ 0 & 0 & 0 & \mathrm{J}_\mathrm{M}^{-1} & 0 & 0 & 0 \\ -\mathrm{m}_\mathrm{S}^{-1}\bar{\mathrm{T}}_{\mathrm{S}}^{\mathrm{o}_2} & 0 & \mathrm{m}_\mathrm{S}^{-1}\bar{\mathrm{T}}_{\mathrm{o}_1}^{\mathrm{o}_2} P^\top & 0 & (\mathrm{m}_\mathrm{S}^{-1} + \mathrm{m}_\mathrm{M}^{-1})P^\top & 0 & 0 \\ 0 & 0 & 0 & 0 & 0 & \mathrm{J}_\mathrm{M}^{-1} & 0 \\ 0 & 0 & 0 & 0 & 0 & 0 & \frac{1}{\mathrm{I}_{zz}} \end{bmatrix}$$

$$P = \begin{bmatrix} 0 & 1 & 0 \\ 0 & 0 & 1 \end{bmatrix}$$

4 | DFACS Controller

In this Chapter the DFAC System designed in [3] is briefly presented, with particular emphasis on the architectural aspects that are relevant for the work of this thesis.

The DFAC System was already in place and this Thesis builds on top of it. It performs both the *drag–free* control and the Spacecraft attitude control, during the Science phase of the mission, when the actual gravitational wave detection takes place. The *drag–free* control is the task of controlling the SC's position and the TM's attitude and position simultaneously, in such a way to ensure a drag–free movement of both TMs along their respective geodesics. It has to take into account the disturbances affecting the three bodies and reject them within the requirements reported in the SoW. While the SC Attitude control is the task of correctly rotating the SC in order to be able to maintain laser contact with the satellite formation during the whole mission.

4.1 Decoupled Architecture

One of the main difficulties in designing this DFACS system was the large number of coupled degrees of freedom of the complex multi–body system (SC + TMs + OAs). In order to reduce this complexity, a special decoupled architecture is employed.

Typically, a decoupled architecture would consist in a series of parallel SISO controllers, each of which would control a single DoF; then, each of the signals would be multiplied by a *decoupling matrix* that yields the final commands $\boldsymbol{u}$ to be forwarded to the actuators. For example, a possible *decoupling matrix* in this case could be the pseudo-inverse of B_v:

$$B_v^{\dagger} = B_v^{\top} \, (B_v \, B_v^{\top})^{-1} \, \in \mathbb{R}^{17,16} \; : \; B_v \, B_v^{\dagger} = I_{16}$$

where 16 SISO controllers would generate a command vector $\boldsymbol{u}_{\mathrm{SISO}} \in \mathbb{R}^{16}$ (one for each DoF to be controlled), then to obtain the 17 actuator commands $\boldsymbol{u}$, the decoupling product would be performed $\boldsymbol{u} = B_v^{\dagger} \, \boldsymbol{u}_{\mathrm{SISO}} \in \mathbb{R}^{17}$.

Nonetheless, in the specific case of this DFAC system, there were additional constraints on the actuators, that prevented the application of such a simple decoupling approach. Specifically, there is a constraint that prevents the position of the TMs along the z-axis to be controlled only by the GRS electrodes in High Resolution mode. The way it was designed forces the average TM height to be controlled by means of the MPS thrusters and the differential TM height to be controlled by the GRS electrodes; the average and differential heights are defined in the following way:

$$z_{avg} = \frac{z_{m_1} + z_{m_2}}{2}$$
$$z_{diff} = \frac{z_{m_1} - z_{m_2}}{2}$$

Another constraint prevents the control of the TM's position along the x-axis (*drag–free direction*) through the GRS electrodes: it can only be performed by using the thrusters.

In order to fulfill all these constraints and to keep as much decoupling as possible, an optimization problem has been solved. The problem has been slightly simplified by noticing that the Optical Assemblies are already completely decoupled from the rest of the DoFs in the linearized model, as can be seen in Eq. 3.32. For this reason we can define a smaller matrix B'_v, such that $B_v = \begin{bmatrix} B'_v & 0 \\ 0 & \mathrm{I}_{zz}^{-1} \end{bmatrix}$, with $B'_v \in \mathbb{R}^{15,16}$. The optimization problem returns as a result the matrix $B^i_v \in \mathbb{R}^{16,15}$. The relationships between the DFACS controller outputs and the decoupled actuator inputs are reported here:

$$
\begin{aligned}
\mathrm{F}_{\mathrm{T}_x} &= -355.3605\, u_{x_1} - 355.3605\, u_{x_2} \\
\mathrm{F}_{\mathrm{T}_y} &= -549.659\, u_{x_1} + 549.659\, u_{x_2} \\
\mathrm{F}_{\mathrm{T}_z} &= -783.0415\, u_{z_{avg}} \\
\mathbf{M}_{\mathrm{T}} &= \begin{bmatrix} 790 & 0 & 0 \\ 0 & 780 & 0 \\ 0 & 0 & 980 \end{bmatrix} \boldsymbol{u}_{\theta SC} \\
\mathrm{F}_{E_{1_x}} &= \mathrm{F}_{E_{2_x}} = 0 \\
\mathrm{F}_{E_{1_y}} &= 1.9574\, u_{y_1} - 0.0013\, u_{y_2} \\
\mathrm{F}_{E_{1_z}} &= 1.96\, u_{z_{diff}} \\
\mathrm{F}_{E_{2_y}} &= 1.9574\, u_{y_2} - 0.0013\, u_{y_1} \\
\mathrm{F}_{E_{2_z}} &= -1.96\, u_{z_{diff}} \\
\mathbf{M}_{E_1} &= 6.9123 \cdot 10^{-4}\, I_3\, \boldsymbol{u}_{\theta m_1} \\
\mathbf{M}_{E_2} &= 6.9123 \cdot 10^{-4}\, I_3\, \boldsymbol{u}_{\theta m_2}
\end{aligned}
$$

where

- u_{x_i}, u_{y_i}, $i = 1, 2$ are the commands from the TM's x and y position SISO controllers;
- $u_{z_{avg}}$, $u_{z_{diff}}$ are the commands from the average and differential TM height controllers;
- $\boldsymbol{u}_{\theta SC}$ are the commands from the SC attitude controllers;
- $\boldsymbol{u}_{\theta m_1}, \boldsymbol{u}_{\theta m_2}$ are the commands from the TMs attitude controllers.

4.2 SISO Controllers

The DFAC System employs a total of 16 SISO LTI controllers, obtained from the *mixed–sensitivity* H^∞ procedure, in order to fulfill all the requirements contained into the SoW. The exact details of the design procedure can be found in [3]. In this Section, they are presented in general, with a focus on the correspondence between sensor signals and controllers.

All controllers have been designed in the continuous domain and then discretized afterwards at 10 Hz, with the Tustin method, that allows to keep the frequency response the closest to the continuous version.

4.2.1 Spacecraft Attitude Control

During Science mode the constellation is maintained and the lasers are always used as a source for the SC attitude control, because the SC–SC DWS sensors are very accurate and have fast sampling frequencies. The main goal of managing the SC's attitude is to keep these sensors in their operating ranges, that is, to maintain laser contact between satellites. This can be achieved by solving two distinct control problems:

1. the SC attitude control, actuated by the MPS thrusters;
2. the OA inter–angle control, actuated by a specific motor.

As concerns the first problem, it is handled by 3 SISO LTI controllers. They have 16 internal states and are not strictly proper systems (D matrix is not zero). The error signal, used as input to the controller, is the vector part of the error quaternion $\mathfrak{q}_{SC}$, that represents the rotation from the desired inertial Spacecraft attitude $\mathfrak{q}_{CI}$ to the real inertial attitude $\mathfrak{q}_{SI}$. The $\mathfrak{q}_{CS}$ quaternion (inverse w.r.t. the error signal) is computed online by starting from the angles measured by the SC–SC DWS sensors and then following the steps of the algorithm shown in Section 3.1.

The second problem is handled by a single SISO LTI controller. It is a second order system, also not strictly proper. The reference angle is the nominal pulsating inter–telescope angle and is assumed to be modelled by a sine wave with amplitude 0.5° and angular frequency of $2.2856 \cdot 10^{-7}$ rad/s. The error signal, used as input to the controller, is simply the difference between the reference value and the actual value measured by an ad hoc sensor.

4.2.2 Drag–Free Control

The Drag–Free Control is divided into different control problems:

1. the TM position control;
2. the SC position control, that happens indirectly as a byproduct of the previous task;
3. the TM attitude control.

The first problem is managed by six different SISO controllers in total: two for each TM's x and y axis translations and two for the average and differential heights. The reference signals are all zeros, that is the goal is to keep the TMs in the center of the cage, at the origin of their frame of reference. The measurements of the x-axis translation for each TM, comes from the respective local SC–TM interferometer. While the measurements of the y and z axis translations for each TM, comes from the GRS electrodes, that can act both as actuators and sensors, as explained in Section 2.3.

The second problem is indirectly solved by distributing the control output signals coming from the TM position controllers across the MPS thrusters and the GRS electrodes. A critical aspect here is that if there happens to be an unmodeled constant disturbance acting on one of the TMs along the x-axis (drag–free direction), given that there is no actuator directly acting on the TM along this direction, the SC will find itself "following" the drifting TM, with no force counteracting this movement.

As regards the third control problem, it is handled by six SISO LTI controllers (three for each TM). The error signal used as input to the controllers is the vector part of the conjugate of the TM attitude quaternion $\mathbf{q}^*_{m_i}$. The attitude of the Test Mass during science mode is measured by mixing the internal SC–TM DWS laser measurements (more accurate and fast) with the GRS electrodes measurements. Specifically, the internal SC–TM DWS can output the pitch and yaw angles, but not the roll angle, that is taken from the GRS.

4.3 Simulation

In this Section a series of results with plots, taken from a simulation of the DFAC System designed in [3], are shown in order to give the full picture of the performances achieved before going into the issue of meteoroid impacts. The simulation was done via Simulink r2019b, with the fixed–step ode-4 solver (Runge-Kutta), step–size equal to 0.01 s and duration of 10000 s.

Figure 4.1a shows the SC attitude rotation error signal, converted to rotation vector $\boldsymbol{\theta}_{SC}$ or, equivalently, to Roll–Pitch–Yaw angles. A constant steady–state error on the y-axis is visible from this simulation. This is due to the particular initial orientation of the Spacecraft and the constant term of the Solar pressure, that is constantly pushing on it. The counteracting torque from the SC attitude controller can be seen both from the direct output in Fig. 4.3a and from the torque applied by the MPS system on the spacecraft's center of mass, Fig. 4.4b.

Figure 4.1b shows the tracking error signal of one of the OAs.

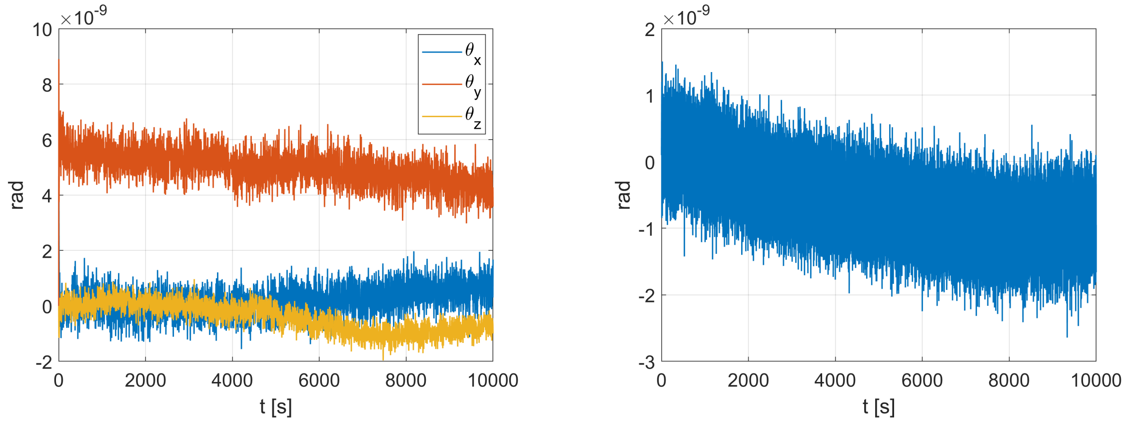

(a) SC attitude w.r.t. CRF $\boldsymbol{\theta}_{SC}$ (b) OA angle tracking error

Figure 4.1: DFACS – SC Attitude Control System

Figure 4.2 shows the position and the attitude converted to rotation vector $\boldsymbol{\theta}_{\mathrm{m}_i\mathrm{o}_i}$, for both TMs.

Figure 4.3 shows all the outputs from the SISO LTI controllers in the DFAC System. These output are the ones that get combined by the *decoupling matrix* to generate the commands for the actuators, as illustrated in Section 4.1.

Figure 4.4 shows the outputs from all of the actuators available on the Spacecraft.

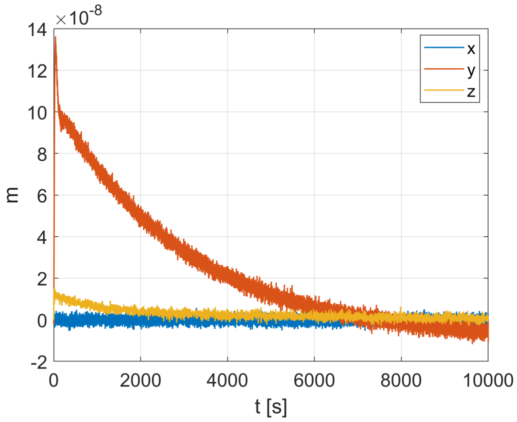

(a) TM1 position w.r.t. ORF1 $\boldsymbol{r}_{\mathrm{m_1o_1}}^{\mathrm{o_1}}$

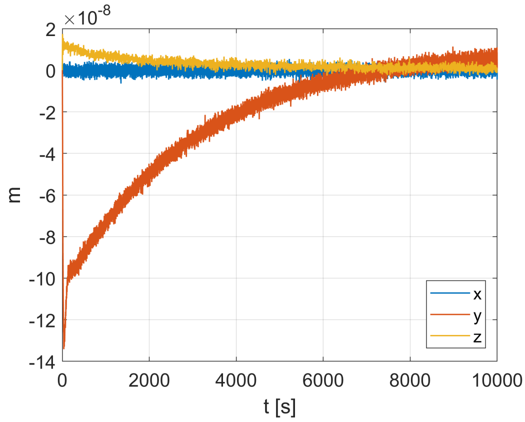

(b) TM2 position w.r.t. ORF2 $\boldsymbol{r}_{\mathrm{m_2o_2}}^{\mathrm{o_2}}$

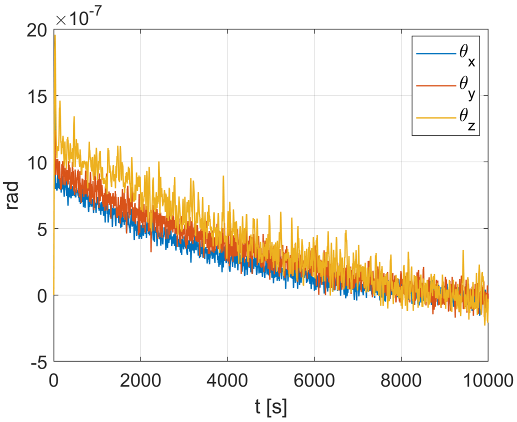

(c) TM1 attitude w.r.t. ORF1 $\boldsymbol{\theta}_{\mathrm{m_1o_1}}$

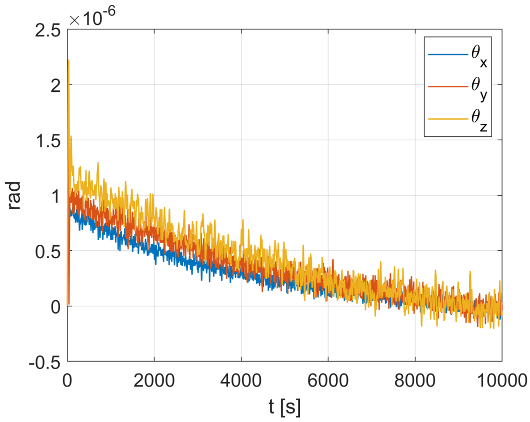

(d) TM2 attitude w.r.t. ORF2 $\boldsymbol{\theta}_{\mathrm{m_2o_2}}$

Figure 4.2: DFACS – Drag–Free Control

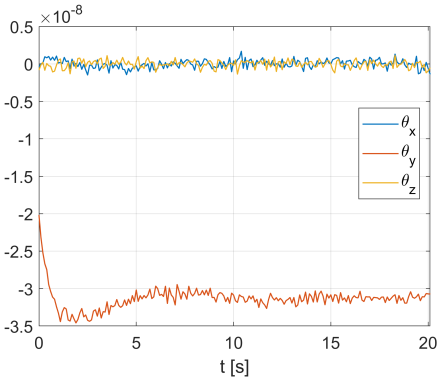

(a) SC attitude control

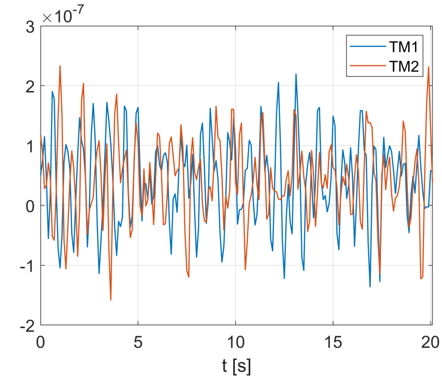

(b) TM x position control

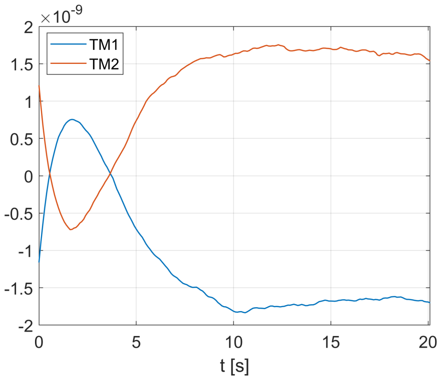

(c) TM y position control

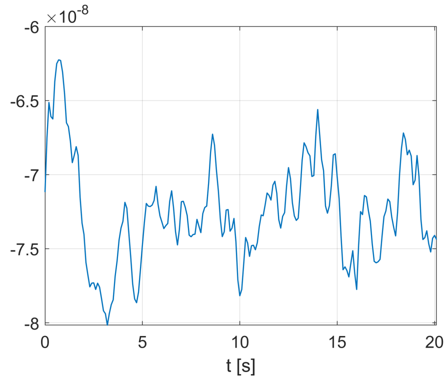

(d) TM average z position control

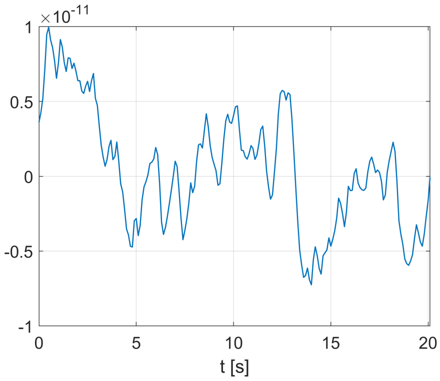

(e) TM differential z position control

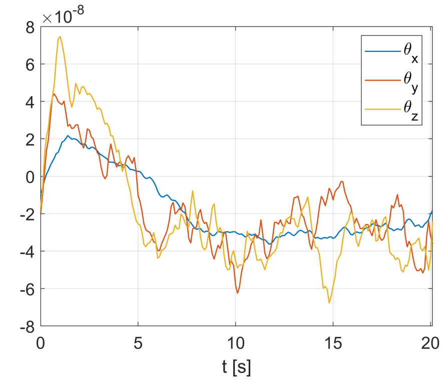

(f) TM1 attitude control

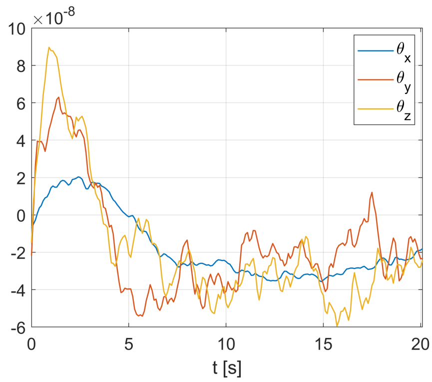

(g) TM2 attitude control

Figure 4.3: DFACS – SISO LTI controllers outputs

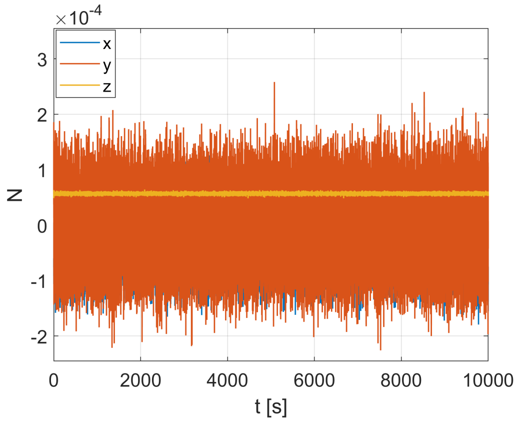

(a) MPS force

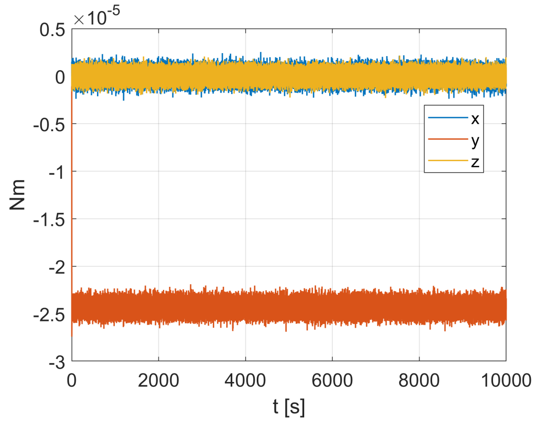

(b) MPS torque

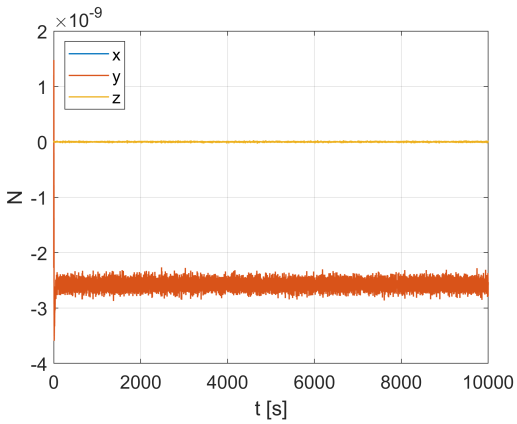

(c) GRS1 force on TM1

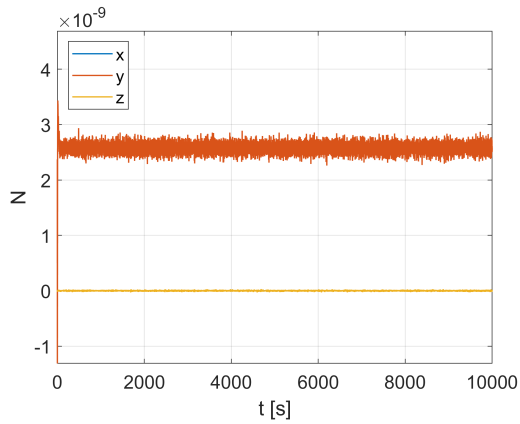

(d) GRS2 force on TM2

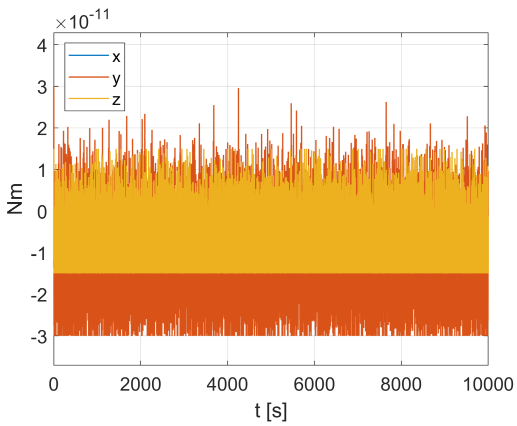

(e) GRS1 torque on TM1

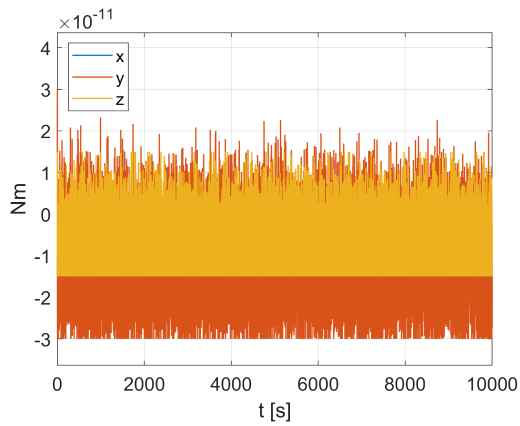

(f) GRS2 torque on TM2

Figure 4.4: DFACS – Saturated actuator commands to the plant

5 | Meteoroid Impact Analysis

This Chapter describes the first step of the work of this thesis. First an analysis of the available meteoroid data is performed, in order to characterize the type of meteoroid objects that are of concern for this mission, according to the ESA. Then the task of extending the dataset with labels is solved.

One major goal has been to come up with efficient ways to label the data. Labeling process consists in categorizing each meteoroid impact according to its convergence properties and laser loss behavior. As regards convergence labels, an analysis of the convergence boundaries of the system already in place (DFAC System) is conducted, in order to establish some approximated classification thresholds, to reduce the number of impacts for which a complete simulation is required. Finally, the laser loss problem is analyzed, and again data is labelled following an efficient, but approximated approach, refined by complete simulations on a smaller dataset.

5.1 Data Analysis

After the preliminary study that was conducted in [3], briefly presented in Section 2.6.3, the conclusion was that for the majority of impacts, the DFAC System, already active during Science mode, was sufficient to keep the whole system convergent and under control. In rare cases these impacts were strong enough to cause divergence issues and force the controller to switch back to the Constellation Acquisition phase. The problem with reacquiring the constellation is that this process is forced to be very slow, with an acquisition time that can be of several hours. Nonetheless, the critical impacts were thought to be rare enough to not justify an ad–hoc recovery system.

Later on, ESA sent new data with updated meteoroid impacts that can be expected during the orbits designed for the LISA mission. This new data dramatically changed the situation, because it contained numerous high–energy impacts that would require the whole system to perform a complete laser link re-acquisition maneuver. If the mission were to be interrupted every time by a strong impact requiring several hours of recovery, then a non negligible percentage of the mission's time and money would be wasted in recovery, instead of the actual gravitational wave detection process.

The data from ESA consists of 219728 impacts, each one described by the following features:

1. *Particle Linear Momentum* p: the norm of the linear momentum of the particle;
2. *Transferred Linear Momentum* $\boldsymbol{p}_i$: the linear momentum transferred to the SC during impact, along each axis;
3. *Transferred Angular Momentum* $\boldsymbol{H}_i$: the angular momentum transferred to the SC during impact, along each axis;

4. *Speed Variation* Δv: the variation in the norm of the particle's speed due to impact;

5. *Angular Speed Variation* $\Delta\omega$: the variation in the norm of the particle's angular speed due to impact;

6. *Impact Point* $\boldsymbol{r}_i$: the impact point on the outer surface of the Spacecraft.

All vectors are in SRF coordinates, hence the missing S superscript.

A first set of information, that can be inferred easily from this data, concerns the shape of the Spacecraft. Figure 5.3 shows all the impact points contained in the file from ESA from different points of view.

A sanity check has been performed in order to confirm that the transferred angular momentum reported in the file is obtained as the cross product of the transferred linear momentum and the impact position: $\boldsymbol{H}_i = \boldsymbol{r}_i \times \boldsymbol{p}_i$. This implies that, depending on the impact location, the SC could experience high torques due to the points that are further away from the SC's center of mass. Particularly, the top solar panel and the bottom antenna are critical points in this regard.

The main quantities affecting the SC are the transferred linear and angular momenta. These features span several order of magnitude, for this reason the impacts were first grouped using this criteria. Different signs are treated as different groups. Table 5.1 reports them in detail.

		Number of Cases					
Id	Range	p_x	p_y	p_z	H_x	H_y	H_z
G_7^-	$[-10^{-2}; -10^{-3})$	29	35	183	164	60	54
G_6^-	$[-10^{-3}; -10^{-4})$	296	362	1393	967	809	355
G_5^-	$[-10^{-4}; -10^{-5})$	1745	1687	4922	3507	3186	2274
G_4^-	$[-10^{-5}; -10^{-6})$	6492	6137	11785	8528	8063	7451
G_3^-	$[-10^{-6}; -10^{-7})$	12781	12943	14571	13489	12598	13011
G_2^-	$[-10^{-7}; -10^{-8})$	15392	13287	18999	17637	17110	15796
G_1^-	$[-10^{-8}; -10^{-9})$	19116	18499	24869	18250	19324	19167
G_0	$[-10^{-9}; 10^{-9}]$	110054	110696	89421	89032	96773	104099
G_1	$(10^{-9}; 10^{-8}]$	18199	20079	16265	20101	19833	18924
G_2	$(10^{-8}; 10^{-7}]$	14550	15225	15553	18639	17040	15364
G_3	$(10^{-7}; 10^{-6}]$	12421	12424	12325	13936	12813	12925
G_4	$(10^{-6}; 10^{-5}]$	6302	6111	6599	9727	8042	7277
G_5	$(10^{-5}; 10^{-4}]$	1911	1942	2319	4434	3255	2406
G_6	$(10^{-4}; 10^{-3}]$	426	295	455	1157	721	584
G_7	$(10^{-3}; 10^{-2}]$	14	6	54	153	86	41

Table 5.1: Impact grouping by order of magnitude of transferred momenta

As can be seen clearly from Figure 5.1, that shows the distribution of impacts across the groups, most of the transferred momenta are in the range of group G_0, that represents orders of $\pm 10^{-10}$ and smaller. These are very low–energy impacts and do not cause any convergence issues.

Figure 5.2 shows, on a per group basis, the percentage distribution on the three x, y and z axis. A few remarks can be drawn from it:

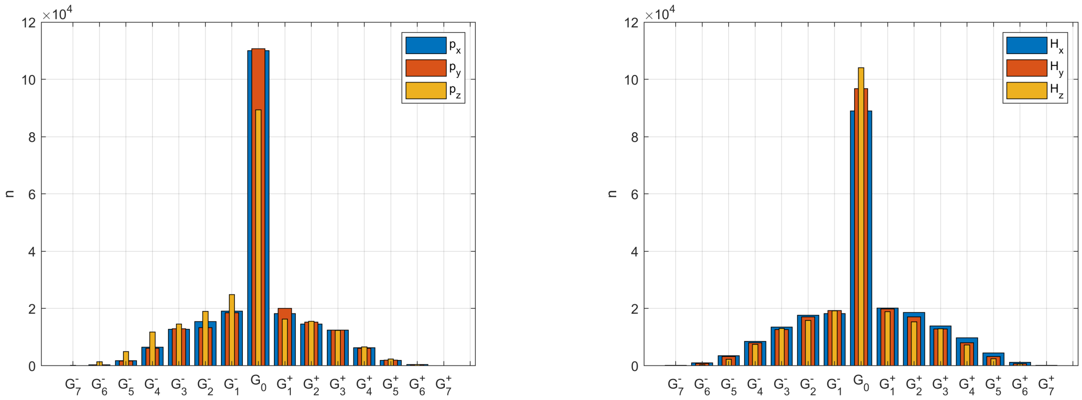

(a) Transferred Linear Momentum (b) Transferred Angular Momentum

Figure 5.1: Samples count for each impact group

1. most of the stronger hits in the negative axis directions (-x, -y and -z) transfer the linear momentum along the -z direction, this is mainly due to the wide solar panel on the top of the Spacecraft (area $\approx 13.5\,\mathrm{m}^2$);
2. among the stronger hits in the positive axis directions (+x, +y and +z) the linear momentum transfer are more evenly spread out, even if a slight preference for the +z direction can be observed for the most powerful impacts;
3. most of the stronger impacts transfer angular momentum along the x axis, this again is due to the long rectangular solar panel, that when hit on the border furthest from the SC's CoM offers a long rotation arm to the meteoroid, exerting higher torques on the SC's x axis.

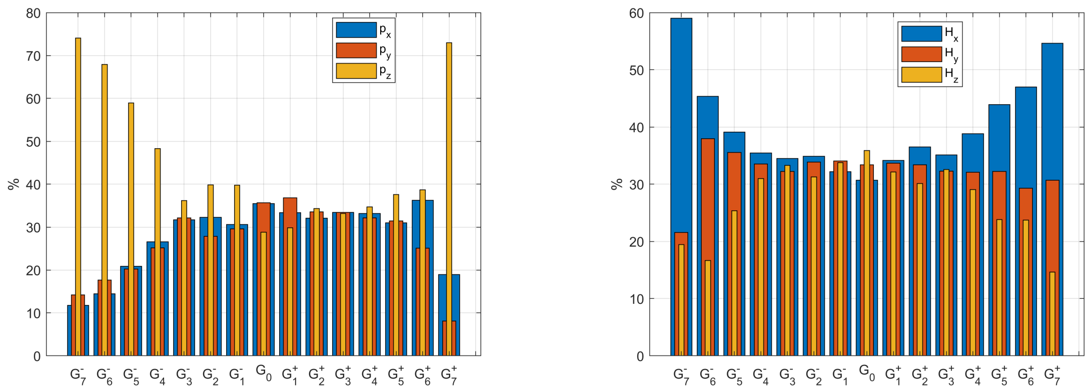

(a) Transferred Linear Momentum (b) Transferred Angular Momentum

Figure 5.2: Percentage distribution on the three axis for each group

5.2 Convergence Boundaries

Within the context of data labeling, a first categorization of the impacts is done according to the convergence properties, that is, if an impact causes or not divergence and, if it does, in what parts of the system.

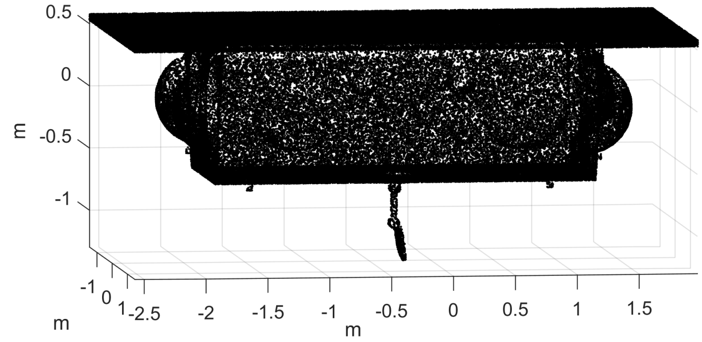

(a) Perspective

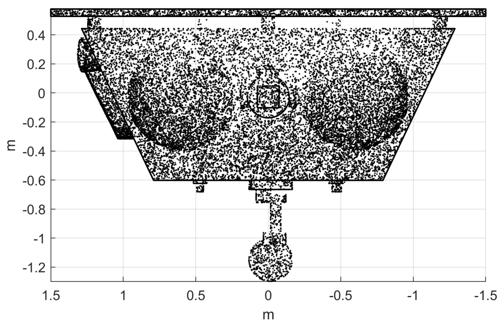

(b) Left side

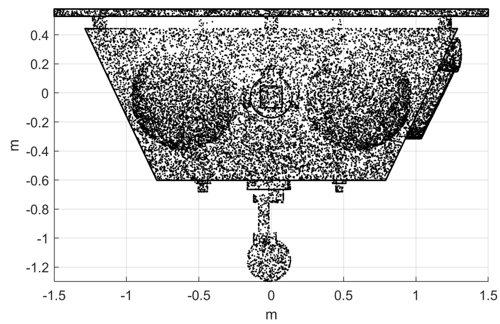

(c) Right side

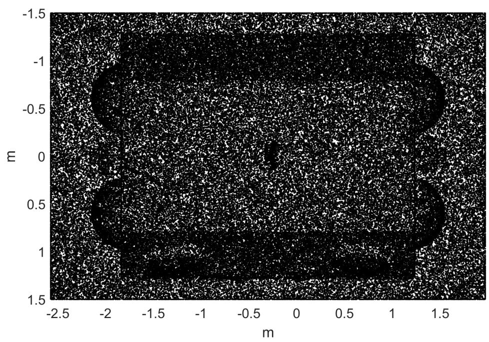

(d) Top side

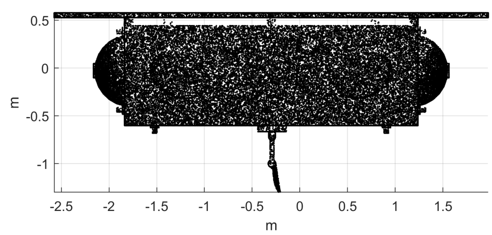

(e) Front side

Figure 5.3: Impact points from the ESA file

One approach would be to start a complete simulation for each impact contained in the database, but this would require a huge amount of time, considering that a simulation of 1000 s requires approximately from 20 to 70 seconds, that (in the best case) would require in total slightly more than 50 days of continuous simulations.

The approach followed in this Section is to explore the convergence boundaries of the simulator itself by pushing it to the limits of convergence with artificial impact values and then infer from these some approximate thresholds to be used for fast impact classification. Then, most of the impacts can be classified immediately using these thresholds and only a small fraction will need a complete simulation in order to be classified.

In all simulations the impacts happen at instant $t_i = 500\,\mathrm{s}$, a time window that allows any initial transient effect to dissipate before impact.

ESA did not provide any information regarding impact duration. Therefore, a duration of $\Delta t_i = 0.1\,\mathrm{s}$ has been assumed, even if, tests with different duration values suggest that this quantity does not affect in a relevant way the simulation results. Indeed, the shorter the duration the greater the force and torque exerted by the meteoroid on the SC's CoM, but these great force and torque are then applied for shorter time intervals, making it almost equivalent to a slightly larger impact duration, with smaller force and torque, but applied for a longer time.

By experimenting with the impacts the following preliminary remarks can be made:

1. if the Spacecraft's attitude becomes divergent, then the whole system becomes divergent over time, including the Test Masses, in short:
   SC attitude divergent $\implies$ TM attitude and position divergent;
2. if the Spacecraft's attitude remains convergent, then the TM's attitude will remain convergent too, for both TMs, in short:
   SC attitude convergent $\implies$ TM attitude convergent;
3. if the Spacecraft's attitude remains convergent, the TM's position can still become divergent over time, due to the linear momentum transferred by the meteoroid.

These remarks suggest mainly two ideas: that there is some degree of separation between the attitude divergence problem and the position divergence one and that the SC attitude and TM attitude are strongly coupled, from a convergence point of view, thus could be treated as a single critical factor in the convergence analysis.

Figure 5.5 shows some relevant signals taken from a simulation of one of the strongest impacts, having the following features: impact id 1, $\boldsymbol{p}_i = \begin{bmatrix} -2.5 & -0.9 & 14.9 \end{bmatrix}^\top \cdot 10^{-3}\,\mathrm{Ns}$, $\boldsymbol{H}_i = \begin{bmatrix} -4 & 19.9 & 0.6 \end{bmatrix}^\top \cdot 10^{-3}\,\mathrm{Nms}$ and $\boldsymbol{r}_i^{\mathrm{S}} = \begin{bmatrix} -1.421 & -0.301 & 0.528 \end{bmatrix}^\top\,\mathrm{m}$. The impact point for this meteoroid is on the border of the solar panel, generating a large torque in the +y rotation direction, as shown in Figure 5.4.

5.2.1 SC and TM Attitude Convergence Boundary

First step of the analysis is to find the convergence boundaries for the SC attitude.

A preliminary remark that simplifies this analysis is that the SC's attitude convergence is almost not affected (or affected very little) by the linear momentum transferred during impact. This can also be seen from Equation 3.9, where the only terms indirectly affected by the linear momentum are

$$-\mathrm{J}_{\mathrm{S}}^{-1}\,\boldsymbol{b}_1^{\mathrm{S}} \times \left(\mathrm{T}_{\mathrm{o}_1}^{\mathrm{S}}\,\mathbf{F}_{\mathrm{E}_1}^{\mathrm{o}_1}\right) - \mathrm{J}_{\mathrm{S}}^{-1}\,\boldsymbol{b}_2^{\mathrm{S}} \times \left(\mathrm{T}_{\mathrm{o}_2}^{\mathrm{S}}\,\mathbf{F}_{\mathrm{E}_2}^{\mathrm{o}_2}\right)$$

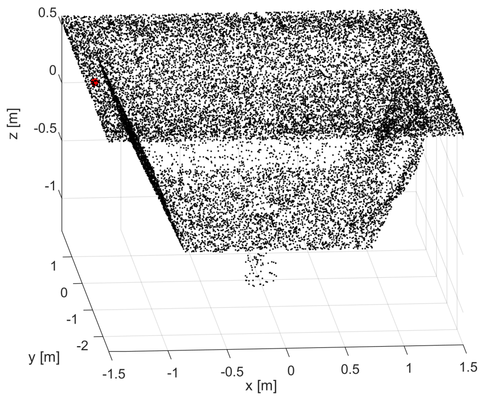

Figure 5.4: Meteoroid (id 1) impact point (red dot)

where $\mathbf{F}_{\mathrm{E}_1}^{\mathrm{o}_1}$ and $\mathbf{F}_{\mathrm{E}_2}^{\mathrm{o}_2}$ are the forces generated by the two GRSs on the TMs, that try to compensate the transferred linear momentum while controlling the TMs' positions. In Fig. 5.5g the saturation limits of the GRS force are visible:

$$\left\|\mathbf{F}_{\mathrm{E}_j}^{\mathrm{o}_j}\right\|_\infty < 6 \cdot 10^{-9}\,\mathrm{N} \implies \left\|\mathbf{F}_{\mathrm{E}_j}^{\mathrm{o}_j}\right\|_2 < \approx 1.0392 \cdot 10^{-8}\,\mathrm{N},\ j = 1,2$$

this also puts an approximate bound on how large these two aforementioned terms can be in norm:

1. $\left\|\boldsymbol{b}_j^{\mathrm{S}} \times \left(\mathrm{T}_{\mathrm{o}_j}^{\mathrm{S}}\,\mathbf{F}_{\mathrm{E}_j}^{\mathrm{o}_j}\right)\right\|_2 \le \left\|\boldsymbol{b}_j^{\mathrm{S}}\right\|_2 \left\|\mathbf{F}_{\mathrm{E}_j}^{\mathrm{o}_j}\right\|_2 < 1.0392 \cdot 10^{-8} \left\|\boldsymbol{b}_j^{\mathrm{S}}\right\|_2$
2. $\left\|\boldsymbol{b}_j^{\mathrm{S}}\right\|_2 < 5 \cdot 10^{-1}\,\mathrm{m}$

$$(1) + (2) \implies \left\|\boldsymbol{b}_j^{\mathrm{S}} \times \left(\mathrm{T}_{\mathrm{o}_j}^{\mathrm{S}}\,\mathbf{F}_{\mathrm{E}_j}^{\mathrm{o}_j}\right)\right\|_2 < \approx 5.1962 \cdot 10^{-9}$$

Furthermore, considering that the SC's inertia matrix J_S is nearly diagonal, it can be assumed that

$$\mathrm{J}_\mathrm{S}^{-1} \approx \begin{bmatrix} 1.3 & 0 & 0 \\ 0 & 1.3 & 0 \\ 0 & 0 & 1 \end{bmatrix} \cdot 10^{-3}\,\mathrm{kg}^{-1}$$

it can be noticed that a product by the $\mathrm{J}_\mathrm{S}^{-1}$ matrix will further reduce the euclidean norm of the vectors contained in the terms above.

To summarize, even after one of the strongest impacts available in the dataset, the maximum order of magnitude of the acceleration terms due to the GRS forces, trying to counteract the transferred linear momentum, is 10^{-9} or less. All other terms in the SC attitude dynamics do not depend on the linear momentum of the meteoroid. The angular momenta involved in the loss of convergence, that will be explored later in this Section, are increased with steps of order 10^{-5} Nms and will involve impact torques of order 10^{-4} Nm (assumed impact duration 0.1 s). For this reason it is reasonable to conduct the exploration process by fixing the impact transferred linear momentum and only varying the transferred angular momentum, thus reducing the dimensionality of the search.

As already stated, the exploration process consists of simulating different artificial impacts, with fixed transferred linear momentum $\boldsymbol{p}_i$, and variable transferred angular

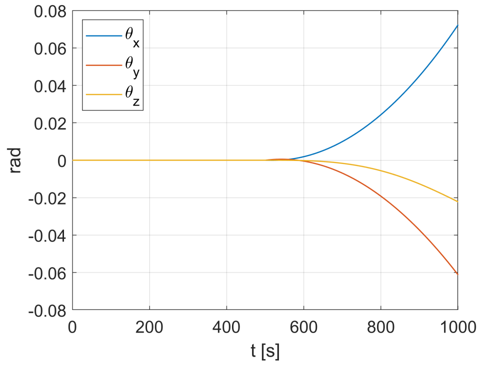

(a) SC attitude w.r.t. constellation frame

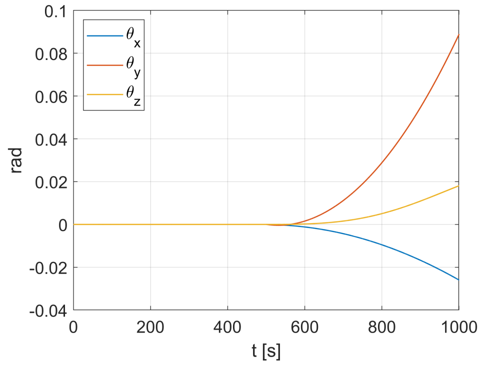

(b) TM1 attitude

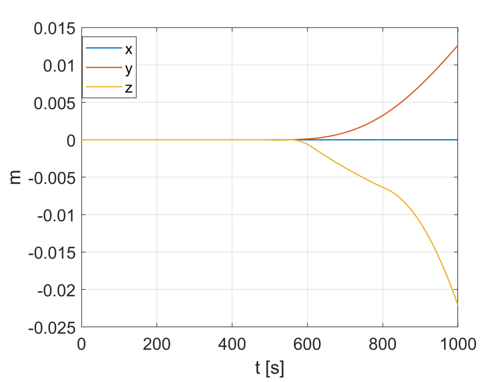

(c) TM1 position

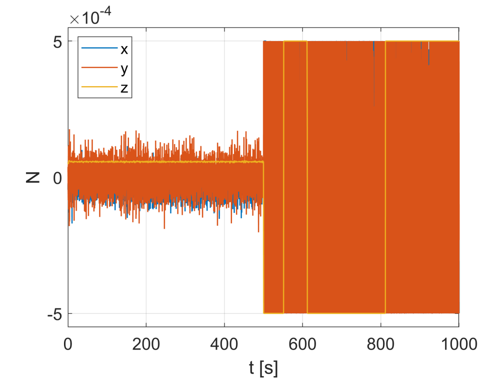

(d) Force output by MPS thrusters

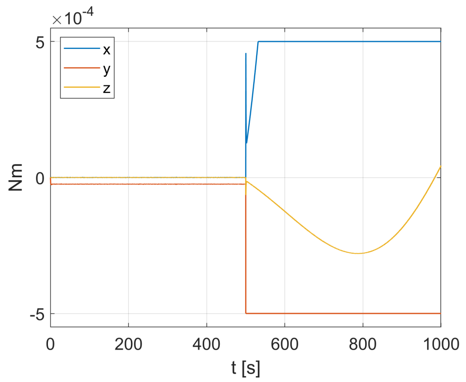

(e) Torque output by MPS thrusters

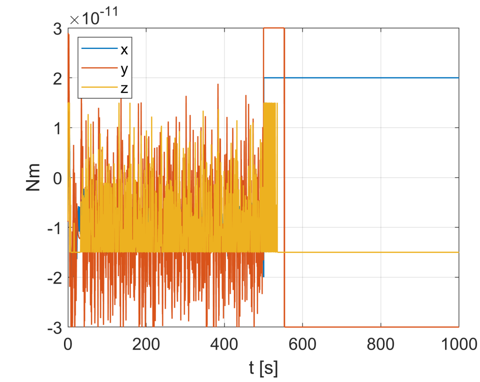

(f) Torque output by GRS1 electrodes

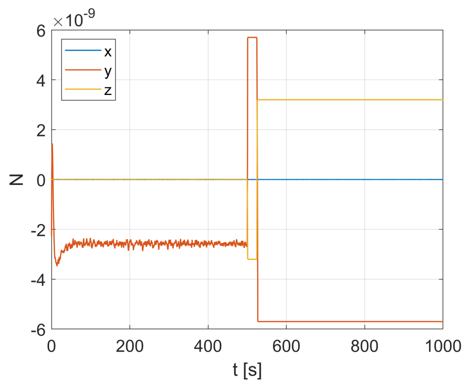

(g) Force output by GRS1 electrodes

Figure 5.5: Strong impact simulation of DFAC System

momentum $\boldsymbol{H}_i$. As regards the fixed $\boldsymbol{p}_i$, a worst–case value has been used. Specifically, the value of the meteoroid impact with id 1, one of the strongest impacts available in the dataset: $\boldsymbol{p}_i = \begin{bmatrix}-2.5 & -0.9 & 14.9\end{bmatrix}^\top \cdot 10^{-3}\,\text{Ns}$. The search is performed by varying $\boldsymbol{H}_i$, one component at a time. First, the starting value should be a vector that keeps the SC's attitude convergent, found by simulation: $\boldsymbol{H}_i = \begin{bmatrix}1 & 1 & 1\end{bmatrix}^\top \cdot 10^{-3}\,\text{Nms}$; then, three iterations follow (one for each component of $\boldsymbol{H}_i$), where, each component is increased by steps of value $0.01 \cdot 10^{-3}\,\text{Nms}$, until divergence is reached.

The first outcome of this exploratory procedure is that the coupling between the degrees of freedom is negligible with this value of step size; in other words, each axis has an independent convergence boundary, when we consider increments of $0.01 \cdot 10^{-3}\,\text{Nms}$, and the value of transferred angular momentum along the other axis has no influence. So, for example, from a SC's attitude convergence standpoint, $\boldsymbol{H}_i = \begin{bmatrix}2.83 & 0 & 0\end{bmatrix}^\top \cdot 10^{-3}\,\text{Nms}$ is equivalent to $\boldsymbol{H}_i = \begin{bmatrix}2.83 & 2.83 & 3.5\end{bmatrix}^\top \cdot 10^{-3}\,\text{Nms}$.

The second outcome is that there does not appear to be any difference in changing the rotation direction, or equivalently changing the sign of the transferred momentum, with this step size value.

Finally, the convergence boundary on the SC's attitude found by simulation is

$$|\boldsymbol{H}_i| = \begin{bmatrix}|H_{ix}| \\ |H_{iy}| \\ |H_{iz}|\end{bmatrix} \leq \boldsymbol{H}_i^* = \begin{bmatrix}2.87 \\ 2.83 \\ 3.53\end{bmatrix} \cdot 10^{-3}\,\text{Nms} \tag{5.1}$$

As expected the boundary is larger for the z-axis, where the Spacecraft's inertia is higher, so it can withstand a higher angular momentum transfer.

Having found the SC Attitude convergence boundary one can label all the impacts by applying the following implications:

1. $|\boldsymbol{H}_i| \leq \boldsymbol{H}_i^* \implies$ SC Attitude convergent $\implies$ TM Attitude convergent
2. $\exists j \in \{1,2,3\} \,:\, |H_{i_j}| \geq H_{i_j}^* + 10^{-5} \implies$ SC Attitude divergent $\implies$ TM Attitude and Position divergent

Luckily enough, both these rules cover the entire dataset and do not leave out any impact, so for the label *SC Attitude Convergence* and *TM Attitude Convergence* no complete simulation is required.

5.2.2 TM Position Convergence Boundary

In labeling impacts based on the *TM Position Convergence* property, the initial simplification regarding the separation between transferred angular and linear momenta, already used in the previous labeling process, does not fully apply. For angular momenta with values near to the attitude convergence boundary, both the transferred angular and linear momenta can influence the *TM Position Convergence* property, thus, in general, one can not analyze them independently.

Nonetheless, some simplifications can still be made. In particular, with the previously found threshold $\boldsymbol{H}_i^*$ for the *SC Attitude convergence* property, it is possible to already label the few impacts (only 89 in total), that correspond to divergent SC attitude, as divergent also in TM position. This is due to the simulation result number 1 presented at the beginning of Section 5.2, which states that when the SC's attitude becomes divergent, every part of it becomes divergent.

For the remaining impacts, which have convergent SC attitude, the transferred angular momentum is kept fixed to a convergent value of $\boldsymbol{H}_i^* = \begin{bmatrix}2 & 2 & 3\end{bmatrix} \cdot 10^{-3}\,\mathrm{Nms}$, that simulations show not to influence the convergence boundary on the linear momentum.

Again, the boundary search has been conducted by increasing $\boldsymbol{p}_i$ with steps of size $10^{-5}\,\mathrm{Ns}$, until divergence is reached, starting from convergent values (found by simulation) of $\begin{bmatrix}1 & 1 & 1\end{bmatrix}^\top \cdot 10^{-3}\,\mathrm{Ns}$.

With this step size and slightly lower angular momentum values, the coupling between the degrees of freedom is negligible for the linear momentum, thus, each DoF can be explored independently.

An additional issue is that depending on the sign of the component of $\boldsymbol{p}_i$ that is being explored the value of the boundary can vary. For this reason a conservative boundary is estimated by taking the smallest among the ones found with both positive and negative signs, for each axis.

The conservative convergence boundary is

$$|\boldsymbol{p}_i| \leq \boldsymbol{p}_i^* = \begin{bmatrix}5.93\\5.69\\3.35\end{bmatrix} \cdot 10^{-3}\,\mathrm{Ns} \quad \text{when} \quad |\boldsymbol{H}_i| \leq \begin{bmatrix}2\\2\\3\end{bmatrix} \cdot 10^{-3}\,\mathrm{Nms} \tag{5.2}$$

The impacts for which a complete simulation is required are 54 (less than 0.03% of the dataset), of which 47, that transfer an angular momentum too close to the convergence boundary, plus additional 7 impacts, for which there is at least a component of $\boldsymbol{p}_i$ that exceeds the conservative threshold.

5.2.3 Incoming Laser Loss

Another useful label to assign to each impact, is whether it is strong enough to make the SC lose the incoming laser beams (at least one of the two). The SC will lose the incoming beam when at least one among the azimuth or elevation angles exceeds the $2\,\mu\mathrm{rad}$ threshold.

The problem can be analyzed by focusing only on the transferred angular momentum, because the influence of the linear momentum is negligible, as shown at the start of Section 5.2.1.

Unfortunately, the threshold on each axis of the angular momentum are coupled together, that is, the threshold on one axis will be higher or lower depending on the momentum values along the other axis.

First the maximum boundaries for each axis are found by setting the momentum on the other axis to zero, leading to the following values: $1.75 \cdot 10^{-3}\,\mathrm{Nms}$ for x axis, $1.26 \cdot 10^{-3}\,\mathrm{Nms}$ for y axis and $1.35 \cdot 10^{-3}\,\mathrm{Nms}$ for z axis. A new vector is defined by these values:

$$\boldsymbol{H}_i^{\ell_i} = \begin{bmatrix}1.75\\1.26\\1.35\end{bmatrix} \cdot 10^{-3}\,\mathrm{Nms} \tag{5.3}$$

Then all combinations of values on the three axis are tested by simulation, 300 in total. The ranges tested for each axis are the following:

$$H_{i_x} \in \{0.8 \cdot 10^{-3},\, 0.9 \cdot 10^{-3},\, 1 \cdot 10^{-3},\, \ldots,\, 1.7 \cdot 10^{-3}\}$$
$$H_{i_y} \in \{0.8 \cdot 10^{-3},\, 0.9 \cdot 10^{-3},\, 1 \cdot 10^{-3},\, 1.1 \cdot 10^{-3},\, 1.2 \cdot 10^{-3}\}$$
$$H_{i_z} \in \{0.8 \cdot 10^{-3},\, 0.9 \cdot 10^{-3},\, 1 \cdot 10^{-3},\, 1.1 \cdot 10^{-3},\, 1.2 \cdot 10^{-3},\, 1.3 \cdot 10^{-3}\}$$

where each set is obtained with increments of $0.1 \cdot 10^{-3}$ Nms. With these known data samples two norm spheres are fitted on the data: one that encloses only convergent values and one that excludes only divergent values. The two radius values are $r^{\mathrm{s}} = 1.57 \cdot 10^{-3}$, the convergent sphere, and $r^{\mathrm{u}} = 1.95 \cdot 10^{-3}$, the sphere that excludes only divergent points. So by applying the following implications most impacts can already be labeled:

1. $|\boldsymbol{H}_i| \leq \boldsymbol{H}_i^{\ell_i} \wedge \|\boldsymbol{H}_i\|_2 \leq r^{\mathrm{s}} \implies$ no incoming laser loss
2. $\exists\, j \in \{1, 2, 3\} \,:\, |H_{i_j}| > H_{i_j}^{\ell_i} \vee \|\boldsymbol{H}_i\|_2 > r^{\mathrm{u}} \implies$ incoming laser loss

A total of 53 impacts are not covered by these rules and require a complete simulation.

5.2.4 Outgoing Laser Loss

The last categorization of impacts that was considered is the outgoing laser loss label. The outgoing laser is lost when at least one among SC2 and SC3 cannot receive the laser coming from SC1, assuming the point of view is on SC1. This happens when the absolute rotation angle between the outgoing laser beam and the incoming one is greater than $1\,\mu$rad, as illustrated in Figure 2.9.

The procedure is analogous to the previous one for the incoming laser loss property. First, the maximum thresholds are found separately for each axis, leading to the following new vector:

$$\boldsymbol{H}_i^{\ell_o} = \begin{bmatrix} 1.19 \\ 0.82 \\ 0.88 \end{bmatrix} \cdot 10^{-3}\,\mathrm{Nms} \tag{5.4}$$

Then all combinations of values on the three axis are tested by simulation, 200 in total. The ranges tested for each axis are the following:

$$\begin{aligned}
H_{i_x} &\in \{0.4 \cdot 10^{-3},\, 0.5 \cdot 10^{-3},\, 0.6 \cdot 10^{-3},\, \ldots,\, 1.1 \cdot 10^{-3}\} \\
H_{i_y} &\in \{0.4 \cdot 10^{-3},\, 0.5 \cdot 10^{-3},\, 0.6 \cdot 10^{-3},\, 0.7 \cdot 10^{-3},\, 0.8 \cdot 10^{-3}\} \\
H_{i_z} &\in \{0.4 \cdot 10^{-3},\, 0.5 \cdot 10^{-3},\, 0.6 \cdot 10^{-3},\, 0.7 \cdot 10^{-3},\, 0.8 \cdot 10^{-3}\}
\end{aligned}$$

where each set is obtained with increments of $0.1 \cdot 10^{-3}$ Nms. With these known data samples two norm spheres are fitted on the data: one that encloses only convergent values and one that excludes only divergent values. The two radius values are $r^{\mathrm{s}} = 0.81 \cdot 10^{-3}$, the convergent sphere, and $r^{\mathrm{u}} = 0.83 \cdot 10^{-3}$, the sphere that excludes only divergent points. So by applying the following implications most impacts can already be labeled:

1. $|\boldsymbol{H}_i| \leq \boldsymbol{H}_i^{\ell_o} \wedge \|\boldsymbol{H}_i\|_2 \leq r^{\mathrm{s}} \implies$ no outgoing laser loss
2. $\exists\, j \in \{1, 2, 3\} \,:\, |H_{i_j}| > H_{i_j}^{\ell_o} \vee \|\boldsymbol{H}_i\|_2 > r^{\mathrm{u}} \implies$ outgoing laser loss

A total of 16 impacts are not covered by these rules and require a complete simulation.

5.2.5 Boundary Visualization

An attempt has been made to visualize in an approximate way the convergence boundary on the momentum transferred by meteoroids, by also taking into account the impact point.

In this framework a meteoroid is represented by a particle, therefore it has no angular momentum associated with it. In general, it will only have a linear momentum due to its mass and velocity properties. When it impacts the SC on a certain location, depending on the distance of this location from the Spacecraft's center of mass and depending on the impact angle, it will transfer a different angular momentum vector.

In order to visualize the limits on the linear momentum of the meteoroid particle, for each impact point, two thresholds must be considered simultaneously: the first is the threshold on the linear momentum, that affects the TM's position convergence property; the second is the threshold on the angular momentum, that affects the SC's and TM's attitude convergence properties. The goal is to assign to each impact point in the plot a single scalar value, that represents the the maximum euclidean norm of linear momentum, that the system can withstand in that point, while remaining convergent under the control of the DFAC System.

Unfortunately, there are too many variables that cannot be shown in a single 4D plot. To restrain the visualization to a 4D plot (3D spacial + 1 color) an approximate conservative bound on the maximum linear momentum norm is considered.

The first step in the procedure is to apply a group of linear momentum transfers to each impact point contained in the dataset. These vectors will have the maximum norm possible for TM's position convergence, reported in Equation 5.2, but will be orientated in different directions. In order to eliminate the problem of the impact angle, the "star" of momenta lies on a plane perpendicular to the impact point vector $\boldsymbol{r}_i$ and the different vectors that compose it are evenly spread around a 360° angle, as shown in Fig. 5.6. The orthogonality to $\boldsymbol{r}_i$ allows to consider a worst–case impact angle, that is, an impact angle that will maximize the angular momentum generated, related to the linear momentum by the following relationship:

$$\boldsymbol{H}_i = \boldsymbol{r}_i \times \boldsymbol{p}_i \implies \|\boldsymbol{H}_i\|_2 = \|\boldsymbol{r}_i\|_2 \, \|\boldsymbol{p}_i\|_2 \sin(\theta_{rp})$$

This will also take into account impact directions that would never happen in reality, because for each impact point there could be some directions that are impossible. Nonetheless, by still considering them, the estimate is only more conservative, an acceptable approximation for the goal of visualization.

The second and last step of the procedure is to compute the $\boldsymbol{H}_i$ corresponding to each linear momentum applied to that impact location and check whether it exceeds or not the convergence boundary $\boldsymbol{H}_i^*$ for SC attitude convergence, defined in Equation 5.1. If none of the angular momenta exceeds the $\boldsymbol{H}_i^*$ threshold, then the scalar associated with the impact point $\boldsymbol{r}_i$ is just $\|\boldsymbol{p}_i^*\|_2$. If there is at least one of the angular momenta that exceeds the $\boldsymbol{H}_i^*$ threshold, then the scalar associated with impact point $\boldsymbol{r}_i$ is the maximum euclidean norm among the angular momenta that exceed the convergence threshold, divided by the norm of $\boldsymbol{r}_i$.

At the end of the procedure for each location $\boldsymbol{r}_i$ there will be an associated scalar value, representing a conservative worst–case estimate of the maximum norm of linear momentum, that the system can withstand, while remaining convergent.

The resulting plot can be seen in Figure 5.7. The darker the color, the less linear momentum is required to make the system divergent.

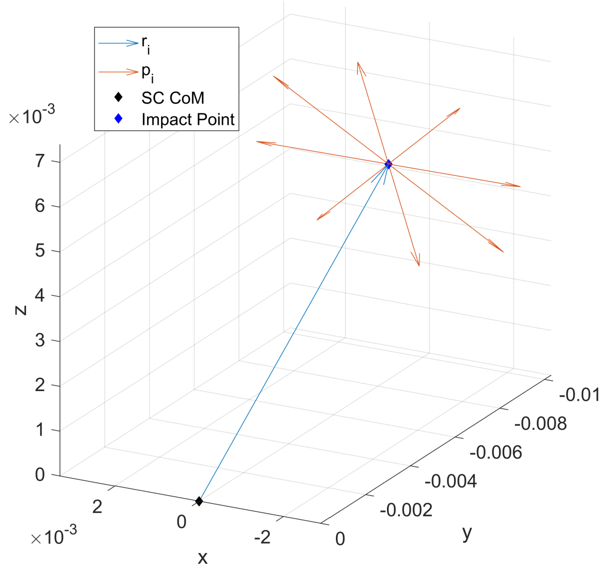

Figure 5.6: “Star” of linear momentum impulses

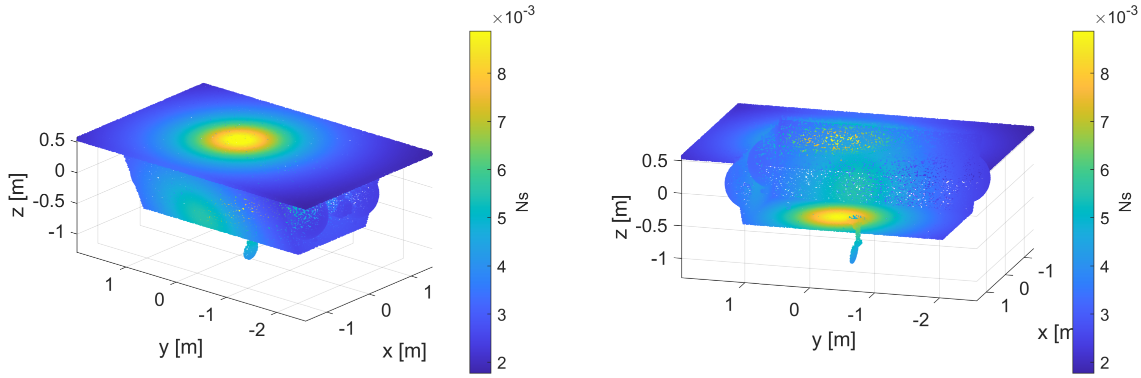

Figure 5.7: Convergence boundary visualization

The plot shows visually that the Spacecraft is more resistant to higher linear momentum transfers around the center of the top solar panel and around the center of the bottom surface; whereas, the borders of the panel and, to a certain extent, also the bottom high–gain antenna are critical regions that can withstand only much smaller impacts.

5.3 LISA States

This Section gives a more detailed explanation regarding all the states that the LISA system can be found in, after an impact.

In order to define all the LISA states, the following system properties have to be considered:

- P1 *Spacecraft attitude convergence*, with values convergent/divergent;
- P2 *Test Mass attitude convergence*, with values convergent/divergent;

- P3 *Test Mass position convergence*, with values convergent/divergent;
- P4 *incoming laser link loss* (DWS sensor), with values loss/no loss;
- P5 *outgoing laser link loss* (DWS sensor), with values loss/no loss.

Table 5.2 lists all the states that the system can attain, among the 32 possible combinations of properties P1–5.

State ID	P1	P2	P3	P4	P5
S0	convergent	convergent	convergent	no loss	no loss
S1	convergent	convergent	convergent	no loss	loss
S2	convergent	convergent	convergent	loss	no loss
S3	convergent	convergent	convergent	loss	loss
S4	convergent	convergent	divergent	loss	loss
S5	divergent	divergent	divergent	loss	loss

Table 5.2: LISA States

The S2 state corresponds to a scenario where another Spacecraft is hit by a meteoroid, say SC2, and starts rotating, breaking at some point the laser link. In this case, it is possible for SC1 to lose the incoming laser link (the one coming from SC2), without necessarily losing the outgoing one (SC2 could still receive the laser from SC1).

Another important remark is that for the DFAC System, as implemented at the beginning of this thesis, all the states different from S0 will cause some sort of issue: in states S1–3, the SC attitude controller cannot use anymore the high–accuracy DWS sensor, that is based on laser links; in states S4 and S5, in addition to the loss of the DWS, the controller itself has to be replaced by a recovery system.

From the list of states one can derive all the possible recovery tasks that are needed in order to cover every possible scenario:

- R1 *Spacecraft attitude recovery*, to be executed in state S5;
- R2 *Test Mass position recovery*, to be executed in states S4 and S5;
- R3 *incoming laser loss recovery*, to be executed in states S3, S4 and S5;
- R4 *waiting mode*, to be executed in state S2.

State S1 does not require any specific recovery task, because in that case the impact is very light and the DFACS system, with the DWS sensors already enabled and working, is enough to return to state S0. In this scenario, at least one of the other two Spacecrafts will transition to state S2, requiring a waiting mode to be activated on that SC.

6 | State Observers

In Chapter 7 extensive use of state observers has been made, due to the fact that LISA is only equipped with sensors that can measure angular and linear positions, but not velocities and accelerations. In this Chapter two state observers or differentiators are considered and evaluated.

6.1 Filtered Differentiator

This type of differentiator is a discrete time linear system, defined by the following Z transform transfer function:

$$F(z) = \frac{N\,(z-1)}{z-1+N\,\tau}$$

The τ parameter is simply the time interval of the filter. The N parameter determines the speed of convergence to the numerical derivative. The filter has a pole at $1 - N\,\tau$, therefore, the closer N is to the filter frequency $1/\tau$, the faster the response to changes in the input.

In the architecture proposed here, this filter is used to estimate the angular error velocity of the SC attitude $\boldsymbol{\omega}_{\mathrm{SC}}$ from $\mathfrak{q}_{\mathrm{SC}}$, measured by the SC–SC DWS and CAS sensors. The main equations are

$$\hat{\dot{\mathfrak{q}}}_{\mathrm{SC}}[k] = N\,(\mathfrak{q}_{\mathrm{SC}}[k] - \mathfrak{q}_{\mathrm{SC}}[k-1]) + (1 - N\,\tau)\,\hat{\dot{\mathfrak{q}}}_{\mathrm{SC}}[k-1] \tag{6.1}$$

$$\hat{\boldsymbol{\omega}}_{\mathrm{SC}} = 2\,\mathfrak{q}^*_{\mathrm{SC}} \otimes \hat{\dot{\mathfrak{q}}}_{\mathrm{SC}} \tag{6.2}$$

where $\hat{\dot{\mathfrak{q}}}_{\mathrm{SC}}$ is the estimated error quaternion derivative and $\hat{\boldsymbol{\omega}}_{\mathrm{SC}}$ is the estimated angular error velocity. Equation 6.2 is the inverse quaternion kinematics relation. Figure 6.1 shows the estimation performance during a recovery maneuver. The filter has been tuned on the 89 impacts that cause SC attitude instability.

Furthermore, this filter is used also to estimate the velocities of the two Test Masses $\boldsymbol{v}_{\mathrm{m}_1}$ and $\boldsymbol{v}_{\mathrm{m}_2}$. The filter takes as input the positions, as measured by the SC–TM DWS, the interferometer and the GRS (more details in Section 7.2), and outputs the estimates $\hat{\boldsymbol{v}}_{\mathrm{m}_1}$ and $\hat{\boldsymbol{v}}_{\mathrm{m}_2}$, according to the following equation:

$$\hat{\boldsymbol{v}}_{\mathrm{m}_j}[k] = N\,(\boldsymbol{r}_{\mathrm{m}_j}[k] - \boldsymbol{r}_{\mathrm{m}_j}[k-1]) + (1 - N\,\tau)\,\hat{\boldsymbol{v}}_{\mathrm{m}_j}[k-1],\ j = 1, 2 \tag{6.3}$$

Figure 6.1 shows the estimation performance during a recovery maneuver. The filter has been tuned on the 96 impacts that cause TM position instability.

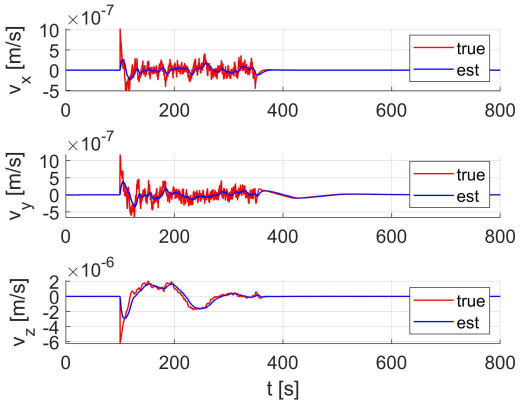

(a) $\boldsymbol{v}_{\mathrm{m}_1}$ estimation

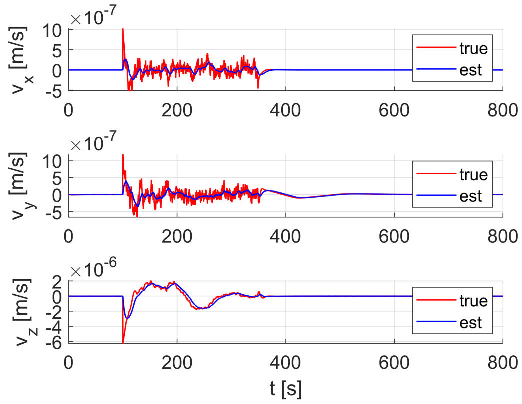

(b) $\boldsymbol{v}_{\mathrm{m}_2}$ estimation

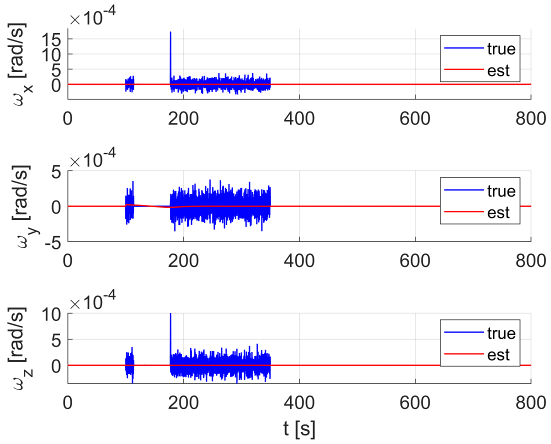

(c) $\boldsymbol{\omega}_{\mathrm{SC}}$ estimation

Figure 6.1: Filtered Differentiator estimation

6.2 Extended Kalman Filter

The EKF is a particular type of discrete–time filter that works by iterating basically two steps: first, there is a prediction made by applying an internal linear model of the process; then, the measurement is used to update the internal states of the filter, by weighting them according to the covariance of the measurement process.

In general, the filter will have an internal linear model in state space form:

$$\begin{aligned} \dot{\boldsymbol{x}} &= A(\boldsymbol{x})\,\boldsymbol{x} + B\,\boldsymbol{u} + B\,\boldsymbol{d}^u \\ \boldsymbol{y} &= C\,\boldsymbol{x} + \boldsymbol{d}^y \end{aligned}$$

that can be discretized with the forward Euler method, leading to

$$\begin{aligned} \boldsymbol{x}_{k+1} &= F_k\,\boldsymbol{x}_k + G\,\boldsymbol{u}_k + \boldsymbol{d}_k \\ \boldsymbol{y}_k &= C\,\boldsymbol{x}_k + \boldsymbol{d}_k^y \end{aligned}$$

where

$$\begin{aligned} F_k &= I + \tau\,A(\boldsymbol{x}_k) \\ G &= \tau\,B \\ \boldsymbol{d}_k &= \tau\,B\,\boldsymbol{d}_k^u \end{aligned}$$

The filter will take as inputs $\boldsymbol{u}_k$, the same input that is given to the real system, and $\boldsymbol{y}_k$, the measured output, and will provide an estimate of the system's real state $\boldsymbol{x}_k$. In this application the EKF's time interval is $\tau = 0.01\,\mathrm{s}$.

Specifically, the detailed algorithm is implemented in the following way:

1. *Prediction* step: an internally predicted state $\boldsymbol{x}_k^p$ and the predicted covariance matrix P_k of the estimation error are computed at time step k:

$$\begin{aligned} \boldsymbol{x}_k^p &= F_k\,\hat{\boldsymbol{x}}_{k-1} + G\,\boldsymbol{u}_{k-1} \\ P_k^p &= F_{k-1}\,P_{k-1}\,F_{k-1}^\top + Q^d \end{aligned}$$

2. *Update* step: using also the measurement $\boldsymbol{y}_k$ coming from the sensor, the internal state of the filter ($\hat{\boldsymbol{x}}$ and P) is updated by the following rules:

$$\begin{aligned} S_k &= C\,P_k^p\,C^\top + R^d \\ K_k &= P_k^p\,C^\top\,S_k^{-1} \\ \Delta\boldsymbol{y}_k &= \boldsymbol{y}_k - C\,\boldsymbol{x}_k^p \\ \hat{\boldsymbol{x}}_k &= \boldsymbol{x}_k^p + K_k\,\Delta\boldsymbol{y}_k \\ P_k &= (I - K_k\,C)\,P_k^p \end{aligned}$$

where Q^d and R^d are matrices that can be tuned, representing respectively the covariance of the input disturbance $\boldsymbol{d}_k$ and the covariance of the measurement process $\boldsymbol{d}_k^y$.

This filter is used to filter out the noise from the SC inertial attitude quaternion $\mathfrak{q}_{\mathrm{SI}}$, measured by the Star Tracker, and to estimate the SC angular velocity $\boldsymbol{\omega}_{\mathrm{SI}}$. The EKF filter provides an estimate of the SC's attitude state $\boldsymbol{x} = \begin{bmatrix} \mathfrak{q}_{\mathrm{SI}} \\ \boldsymbol{\omega}_{\mathrm{SI}} \end{bmatrix}$.

The internal model in state space form is

$$A(\boldsymbol{x}) = \begin{bmatrix} 0 & \frac{1}{2}\,Q_{\mathrm{SI}} \\ 0 & -J_{\mathrm{S}}^{-1}\,[\boldsymbol{\omega}_{\mathrm{SI}}\times]\,J_{\mathrm{S}} \end{bmatrix} \in \mathbb{R}^{7,7} \tag{6.4}$$

$$Q_{\mathrm{SI}} = \begin{bmatrix} -q_{\mathrm{SI}_1} & -q_{\mathrm{SI}_2} & -q_{\mathrm{SI}_3} \\ q_{\mathrm{SI}_0} & -q_{\mathrm{SI}_3} & q_{\mathrm{SI}_2} \\ q_{\mathrm{SI}_3} & q_{\mathrm{SI}_0} & -q_{\mathrm{SI}_1} \\ -q_{\mathrm{SI}_2} & q_{\mathrm{SI}_1} & q_{\mathrm{SI}_0} \end{bmatrix} \tag{6.5}$$

$$B = \begin{bmatrix} 0 \\ \mathrm{J}_{\mathrm{S}}^{-1} \end{bmatrix} \in \mathbb{R}^{7,3} \tag{6.6}$$

$$C = \begin{bmatrix} I & 0 \end{bmatrix} \in \mathbb{R}^{4,7} \tag{6.7}$$

The input $\boldsymbol{u}$ is the torque generated by the MPS system, that can be obtained from the torque command $\boldsymbol{M}_{\mathrm{T}}$ of the attitude controller. The output $\boldsymbol{y}$ is the inertial Spacecraft quaternion $\mathfrak{q}_{\mathrm{SI}}$ measured by the Star Tracker.

The tuning process for this state observer starts by defining the structures of matrices Q^d and R^d, making the same considerations of [3]: Q^d will be a 7x7 diagonal matrix where only the last three diagonal entries are different from zero, because the model disturbance enters just in the angular acceleration equations, not in the quaternion kinematics; R^d will be a 3x3 diagonal matrix where the third diagonal entry is 100 times greater than the other two, because the star tracker has a noise on the z axis that is 10 times greater with respect to the other axis. Therefore the tuning procedure can focus only on varying two real parameters α and β, that will in turn give the EKF matrices according to the following relationship:

$$Q^d = \alpha\, \mathtt{diag}(0,0,0,0,1,1,1) \tag{6.8}$$

$$R^d = \beta \begin{bmatrix} 1 & 0 & 0 \\ 0 & 1 & 0 \\ 0 & 0 & 100 \end{bmatrix} \tag{6.9}$$

This process can then be further simplified by considering that only the ration between α and β matters, not the individual values. Thus, a scalar α/β represents the single variable of the tuning process.

Figure 6.2 shows the estimation performance during a recovery maneuver. The filter has been tuned on the 89 impacts that cause SC attitude instability.

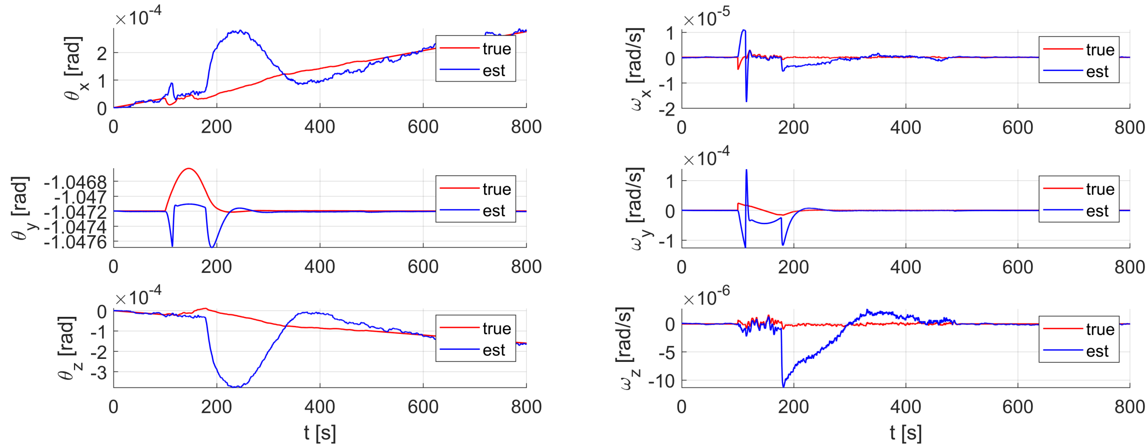

(a) $\mathfrak{q}_{\mathrm{SI}}$ estimation (b) $\boldsymbol{\omega}_{\mathrm{SI}}$ estimation

Figure 6.2: EKF estimation

7 | Recovery Control System

The goal of this Thesis is to design and test a recovery system for the LISA mission. Different configurations of controllers and sensors have been tested, summarized in Table 7.1. In this Chapter only the two most effective recovery systems are presented: the main one is the Configuration 1, that assumes the presence of a CAS sensor to aid the recovery maneuver and is based on PD/PID controllers; the other one is Configuration 2, that allows the CAS sensor to be removed, requiring a model of the solar pressure, and is based on PD/PID controllers too.

ID	SC Att. control	TM Pos. control	CAS	State Obs.
1	PD	PID	yes	EKF
2	PD	PID	no	EKF+Solar Press. model
3	PD	PID	yes	Filtered Diff.
4	Sliding Mode	PID	yes	EKF

Table 7.1: Summary of tested configurations

The main problems that had to be solved in its implementation are

1. *impact detection*, that is to detect when an impact occurs and to predict with the highest accuracy possible in what state does the LISA system transition into;
2. *sensor management*, that is to switch the sensors in the correct operating modes and implement some fusion in order to obtain the most precise measurement available for each signal;
3. *controller design*, that is to design some controllers to be evaluated that can fulfil the recovery tasks determined in Section 5.3;
4. *end of recovery* (EoR) *detection*, that is to detect when the LISA system has been successfully recovered and is ready to switch back to science mode.

For each of these problems a section is dedicated to it, that explains the implemented solution.

7.1 Meteoroid Impact Detection

Impact detection is the task of detecting when an impact has occurred and, more specifically, in which state the LISA system has transitioned into. The detection happens through a monitoring system that tracks and processes a group of signals online and is able to notice when one of the properties P1–5 of the LISA system (defined in Section

5.3) has changed; according to these properties it is able to output the new state of the system and consequently start the appropriate recovery tasks.

The more physical states of the LISA system it has available, the better the monitoring system performance. Unfortunately, the Spacecraft is equipped only with sensors that can measure linear or angular positions, but not velocities or accelerations. This highly constraints the performance that can be expected. The detected state will often be based on some estimated signals, thus the predicted state could sometimes not correspond to the real one. For this reason there is a safety property that has to be enforced on the detection system, that is, when the detection is wrong, it should always predict a state that is "worse" than the real one. A LISA state is considered worse than another, when it requires the activation of more recovery tasks.

The principles followed here are those of separation of concerns and modularity. For each of the five LISA properties there is a separate monitoring system that estimates the value of that property.

Here different monitoring systems are presented for comparison. Specifically, one monitoring system for each order of signal derivatives considered in the detection process:

- *Zero–order monitoring*, where only the position signals are used;
- *First–order monitoring*, where estimated velocity signals are added.

A *Second–order monitoring* is not presented due to the extremely low acceleration estimation performances.

It is not obvious a priori which system can perform better: in theory, by increasing the number of signals and the derivatives order, the detection system has more information available and should perform better; in practice, those signals will be estimated, not directly measured, thus they will be affected by a higher noise, that could interfere with the detection process.

7.1.1 P1-2 Spacecraft and TM attitude convergence

The P1 property *Spacecraft attitude convergence* can have two values: convergent or divergent. In order to detect which is the value of the property, a basic threshold–based system is implemented.

First, a zero–order approach is tested, where only the error quaternion $\mathfrak{q}_{\text{SC}}$, measured from the DWS sensor during Science phase, is used in the monitoring process. The basic idea is to have a maximum rotation angle θ^*_{SC}, that constitutes the threshold between the two values of the P1 property. The absolute rotation angle θ_{SC} can be obtained from $\mathfrak{q}_{\text{SC}}$ by the following relationship:

$$\theta_{\text{SC}} = 2\,\cos^{-1}(\mathfrak{q}_{\text{SC}_0})$$

So, if $\theta_{\text{SC}} > \theta^*_{\text{SC}}$, then P1 is divergent, else it is convergent.

In order to tune the threshold θ^*_{SC} and to evaluate the performance of the monitoring system, the impact dataset is divided into two separate groups based on the SC Attitude divergence label. Only a total of 89 impacts will make the SC attitude go divergent, so among the convergent impacts only the strongest 89 impacts are considered. By eliminating the rest of them, the complexity and time required to do the tests is reduced.

The safety rule implies that the false negatives should be zero. False negatives are strong impacts that cause the SC attitude to become divergent, but are wrongly detected as P1 convergent by the monitoring system. On the other hand, false positives are lighter impacts that keep the SC attitude convergent with the DFACS controller, but are wrongly classified as P1 divergent by the monitoring system. Therefore, the optimization objective is to have minimum average detection time and minimum false positives, by keeping the false negatives to zero.

Figure 7.1 shows the simulation results.

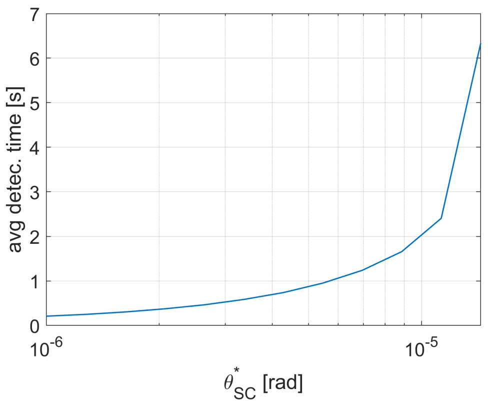

(a) Average Detection Time

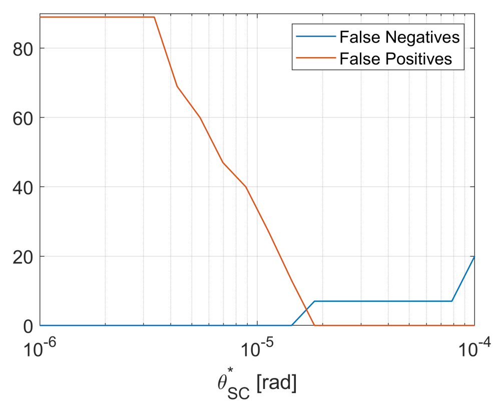

(b) False Positives and False Negatives

Figure 7.1: Simulation results for P1 zero–order monitoring

Figure 7.1a contains the relationship between the threshold θ^*_{SC} and the average *detection time*, that is the average across all the tested impacts of the time elapsed between the impact instant and the instant when the monitoring system outputs its prediction. From this plot it can be seen that, generally speaking, the lower the threshold the more sensitive the system is to rotations and the faster it outputs a new detection.

Figure 7.1b contains the relationship between the threshold θ^*_{SC} and the false positives and false negatives. This plot shows that the lower the threshold, the more false positives there are.

From these plots the optimal value $\theta^*_{\mathrm{SC}} \approx 1.43 \cdot 10^{-5}$ rad can be inferred. The number of false positives is 13 and the average detection time is 6.337 s.

Next the first–order detection system is tested with the same performance parameters. Another threshold ω^*_{SC} is defined for the $\boldsymbol{\omega}_{\mathrm{SC}}$ signal. This derivative is estimated by a Filtered Differentiator with $N = 4$, presented in Section 6.1, that differentiates the DWS measured quaternion $\mathfrak{q}_{\mathrm{SC}}$ and applies inverted quaternion kinematics. The estimated signal is $\hat{\boldsymbol{\omega}}_{\mathrm{SC}}$. Therefore the detection rule becomes:

$$\|\hat{\boldsymbol{\omega}}_{\mathrm{SC}}\|_2 > \omega^*_{\mathrm{SC}} \implies \text{P1 divergent}$$

Figure 7.2 shows the results of the simulations.

Figure 7.2a shows the average detection time for the values of the threshold with no false negatives.

The optimal value for this threshold is $\omega^*_{\mathrm{SC}} \approx 3.36 \cdot 10^{-6}$ rad/s. The number of false positives is 34 and the average detection time is 1.02 s. The outcome is that by using just the estimated $\boldsymbol{\omega}_{\mathrm{SC}}$, the detection becomes faster at the cost of more false positives.

The P2 property TM attitude convergence is equivalent to the value of P1, so the monitoring system is one for both properties.

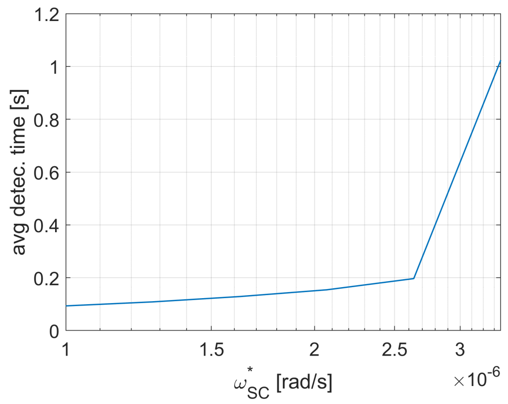

(a) Average Detection Time

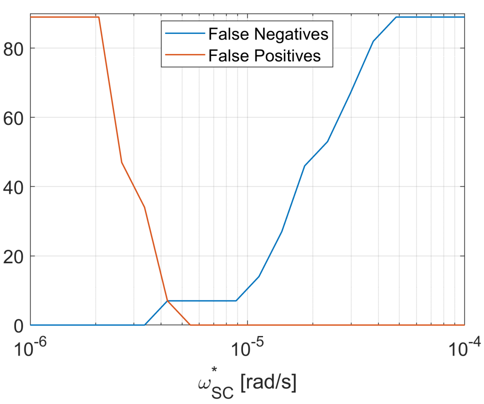

(b) False Positives and False Negatives

Figure 7.2: Simulation results for P1 first–order monitoring

7.1.2 P3 Test Mass position convergence

The P3 property *Test Mass position convergence* can have two values: convergent or divergent. In order to detect the value of the property, a basic threshold–based system is implemented.

First, a zero-–order approach is tested, where only the $\boldsymbol{r}_{\mathrm{m}_j}$ signals are considered. In this case the filtered versions $\hat{\boldsymbol{r}}_{\mathrm{m}_j}$ from the EKF, presented in Section 6.2, are employed. A new threshold r^*_{m} is defined and the detection rule becomes

$$\|\boldsymbol{r}_{\mathrm{m}_1}\|_2 > r^*_{\mathrm{m}} \vee \|\boldsymbol{r}_{\mathrm{m}_2}\|_2 > r^*_{\mathrm{m}} \implies \text{P3 divergent}$$

In order to tune the threshold θ^*_{SC} and to evaluate the performance of the monitoring system, the impact dataset is divided into two separate groups based on the TM Position divergence label. A total of 96 impacts will make the TM Position go divergent, so among the convergent impacts only the strongest 96 impacts are considered. By eliminating the rest of them, the complexity and time required to do the tests is reduced.

The same evaluation parameters of the P1 monitoring are computed during tests: average detection time, number of false positives and number of false negatives. Again, according to the safety property the number of false negatives should be zero.

The results for the first tests are shown in Figure 7.3.

From Figure 7.3b it can be seen that the optimal value for the threshold is $r^*_{\mathrm{m}} \approx 5.45 \cdot 10^{-6}\,\mathrm{m}$. With this choice of threshold the number of false positives is 14 and the average detection time is 3.74 s.

The next test concerns the first–order monitoring system. The new threshold v^*_{m} is defined for the following detection rule:

$$\|\boldsymbol{v}_{\mathrm{m}_1}\|_2 > v^*_{\mathrm{m}} \vee \|\boldsymbol{v}_{\mathrm{m}_2}\|_2 > v^*_{\mathrm{m}} \implies \text{P3 divergent}$$

The test results are shown in Figure 7.4.

The optimal value is $v^*_{\mathrm{m}} \approx 1.62 \cdot 10^{-6}\,\mathrm{m/s}$, with an average detection time of 10.64 s and 14 false positives.

In this case, the zero–order monitoring is faster with the same number of false positives.

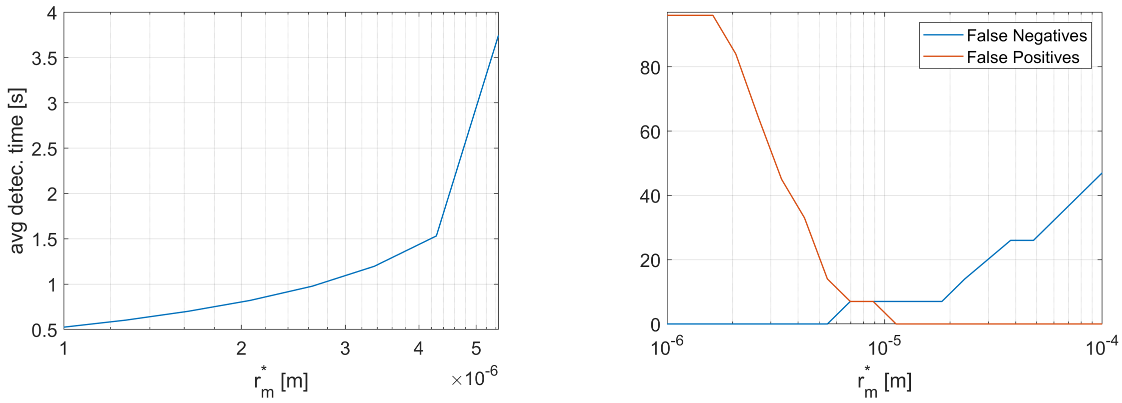

(a) Average detection time (b) False Positives and False Negatives

Figure 7.3: Simulation results for P3 zero–order monitoring

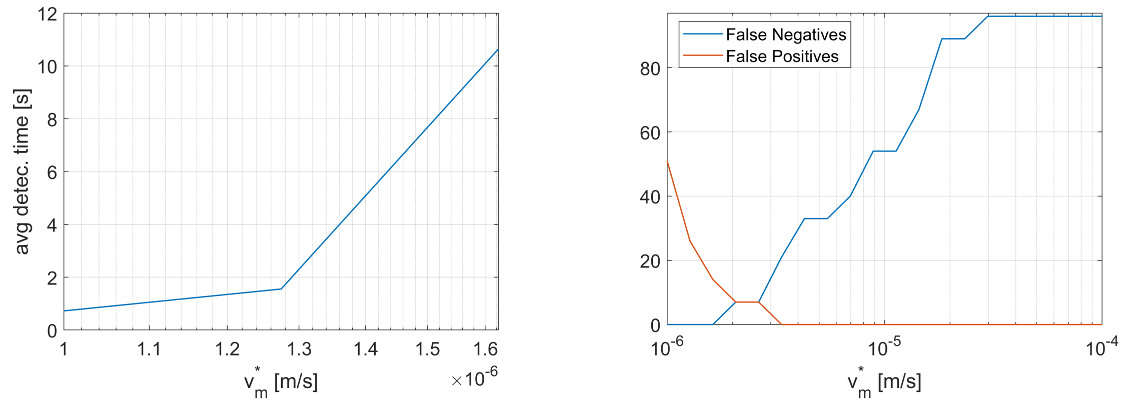

(a) Average detection time (b) False Positives and False Negatives

Figure 7.4: Simulation results for P3 first–order monitoring

7.1.3 P4 and P5 Laser Loss

The P4 incoming laser loss and the P5 outgoing laser loss properties are monitored in hardware. This work makes the reasonable assumption that the laser sensors can detect whether the laser is hitting the sensor or not and update an internal flag accordingly, that can be accessed by the controller.

For this reason the detection time will always be very small, in this work assumed to be 10 ms, depending on the performance of the processor of the on–board computer and the real time operating system. The number of false positives and false negatives will be zero, given that the presence and absence of laser is a perfectly detectable fact.

7.2 Sensor Management

The task of sensor managing consists of two important parts: the first, is to correctly switch each sensor to the appropriate operating mode, during recovery; the second, is to handle the different sensor measurements in order to output for each signal the most accurate value at each time.

As regards the first problem, only the GRS sensors are affected. Indeed, they have to be switched to Wide Range mode in order to increase their actuation authority on the TMs. This will also cause an increase in the measurement noise, as reported in Table 2.5.

As regards the second problem, the following remarks are important:

1. the pitch and yaw angles of the TMs are measured both by the GRS and by the local SC–TM DWS sensor, when available;
2. the x coordinate of the TM position $\boldsymbol{r}_{\mathrm{m}_j}$ is measured both by the GRS and by the local Interferometer, when available;
3. there could be attitudes for which both the SC–SC DWS and the CAS sensors are active at the same time.

In order to deal with the remarks 1 and 2, the controller will perform a measurement fusion for both the attitude $\boldsymbol{\theta}_{\mathrm{m}_j}$ and position $\boldsymbol{r}_{\mathrm{m}_j}$ of the TMs, that is, when available the measurement from the laser sensors will replace the corresponding components of the signals that come from the GRS, making it more accurate. When an impact that activates the recovery task R2 takes place, that is the recovery of the TM position, the fusion will be turned off, leaving just the GRS sensor to provide all the measurements. When the recovery is concluded the fusion will be activated again.

To deal with remark 3, the controller will simply use the most accurate of the measurements available for the $\mathfrak{q}_{\mathrm{SC}}$ signal. When both the DWS and CAS are available, the CAS measurement is discarded. Whereas, when the DWS is lost the CAS provides its measurement instead. Finally, when also the CAS sensor is lost the $\mathfrak{q}_{\mathrm{SC}}$ signal will be reconstructed internally by the controller using the computation $\mathfrak{q}_{\mathrm{SC}} = \hat{\mathfrak{q}}_{\mathrm{CI}}^* \otimes \hat{\mathfrak{q}}_{\mathrm{SI}}$, where $\hat{\mathfrak{q}}_{\mathrm{CI}}$ is an estimate of the desired inertial attitude computed on–board during recovery and $\hat{\mathfrak{q}}_{\mathrm{SI}}$ is the EKF filtered version of the Spacecraft inertial attitude measured by the Star Tracker.

The $\hat{\mathfrak{q}}_{\mathrm{CI}}$ quaternion is computed by integration of the following expression:

$$\dot{\hat{\mathfrak{q}}}_{\mathrm{CI}} = \frac{1}{2}\,\hat{\mathfrak{q}}_{\mathrm{CI}} \otimes \begin{bmatrix} 0 \\ \hat{\boldsymbol{\omega}}_{\mathrm{SC}} \end{bmatrix}$$

where $\hat{\boldsymbol{\omega}}_{\mathrm{SC}}$ is the approximate time dependent function reported in Equation 3.5, obtained by orbital simulations. The accuracy and performance of the recovery system depends on how accurate this orbital simulations are. Future work could focus on ways to estimate this orbital properties directly online, before the impact happens, in order to have a more accurate estimate of the nominal desired attitude, that does not rely entirely on offline simulations. This last switching system for the quantity $\mathfrak{q}_{\mathrm{SC}}$ represents the implementation of the recovery task R3, that handles the incoming laser loss scenario.

Table 7.2 summarizes the different scenarios and what changes will be made to each sensor.

7.3 Controller Design

The controllers needed for the recovery system are two: one for the SC attitude recovery (task R1) and the other for the TM position recovery (task R2).

State ID	SC–SC DWS	CAS	GRS	TM–SC DWS+IFO	Star Tracker
S0	active	active	active HR	active	not used
S1	active	active	active HR	active	not used
S2	not used	not used	active HR	active	active
S3	not used	not used	active HR	active	active
S4	not used	not used	active WR	not used	active
S5	not used	not used	active WR	not used	active

Table 7.2: Sensor management summary

7.3.1 Spacecraft attitude controller

The main controller design procedure starts from the design of a Sliding Mode controller, that already showed to be effective in the Constellation Acquisition phase [3].

First step is to design a sliding variable $\boldsymbol{s}$ as a function of the desired state variable, such that

1. when $\boldsymbol{s} = 0$, the tracking error tends to 0;
2. $\dot{\boldsymbol{s}}$ is affected by the input command $\boldsymbol{u}$.

A possible choice of such variable is $\boldsymbol{s} = \tilde{\boldsymbol{\omega}} + \lambda\,\tilde{\boldsymbol{q}}$, where λ is a positive real coefficient, $\tilde{\boldsymbol{q}}$ is the vector part of the error quaternion of the Spacecraft attitude during recovery and $\tilde{\boldsymbol{\omega}}$ is the error angular velocity; more specifically, $\tilde{\mathfrak{q}} = \mathfrak{q}^*_{\mathrm{CI}} \otimes \mathfrak{q}_{\mathrm{SI}}$ and $\tilde{\boldsymbol{\omega}} = \boldsymbol{\omega}_{\mathrm{SI}} - \boldsymbol{\omega}_{\mathrm{CI}}$. With this choice both the requirements on $\boldsymbol{s}$ are fulfilled:

1. $\boldsymbol{s} = 0 \implies \tilde{\boldsymbol{\omega}} + \lambda\,\tilde{\boldsymbol{q}} = 0 \iff \tilde{\boldsymbol{\omega}} = -\lambda\,\tilde{\boldsymbol{q}}$, that means that the dynamics of the error is an exponential function that tends to zero, approximately with rate λ;
2. $\dot{\boldsymbol{s}} = \dot{\tilde{\boldsymbol{\omega}}} + \lambda\,\dot{\tilde{\boldsymbol{q}}} = \dot{\boldsymbol{\omega}}_{\mathrm{SI}} - \dot{\boldsymbol{\omega}}_{\mathrm{CI}} + \lambda\,\dot{\tilde{\boldsymbol{q}}}$ and the term $\dot{\boldsymbol{\omega}}_{\mathrm{SI}}$ depends on the command input $\boldsymbol{u} = \boldsymbol{M}_{\mathrm{T}}$ (the torque from the MPS), according to Equation 3.9.

More specifically the derivative of the sliding variable can be expanded with the dynamics of the SC attitude (no superscript means represented in the SRF):

$$\begin{aligned}
\dot{\boldsymbol{s}} = \dot{\tilde{\boldsymbol{\omega}}} + \lambda\,\dot{\tilde{\boldsymbol{q}}} = \dot{\boldsymbol{\omega}}_{\mathrm{SI}} - \dot{\boldsymbol{\omega}}_{\mathrm{CI}} + \lambda\,\dot{\tilde{\boldsymbol{q}}} &= f(\boldsymbol{\omega}_{\mathrm{SI}}) + \mathrm{J}_{\mathrm{S}}^{-1}\,\boldsymbol{M}_{\mathrm{T}} - \dot{\boldsymbol{\omega}}_{\mathrm{CI}} + \lambda\,\dot{\tilde{\boldsymbol{q}}} \\
f(\boldsymbol{\omega}_{\mathrm{SI}}) = -\mathrm{J}_{\mathrm{S}}^{-1}\,\boldsymbol{\omega}_{\mathrm{SI}} \times (\mathrm{J}_{\mathrm{S}}\,\boldsymbol{\omega}_{\mathrm{SI}}) &+ \mathrm{J}_{\mathrm{S}}^{-1}\left(+\mathbf{D}_{\mathrm{T}} + \mathbf{D}^{\mathrm{S}}_{\odot\mathrm{press}} + \mathbf{M}_{\mathrm{met}}\right) + \\
&- \mathrm{J}_{\mathrm{S}}^{-1} \sum_{j=1,2} \mathrm{T}^{\mathrm{S}}_{\mathrm{o}_j}\,\mathrm{I}_{zz}\,\ddot{\boldsymbol{\xi}}^{\mathrm{o}_j}_j + \mathrm{T}^{\mathrm{S}}_{\mathrm{o}_j}\,\mathbf{M}^{\mathrm{o}_j}_{\mathrm{E}_j} + \boldsymbol{b}_j \times \left(\mathrm{T}^{\mathrm{S}}_{\mathrm{o}_j}\,\mathbf{F}^{\mathrm{o}_j}_{\mathrm{E}_j}\right)
\end{aligned}$$

The nonlinear function f can be seen as composed by two terms: the gyroscopic term and other disturbances due to meteoroid impacts and due to noise in actuators and GRS electrodes. An approximate dynamics function $\hat{f}$ is defined in the following way by neglecting the disturbance terms:

$$\hat{f}(\boldsymbol{\omega}_{\mathrm{SI}}) = -\mathrm{J}_{\mathrm{S}}^{-1}\,\boldsymbol{\omega}_{\mathrm{SI}} \times (\mathrm{J}_{\mathrm{S}}\,\boldsymbol{\omega}_{\mathrm{SI}})$$

The command input $\boldsymbol{M}_{\mathrm{T}}$ can be decomposed in two control laws: a partially linearizing one and the one that ensures finite–time convergence to the sliding manifold $\boldsymbol{s} = 0$, represented with $\bar{\boldsymbol{u}}$. The linearizing command is

$$\boldsymbol{M}_{\mathrm{T}} = \mathrm{J}_{\mathrm{S}}\,(-\hat{f} + \dot{\boldsymbol{\omega}}_{\mathrm{CI}} - \lambda\,\dot{\tilde{\boldsymbol{q}}} + \bar{\boldsymbol{u}})$$

When it is applied to the system the equation of $\dot{\boldsymbol{s}}$ becomes

$$\dot{\boldsymbol{s}} = f - \hat{f} + \bar{\boldsymbol{u}}$$

If $\hat{f}$ is temporarily assumed to be equal to the exact dynamics f, then the problem becomes perfectly diagonal, that is the multi–input system $\dot{\boldsymbol{s}} = \bar{\boldsymbol{u}}$ is composed by the parallel of 3 single–input systems, with dynamics $\dot{s}_i = \bar{u}_i$, $i = 1, 2, 3$.

The sliding variable should go to zero in finite time, thus a common known finite–time convergence law is used [17, p. 62]:

$$\begin{aligned}
\frac{1}{2}\frac{d}{dt}(s_i)^2 &\leq -\eta\,|s_i|, \quad \eta > 0 \\
s_i\,\dot{s}_i &\leq -\eta\,s_i\,\mathtt{sign}(s_i) \\
\dot{s}_i &\leq -\eta\,\mathtt{sign}(s_i) \\
\bar{u}_i &\leq |(f - \hat{f})_i| - \eta\,\mathtt{sign}(s_i)
\end{aligned}$$

From the above inequality regarding $\bar{\boldsymbol{u}}$, it can be seen that, in theory, it should be $\eta > \left\| f - \hat{f} \right\|_\infty$, thus an upper bound on the error in the dynamics due to the neglected terms should be known. In practice, η can also be tuned on simulations.

Finally, the control law obtained is

$$\boldsymbol{M}_\mathrm{T} = \mathrm{J_S}\,\left(\mathrm{J_S^{-1}}\,\boldsymbol{\omega}_\mathrm{SI} \times (\mathrm{J_S}\,\boldsymbol{\omega}_\mathrm{SI}) + \dot{\boldsymbol{\omega}}_\mathrm{CI} - \lambda\,\dot{\tilde{\boldsymbol{q}}} - \eta\,\mathtt{sign}(\boldsymbol{s})\right) \tag{7.1}$$

where

- $\boldsymbol{\omega}_\mathrm{SI}$ is estimated ($\hat{\boldsymbol{\omega}}_\mathrm{SI}$) from the Filtered Differentiator, as shown in Section 6.1;
- $\dot{\boldsymbol{\omega}}_\mathrm{CI}$ is the desired angular acceleration, needed in order to track the constellation, this would also be computed nominally offline from orbital simulations, but it is very small, as seen by simulations, and can be neglected without affecting the recovery task;
- $\tilde{\boldsymbol{q}}$ is directly taken from the SC–SC DWS or CAS sensor, when available; otherwise it is computed as the vector part of $\tilde{\mathfrak{q}}$ computed from the available signals in the following way:

  $$\tilde{\mathfrak{q}} = \hat{\mathfrak{q}}^*_\mathrm{CI} \otimes \hat{\mathfrak{q}}_\mathrm{SI}$$

  where $\hat{\mathfrak{q}}_\mathrm{CI}$ is the nominal, internally computed, desired SC attitude and $\hat{\mathfrak{q}}_\mathrm{SI}$ is the EKF filtered Star Tracker measurement;
- $\dot{\tilde{\boldsymbol{q}}}$ is the vector part of $\dot{\tilde{\mathfrak{q}}}$ computed always online by quaternion kinematics:

  $$\dot{\tilde{\mathfrak{q}}} = \frac{1}{2}\,\tilde{\mathfrak{q}} \otimes \begin{bmatrix} 0 \\ \hat{\boldsymbol{\omega}}_\mathrm{SI} - \hat{\boldsymbol{\omega}}_\mathrm{CI} \end{bmatrix}$$

  where $\hat{\boldsymbol{\omega}}_\mathrm{CI}$ is the desired angular velocity, internally computed according to Equation 3.5.

The sign function is applied component–wise to the sliding variable.

A well performing tuning of this sliding mode controller is $\lambda = 1$ and $\eta = 1$.

A common way to deal with the problem of high command effort and chattering, that usually affects SM controllers, due to the high frequency switching term contained in the control law, is to replace the sign function with another, that approximates its behavior to a certain extent, that can be tuned by means of a scalar parameter ρ. Usually functions like arctan, sigmoid or saturation are employed as substitutes to the sign. Although not strictly equivalent to one another, they serve the same purpose of reducing the switching behavior of the control command. In this design, the saturation function is chosen, that is so defined:

$$\mathtt{sat}(x) = \begin{cases} -1 & x < -1 \\ x & -1 \leq x \leq 1 \\ +1 & x > 1 \end{cases}$$

and has the plot shown in Figure 7.5a.

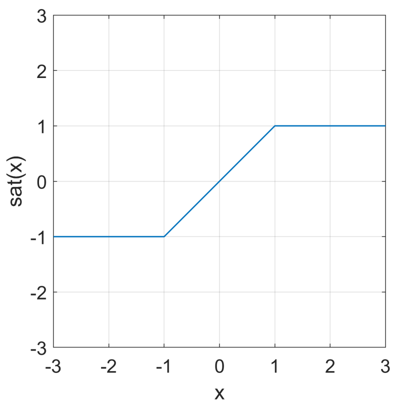

(a) `sat` function

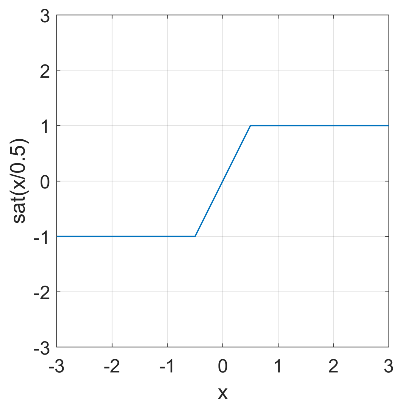

(b) Parametrized `sat` function with $\rho = 0.5$

Figure 7.5: Plot of the `sat` function

It is easy to make it depend on a scalar parameter to increase or diminish its linearizing effect. Specifically, the linearizing effect will only be present in the interval $[-\rho;\, \rho]$, as shown here:

$$\mathtt{sat}(\frac{x}{\rho}) = \begin{cases} -1 & x < -\rho \\ \frac{x}{\rho} & -\rho \leq x \leq \rho \\ +1 & x > \rho \end{cases}$$

and in the plot in Figure 7.5b.

The new control law becomes:

$$\boldsymbol{M}_{\mathrm{T}} = \mathrm{J_S} \left[\mathrm{J_S^{-1}}\, \boldsymbol{\omega}_{\mathrm{SI}} \times (\mathrm{J_S}\, \boldsymbol{\omega}_{\mathrm{SI}}) + \dot{\boldsymbol{\omega}}_{\mathrm{CI}} - \lambda\, \dot{\tilde{\boldsymbol{q}}} - \eta\, \mathtt{sat}\left(\frac{1}{\rho}\, \boldsymbol{s}\right)\right] \tag{7.2}$$

From simulations it was found that even very large values of ρ do not affect particularly the performance of the SC attitude recovery controller, except from reducing the command activity. The following implication holds in this case:

$$\rho \gg |s_i| \implies \mathtt{sat}\left(\frac{s_i}{\rho}\right) \approx \frac{s_i}{\rho} \tag{7.3}$$

Therefore, the control law with the saturation term can be rewritten as

$$\boldsymbol{M}_\mathrm{T} = \mathrm{J_S} \left(\mathrm{J_S^{-1}} \boldsymbol{\omega}_\mathrm{SI} \times (\mathrm{J_S} \boldsymbol{\omega}_\mathrm{SI}) + \dot{\boldsymbol{\omega}}_\mathrm{CI} - \lambda \dot{\tilde{\boldsymbol{q}}} - \frac{\eta}{\rho} \boldsymbol{s} \right)$$
$$\boldsymbol{M}_\mathrm{T} = \boldsymbol{\omega}_\mathrm{SI} \times (\mathrm{J_S} \boldsymbol{\omega}_\mathrm{SI}) + \mathrm{J_S} \dot{\boldsymbol{\omega}}_\mathrm{CI} - \lambda \mathrm{J_S} \dot{\tilde{\boldsymbol{q}}} - \frac{\eta}{\rho} \mathrm{J_S} \tilde{\boldsymbol{\omega}} - \frac{\lambda \eta}{\rho} \mathrm{J_S} \tilde{\boldsymbol{q}}$$

that is basically a PD control law, with a partial feedback linearization given by the gyroscopic term and the inertia tensor.

Furthermore, by applying some transformations, a tuning for the PD control law, that makes the performance equivalent to that of the SM controller, can be obtained:

1. substitution of the parameters with the following values: $\lambda = 1$ and $\eta = 1$, from the previous SM tuning, $\rho = 1$ found from simulations, because the order of magnitude of any s_i is very small, so the linearizing assumption (Equation 7.3) can be applied;
2. neglecting the desired angular acceleration term $\dot{\boldsymbol{\omega}}_\mathrm{CI}$, because it is very small in norm and does not impact appreciably the performance of the SM;
3. the signal $\dot{\tilde{\boldsymbol{q}}}$ is computed by simple quaternion kinematic from $\tilde{\boldsymbol{q}}$ and $\tilde{\boldsymbol{\omega}}$, that are already in the control law, thus it can be removed from the sum;
4. also the gyroscopic term is very small with the rotations that generate from a micro–meteoroid impact, or at least it is very small when compared to the P. D. terms in the control law, therefore it is removed.

These transformations lead to the final PD attitude recovery control law:

$$\boldsymbol{M}_\mathrm{T} = -\mathrm{J_S} \tilde{\boldsymbol{\omega}} - \mathrm{J_S} \tilde{\boldsymbol{q}} \tag{7.4}$$

A problem that could arise from using only the vectorial part $\tilde{\boldsymbol{q}}$ of the attitude error quaternion is the *quaternion unwinding* phenomenon. This problem arises from the fact that quaternions provide a double coverage of the orthogonal 3 by 3 matrix group SO(3), that is used to represent rotations. When using quaternions in a closed feedback PID control configuration, there are usually two equilibrium points $\tilde{\mathfrak{q}} = \begin{bmatrix} 1 & 0 & 0 & 0 \end{bmatrix}^\top$ and $\tilde{\mathfrak{q}} = \begin{bmatrix} -1 & 0 & 0 & 0 \end{bmatrix}^\top$, that are respectively stable and unstable. A common heuristic to prevent this issue is obtained by multiplying the vectorial part by the scalar part, obtaining the following control law:

$$\boldsymbol{M}_\mathrm{T} = -\mathrm{J_S} \tilde{\boldsymbol{\omega}} - \mathrm{J_S} \tilde{\mathfrak{q}}_0 \tilde{\boldsymbol{q}} \tag{7.5}$$

Figure 7.6 shows the result for the simulation of meteoroid with id 1, that is one of the strongest impacts in the dataset, where the impact happens after 100 s.

The general architecture of the Spacecraft attitude recovery controller is shown in Figure 7.7.

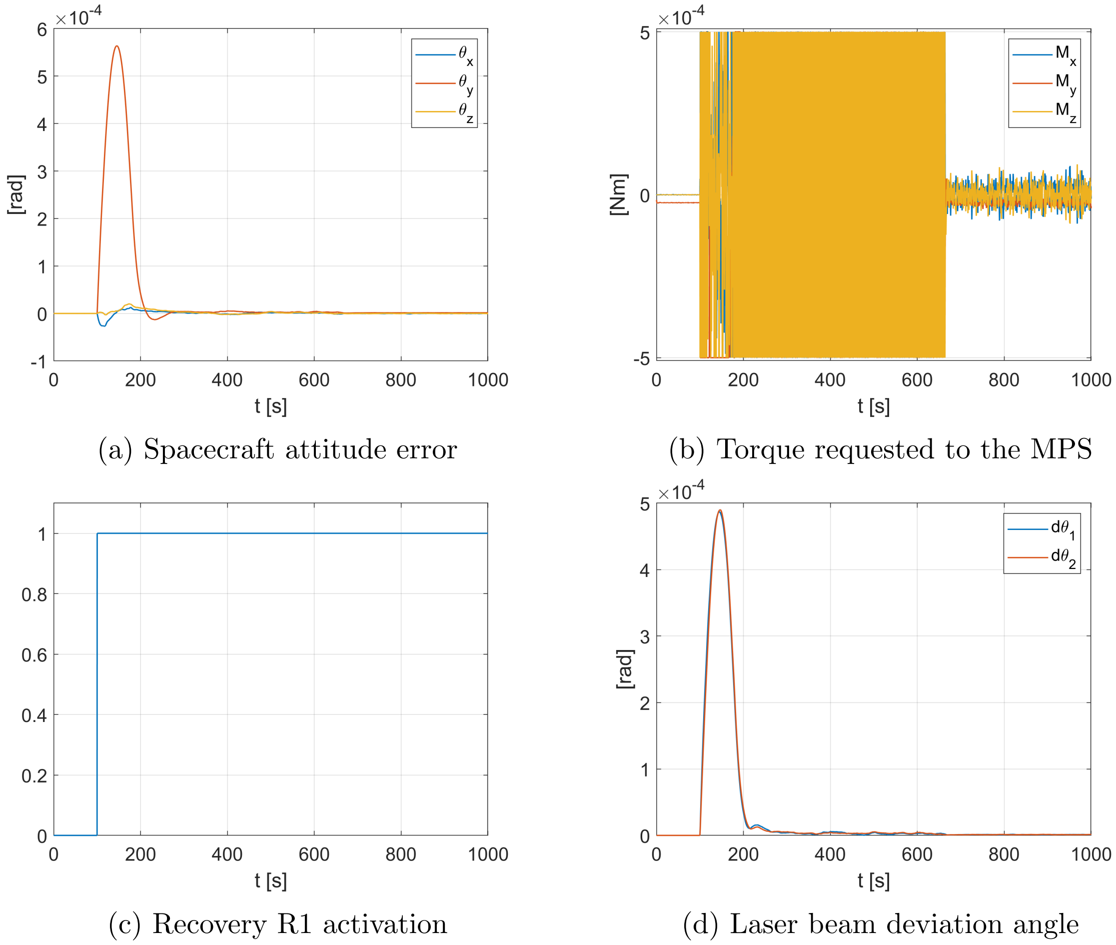

Figure 7.6: Simulation of the SC att. rec. controller

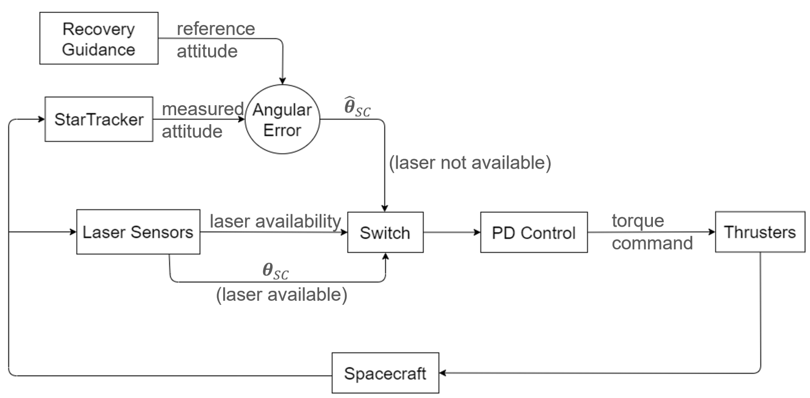

Figure 7.7: General architecture of the Spacecraft attitude recovery controller

7.3.2 TM position controller

The design for the TM position controller starts directly from a PID control law, that showed to be effective for the Spacecraft's attitude control.

The actuators that affect the quantities $\boldsymbol{r}_{\mathrm{m}_j}$ are the two GRS and the linear force of the MPS, thus a total of three different 3–dimensional PID controllers are needed.

Actually, the linear momentum transferred to the Spacecraft during the impact, causes an acceleration on the Spacecraft, that in turn generates another apparent acceleration on the relative positions between the TMs and the SC itself. For this reason the controllers that handle the linear force of the MPS thrusters will compensate the average TM position $\boldsymbol{r}_{\mathrm{m}}^{+} = \frac{1}{2}\left(\boldsymbol{r}_{\mathrm{m}_1} + \boldsymbol{r}_{\mathrm{m}_2}\right)$ by moving the SC itself. Whereas, the controllers that handle the two GRS will compensate the differential TM position $\boldsymbol{r}_{\mathrm{m}}^{-} = \frac{1}{2}\left(\boldsymbol{r}_{\mathrm{m}_1} - \boldsymbol{r}_{\mathrm{m}_2}\right)$, by actuating the TMs directly.

The PID controllers used are all discrete–time in parallel form, with filtered differentiation. The Z transfer function is

$$C(z) = \mathrm{P} + \mathrm{I}\,\tau\,\frac{1}{z-1} + \mathrm{D}\,N\,\frac{z-1}{z-1+N\,\tau}$$

where τ is the time interval of the controller, $\tau = 0.1\,\mathrm{s}$ for the MPS controllers and $\tau = 0.01\,\mathrm{s}$ for the GRS controllers.

In order to tune all the PID controllers, the Simulink PID Tuner was employed on the linearized plant. The settings used were maximum response speed and robustness. The parameters found were the following:

- for the MPS force controllers $\mathrm{P} = \begin{bmatrix}225 & 225 & 195\end{bmatrix}^\top$, $\mathrm{I} = \begin{bmatrix}3 & 3 & 2.5\end{bmatrix}^\top$ and $\mathrm{D} = \begin{bmatrix}3847 & 3847 & 3330\end{bmatrix}^\top$;
- for the GRS1 force controllers $\mathrm{P} = \begin{bmatrix}-200 & -200 & -200\end{bmatrix}^\top$, $\mathrm{I} = \begin{bmatrix}-2 & -2 & -2\end{bmatrix}^\top$ and $\mathrm{D} = \begin{bmatrix}-3500 & -3500 & -3500\end{bmatrix}^\top$;
- for the GRS2 force controllers $\mathrm{P} = \begin{bmatrix}200 & 200 & 200\end{bmatrix}^\top$, $\mathrm{I} = \begin{bmatrix}2 & 2 & 2\end{bmatrix}^\top$ and $\mathrm{D} = \begin{bmatrix}3500 & 3500 & 3500\end{bmatrix}^\top$.

Figure 7.8 shows the result for the simulation of meteoroid with id 1, that is one of the strongest impacts in the dataset, where the impact happens after 100 s.

The general architecture of the Test Mass position recovery controller is shown in Figure 7.9.

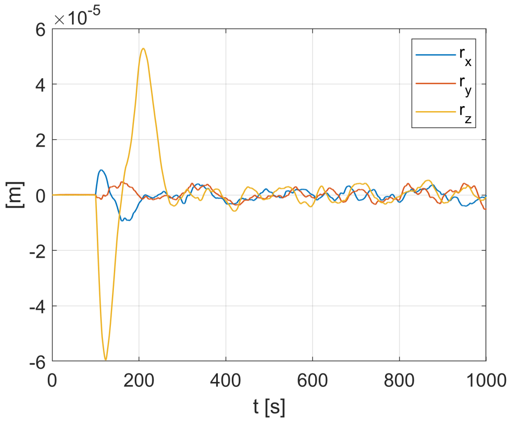

(a) TM1 position

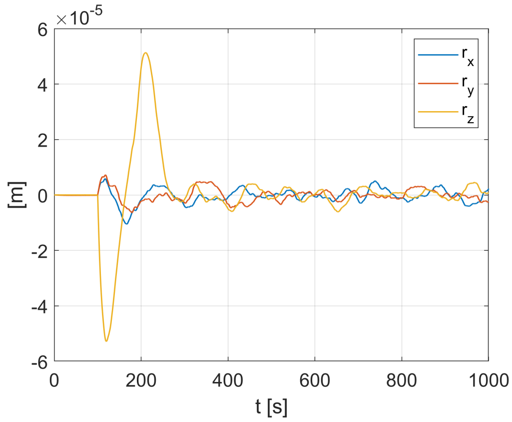

(b) TM2 position

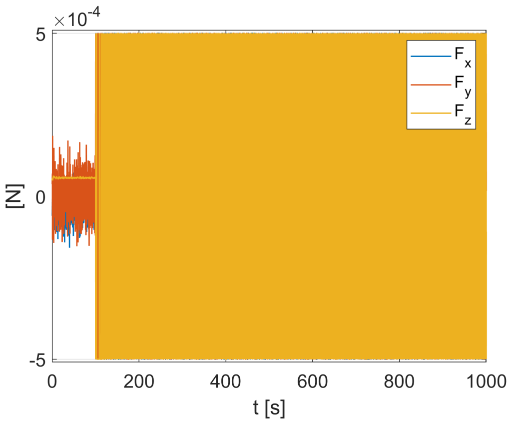

(c) Force requested to the MPS

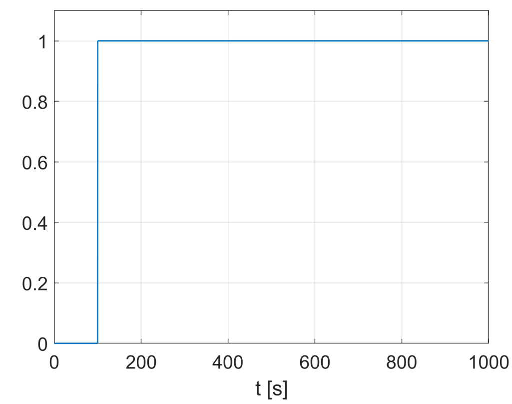

(d) Recovery R2 activation

Figure 7.8: Simulation of the TM pos. rec. controller

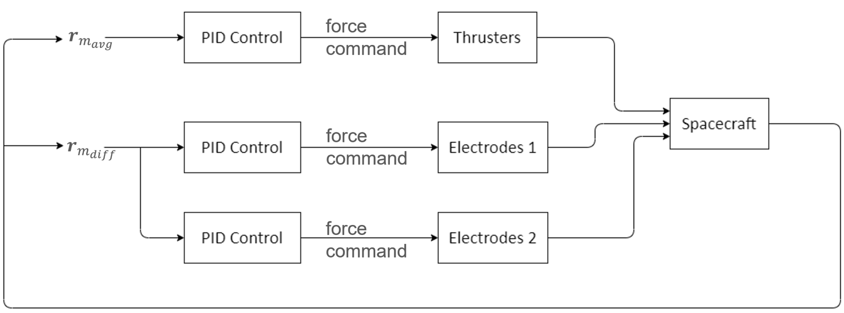

Figure 7.9: General architecture of the TM position recovery controller

7.4 EoR Detection

The End of Recovery detection is the task of determining online when a specific recovery controller has successfully accomplished the recovery phase and can be switched back to the DFAC System.

In particular, only tasks R1 and R2 need to perform EoR detection, because only these two have a specific controller.

The mechanism is the same for impact detection, that is, a threshold based system. A main difference is that in this scenario both the position and the velocity have to satisfy some constraints on their norm, in order to allow the switch back.

In order to determine the value of the angular position and velocity thresholds, the 89 impacts that make the SC attitude go divergent are used in a series of simulations to determine the steady state average of the norms of attitude angular error θ_{SC} and attitude error angular velocity $\boldsymbol{\omega}_{\mathrm{SC}}$. The final EoR rule is

$$|\theta_{\mathrm{SC}}| \leq 2.1 \cdot 10^{-6}\,\mathrm{rad} \wedge \|\boldsymbol{\omega}_{\mathrm{SC}}\|_2 \leq 2 \cdot 10^{-6}\,\mathrm{rad/s} \implies \text{End of R1 task}$$

The same procedure is repeated for the EoR of the R2 recovery of the TMs. A simulation for each of the 96 impacts that make the TMs divergent is performed and the steady state average values of the TMs positions $\boldsymbol{r}_{\mathrm{m}_j}$ and velocities $\boldsymbol{v}_{\mathrm{m}_j}$ are used as thresholds. The final EoR rule is

$$\left\|\boldsymbol{r}_{\mathrm{m}_j}\right\|_2 \leq 3.56 \cdot 10^{-6}\,\mathrm{m} \wedge \left\|\boldsymbol{v}_{\mathrm{m}_j}\right\|_2 \leq 2.14 \cdot 10^{-7}\,\mathrm{m/s},\ j = 1, 2 \implies \text{End of R2 task}$$

7.5 Configuration without CAS Sensor

As already mentioned at the beginning of this Chapter, it is possible to remove the CAS sensor and still perform the recovery maneuver (described as Configuration 2).

When the CAS sensor is removed the only remaining laser sensors are the DWS sensors. These are almost immediately lost after the strongest impacts, requiring the Star Tracker measurements to be used in combination with the same EKF of Configuration 1.

Simulations show that the spacecraft attitude is not going back to the working point if no CAS sensor is present. This is visible by comparing the spacecraft attitude error obtained from the recovery controller and CAS sensor, shown in Figure 7.10a, with the one obtained from the recovery controller without CAS, shown in Figure 7.10b, and also by comparing the laser beam deviations for the same configurations, respectively in Figure 7.11a and Figure 7.11b.

The recovery system without CAS is not able to return within the 2 μrad error required to reacquire the DWS sensors. The reason is that the solar pressure is not accounted for in the EKF model of the SC's attitude dynamics. This causes over time a steady–state offset in the angular prediction between the filtered value $\hat{\mathfrak{q}}_{\mathrm{SI}}$, coming from the EKF, and the real attitude $\mathfrak{q}_{\mathrm{SI}}$. This effect is shown in Figure 7.12a. Nonetheless, by adding a model of torque exerted on the Spacecraft's center of mass by the solar pressure to the EKF filter, this offset is greatly reduced, Figure 7.12b.

By adding this model, thus removing the constant offset in the filter's prediction, the performance is greatly improved and the recovery controller can be used to return to drag–free mode.

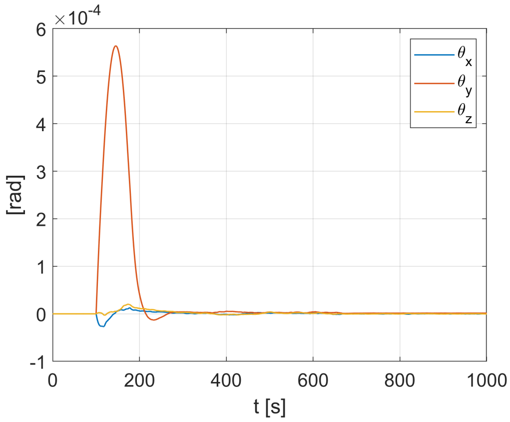

(a) Configuration 1

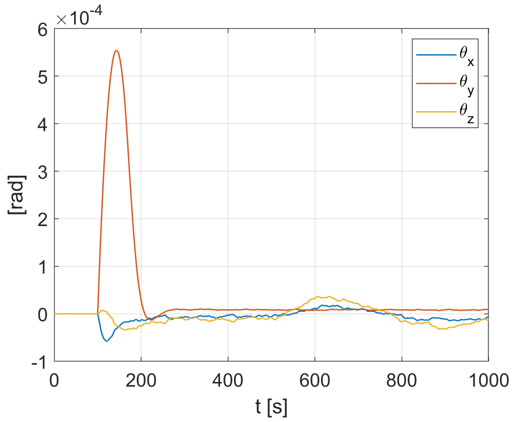

(b) Configuration 2

Figure 7.10: Spacecraft attitude error comparison

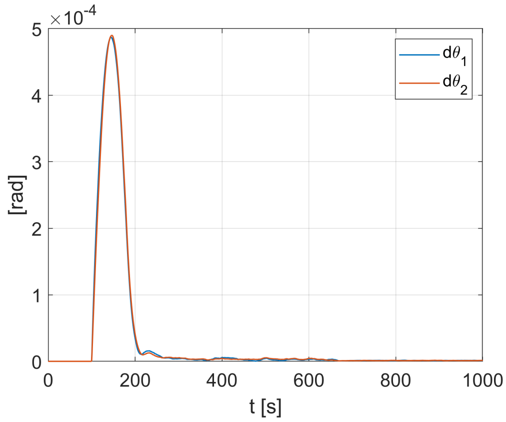

(a) Configuration 1

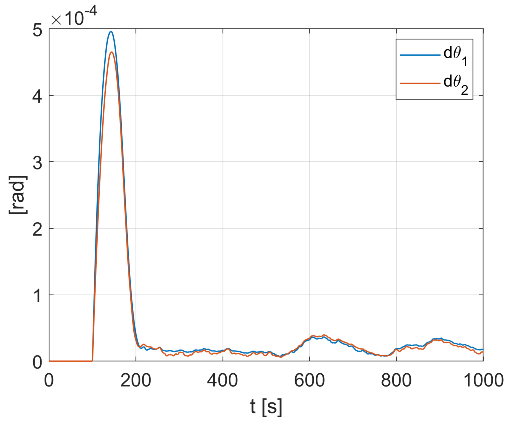

(b) Configuration 2

Figure 7.11: Laser beam deviation angle comparison

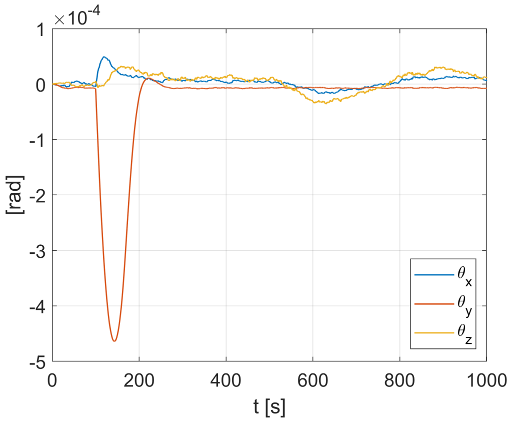

(a) No solar pressure model

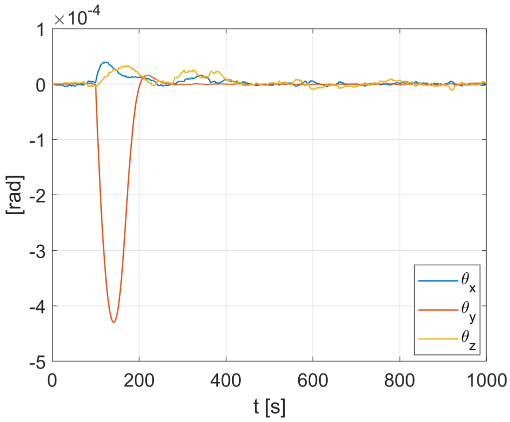

(b) With solar pressure model

Figure 7.12: Error in the EKF filtering of $\mathfrak{q}_{SI}$

8 | Simulation Results

In this chapter first the recovery system is shown in action with two of the strongest impacts available in the ESA dataset. Finally the results of a Monte Carlo simulation campaign are reported.

8.1 Single impact simulations

The first impact that is shown in Figure 8.2 is characterized by the following features: impact id 1, $\boldsymbol{p}_i = \begin{bmatrix}-2.5 & -0.9 & 14.9\end{bmatrix}^\top \cdot 10^{-3}\,\mathrm{Ns}$, $\boldsymbol{H}_i = \begin{bmatrix}-4 & 19.9 & 0.6\end{bmatrix}^\top \cdot 10^{-3}\,\mathrm{Nms}$ and $\boldsymbol{r}_i^{\mathrm{S}} = \begin{bmatrix}-1.421 & -0.301 & 0.528\end{bmatrix}^\top\,\mathrm{m}$. The impact instant is $t_i = 100\,\mathrm{s}$.

In the plot of Figure 8.2a the attitude error of the spacecraft with respect to the correct orientation is represented as a rotation vector $\boldsymbol{\theta}_{\mathrm{SC}}$. In the plot of Figure 8.2b the two deviation angles of each of the laser beams are shown. Each deviation angle represents the acute angle between the incoming laser beam and the longitudinal axis of the optical assembly (x axis in the ORF).

An additional simulation is shown in Figure 8.3 of another impact with features: impact id 2, $\boldsymbol{p}_i = \begin{bmatrix}-2.02 & -5.7 & -14.94\end{bmatrix}^\top \cdot 10^{-3}\,\mathrm{Ns}$, $\boldsymbol{H}_i = \begin{bmatrix}19.76 & -0.78 & -2.38\end{bmatrix}^\top \cdot 10^{-3}\,\mathrm{Nms}$ and $\boldsymbol{r}_i^{\mathrm{S}} = \begin{bmatrix}0.02 & -1.1 & 0.57\end{bmatrix}^\top\,\mathrm{m}$. The impact instant is $t_i = 100\,\mathrm{s}$.

8.2 Monte Carlo campaign

The Monte Carlo campaign validation process consists in performing a complete simulation for each impact in the dataset that causes at least one LISA state transition (236 impacts) and analyzing the results.

The first parameter that is evaluated is the success rate, that is the percentage of impacts whose simulation ended without instabilities and with the system back to science mode. The success rate after these simulations is 100%.

Another set of parameters focuses on the correct or wrong activation of the recovery tasks R1 and R2. The average number of times the impact detection triggers correctly a SC divergence is 12, with the maximum as high as 31 times. This happens because sometimes the attitude parameters will temporarily activate the threshold for impact detection, causing the activation of a recovery task, and then will oscillate triggering in sequence the EoR thresholds and again the impact detection thresholds. Such a behaviour can be seen in Figure 8.1; only by zooming the time scale in the detection area the fast oscillations can be noticed.

To overcome this problem, a simple solution adopted in this work is to have a 2 min timer start whenever the detection transitions from convergent to divergent. With this

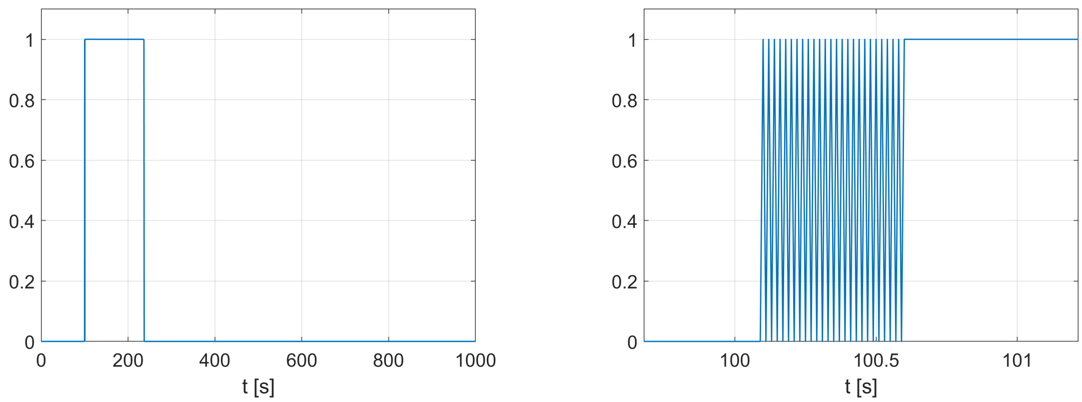

Figure 8.1: Impact detection oscillatory behavior

solution, every time there is an impact that causes SC attitude divergence, the impact detection will only trigger the recovery signal once.

The number of impacts for which the spacecraft attitude was convergent but the impact detection triggered nonetheless (false positives) is 6. The number to be expected was much higher, according to the number of false positives of the threshold ω^*_{SC} discussed in Section 7.1. This means that adding appropriate sensor management and tuning of the state observers had a positive effect on the impact detection.

The number of misses of the TM detection and SC detection is 0. This is in accordance with the number found during threshold tuning (Section 7.1) and with the safety rule of zero false negatives.

The last important performance parameter obtained from the final set of simulations is the total time required to complete the recovery maneuver: the average time was 5.78 minutes, with a minimum of 83.16 seconds and a maximum of 12.15 minutes.

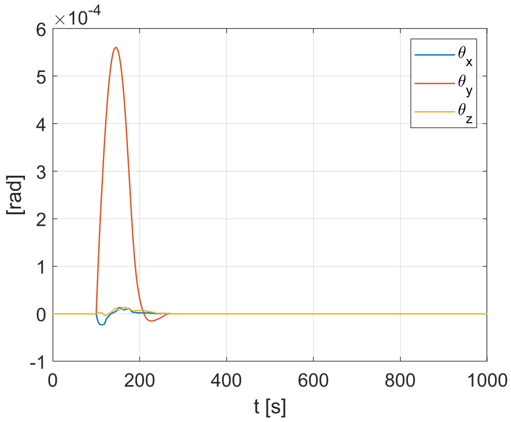

(a) SC Attitude error

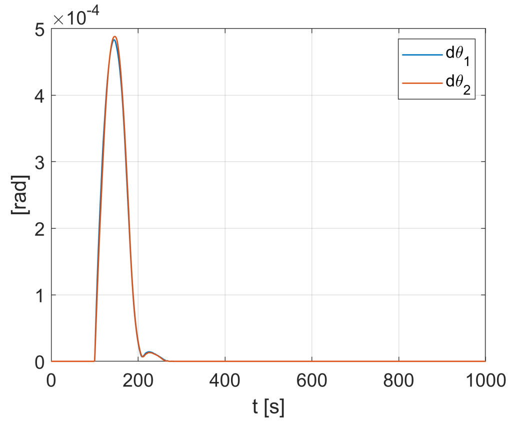

(b) Laser beams angular deviations

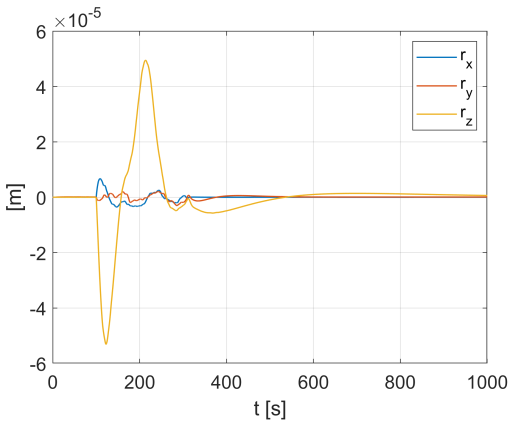

(c) TM1 position

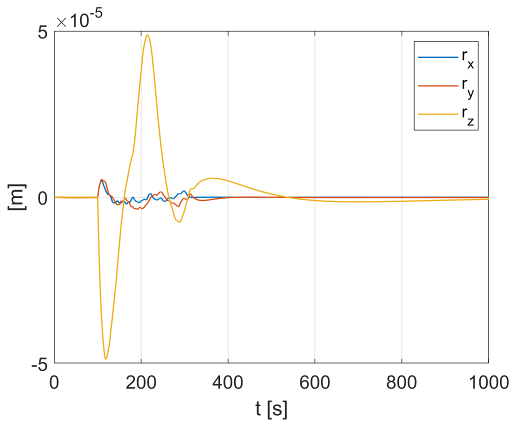

(d) TM2 position

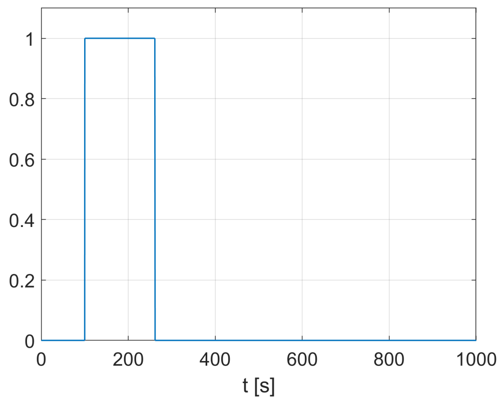

(e) SC attitude recovery signal

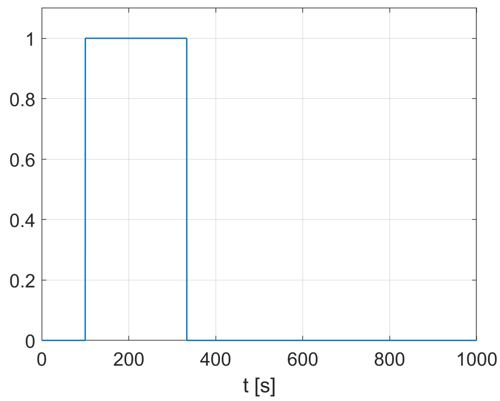

(f) TM position recovery signal

Figure 8.2: Recovery system simulation for impact 1

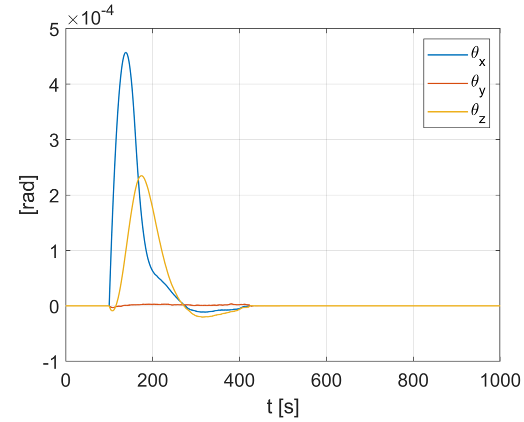

(a) SC Attitude error

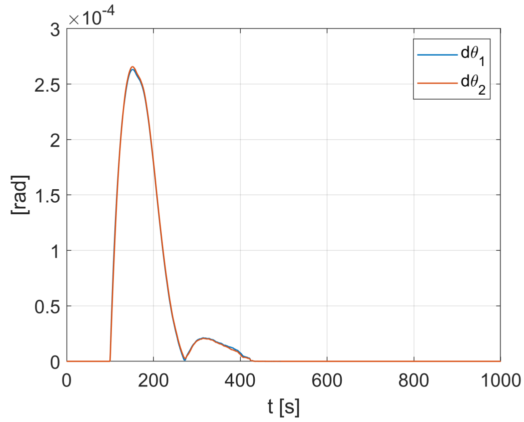

(b) Laser beams angular deviations

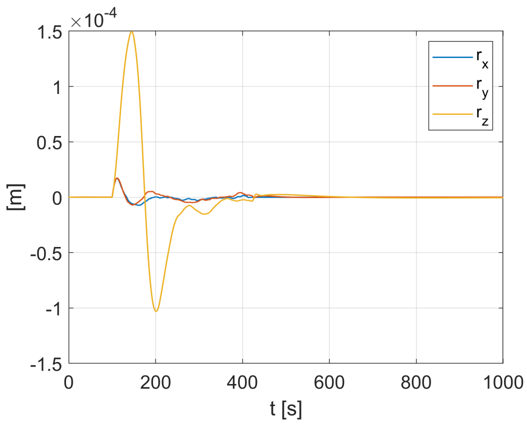

(c) TM1 position

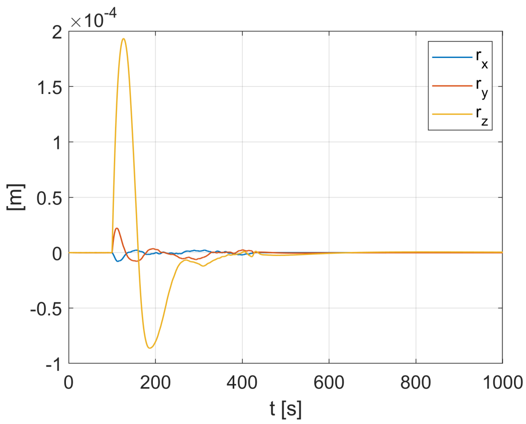

(d) TM2 position

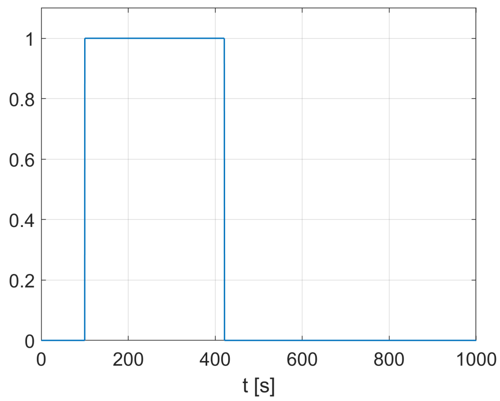

(e) SC attitude recovery signal

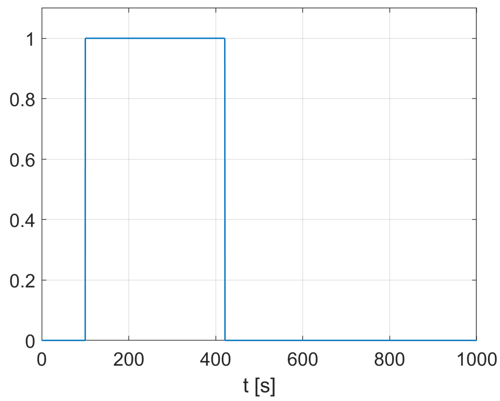

(f) TM position recovery signal

Figure 8.3: Recovery system simulation for impact 2

9 | Conclusions

In this Thesis the problem of designing a recovery control system for the LISA space mission has been addressed. First a preliminary analysis of the meteoroid impacts was performed, analyzing all the possible states in which the spacecrafts may find themselves in and the outcomes naturally led to the definition of the main recovery tasks to be implemented in the recovery system. Some of these recovery tasks were easily implemented by means of simple sensor management, but for the main two, Spacecraft attitude control and Test Mass position control, additional specific controllers were needed.

The control design for the Spacecraft attitude started from an already developed and tuned sliding mode controller employed for the Constellation Acquisition phase, and was simplified down to a PD control law, with the tuning automatically obtained from the previous one. This suggested that simple PID control laws could be effective also for Test Mass position control, given that during science mode the spacecraft's state is near the working point, where it behaves almost linearly.

Finally, a set of simulations with the most problematic impacts was performed and some interesting parameters were tracked. This confirmed the effectiveness of the recovery system, specifically it showed a great reduction in the time needed to complete the maneuver with respect to the time needed for the complete laser link reacquisition maneuver. This was the main problem that motivated this study.

Additionally, it was also shown that the same maneuver can be carried out even without the CAS sensor, one of the already few sensors available on board. This can be done at the cost of needing an accurate model of the solar pressure torque acting on the Spacecraft's center of mass.

Further work could be carried out focusing on ways to estimate the nominal reference for the spacecraft's attitude during the recovery maneuver, when the laser sensors are no longer available. This work relied on offline orbital simulations, but accurate enough data could be difficult to obtain by these means. Instead online estimation of the spacecraft's orbit, speed and acceleration could result in more reliable control. These estimation techniques could then simply be integrated into the recovery system proposed here.

A | Mathematical Notation

A.1 Basic Notation

In this work extensive use of abstract vectors was made. Basic abstract vectors are represented using **bold** font:

$$\mathbf{v} = \begin{bmatrix} \mathrm{v}_1 \\ \vdots \\ \mathrm{v}_\mathrm{n} \end{bmatrix}, \quad \mathbf{v} \in \mathbb{R}^\mathrm{n}$$

When the abstract vector is represented with respect to a reference frame, the reference frame is put as an apex. Other information regarding the quantity represented by the vector is put as a subscript. For example, a vector $\mathbf{r} \in \mathbb{R}^3$, that represents the spacecraft's position in the IRF, expressed in the Spacecraft Reference Frame, would appear like this:

$$\mathbf{r}^{\mathrm{S}}_{\mathrm{SI}}$$

The component-wise product between two vectors **a** and **b** is defined as

$$\mathbf{a} * \mathbf{b} = \begin{bmatrix} \mathrm{a}_1\,\mathrm{b}_1 \\ \vdots \\ \mathrm{a}_\mathrm{n}\,\mathrm{b}_\mathrm{n} \end{bmatrix}$$

A.2 Quaternions

Every rotation quaternion is expressed with a particular font and style. The **bold** font is used to remember that it is still a vector, of 4 components in this case, and all useful information are shown as subscript.

$$\boldsymbol{\mathfrak{q}} = \begin{bmatrix} \mathrm{q}_0 \\ \mathbf{q} \end{bmatrix}, \quad \boldsymbol{\mathfrak{q}} \in \mathbb{R}^4, \quad \mathrm{q}_0 \in \mathbb{R}, \quad \mathbf{q} \in \mathbb{R}^3$$

where q_0 is the quaternion *scalar part*, and $\mathbf{q}$ is the *vector part*. Notice the difference between the quaternion $\boldsymbol{\mathfrak{q}}$ and the quaternion vector part $\mathbf{q}$.
The conjugate of a quaternion $\boldsymbol{\mathfrak{q}}^*$ is defined as

$$\boldsymbol{\mathfrak{q}}^* = \begin{bmatrix} \mathrm{q}_0 \\ -\mathbf{q} \end{bmatrix}$$

To obtain the DCM matrix corresponding to a given quaternion:

$$T(\boldsymbol{\mathfrak{q}}) = \begin{bmatrix} \mathrm{q}_0^2 + \mathrm{q}_1^2 - \mathrm{q}_2^2 - \mathrm{q}_3^2 & 2\,(\mathrm{q}_1\,\mathrm{q}_2 - \mathrm{q}_0\,\mathrm{q}_3) & 2\,(\mathrm{q}_1\,\mathrm{q}_3 + \mathrm{q}_0\,\mathrm{q}_2) \\ 2\,(\mathrm{q}_1\,\mathrm{q}_2 + \mathrm{q}_0\,\mathrm{q}_3) & \mathrm{q}_0^2 - \mathrm{q}_1^2 + \mathrm{q}_2^2 - \mathrm{q}_3^2 & 2\,(\mathrm{q}_2\,\mathrm{q}_3 - \mathrm{q}_0\,\mathrm{q}_1) \\ 2\,(\mathrm{q}_1\,\mathrm{q}_3 - \mathrm{q}_0\,\mathrm{q}_2) & 2\,(\mathrm{q}_2\,\mathrm{q}_3 + \mathrm{q}_0\,\mathrm{q}_1) & \mathrm{q}_0^2 - \mathrm{q}_1^2 + \mathrm{q}_2^2 + \mathrm{q}_3^2 \end{bmatrix}$$

From the DCM it is possible to transform a quaternion $\mathfrak{q}$ to a rotation vector $\boldsymbol{\theta}$ by the following relationships:

$$
\begin{aligned}
\phi &= \texttt{atan2}(T_{3,2},\, T_{3,3}) \\
\theta &= \texttt{atan2}(-T_{3,1},\, \sin(\phi)\, T_{3,2} + \cos(\phi)\, T_{3,3}) \\
\psi &= \texttt{atan2}(-\cos(\phi)\, T_{1,2} + \sin(\phi)\, T_{1,3},\, \cos(\phi)\, T_{2,2} - \sin(\phi)\, T_{2,3}) \\
\boldsymbol{\theta} &= \begin{bmatrix} \phi \\ \theta \\ \psi \end{bmatrix}
\end{aligned}
$$

The quaternion product $\otimes$ can be also expressed with a matrix:

$$
\mathfrak{q}\otimes = Q = \begin{bmatrix} q_0 & -q_1 & -q_2 & -q_3 \\ q_1 & q_0 & -q_3 & q_2 \\ q_2 & q_3 & q_0 & -q_1 \\ q_3 & -q_2 & q_1 & q_0 \end{bmatrix}
$$

Bibliography

[1] A. Schleicher et al. "In-Orbit Performance of the LISA PAthfinder Drag Free and Attitude Control System". In: *Proceedings of the 10th International ESA Conference on Guidance Navigation & control Systems* (2017).

[2] Abadie et al. *Search for Gravitational Waves from Low Mass Compact Binary Coalescence in LIGO's Sixth Science Run and Virgo's Science Runs 2 and 3*. 2011. URL: `https://arxiv.org/abs/1111.7314`.

[3] C. Novara et al. "Assessment and Preliminary Prototyping of a Drag Free Control System for the L3 Gravity Wave Observatory". 2020.

[4] D. Gerardi et al. "Advanced drag-free concepts for future space-based interferometers: acceleration noise performance". In: *The Review of scientific instruments, AIP* (2014).

[5] J. I. Thorpe et al. "LISA Pathfinder as a Micrometeoroid Instrument". In: 840 012007. IOP Conference, 2017.

[6] J. I. Thorpe et al. "Micrometeoroid Events in LISA Pathfinder". In: *The Astrophysical Journal* (2019), p. 15.

[7] P. Amaro-Seoane et al. *Laser Interferometer Space Antenna*. 2017. URL: `https://arxiv.org/abs/1702.00786`.

[8] S. M. Merkowitz et al. "Self-Gravity Modelling for LISA". In: *Classical and Quantum Gravity 22* (2005).

[9] S. Vidano et al. "The LISA DFACS: A Nonlinear Model for the Spacecraft Dynamics". In: *Aerospace Science and Technology* (2020).

[10] T. Ziegler et al. "Test Mass Stiffness Estimation for the LISA Pathfinder Drag-Free System". In: *Proceedings of the AIAA Guidance, Navigation and Control Conference and Exhibit* (2007).

[11] F. Cirillo. "Controller design for the acquisition phase of the LISA mission using a Kalman Filter". In: *University of Pisa, Thesis, etd-06202007-101808* (2007).

[12] ESA. *LISA PHASE 0 CDF STUDY - INTERNAL FINAL PRESENTATION*. 2017. URL: `https://sci.esa.int/web/lisa/-/59336-lisa-internal-phase-0-cdf-study-final-presentation`.

[13] ESA. *Statement of Work: Appendix 1 to ESA ITT 1-9100/17/NL/CRS*. 2017.

[14] R. M. Georgevic. *Mathematical Model of the Solar Radiation Force and Torques Acting on the Components of a Spacecraf*. NASA, Oct. 1971. URL: `https://ntrs.nasa.gov/api/citations/19720004068/downloads/19720004068.pdf?attachment=true`.

[15] Leonardo – Finmeccanica M. Molina et al. “Cold Gas Micropropulsion in-orbit performances LISA Pathfinder and Microscope”. In: *Astronautical Congress, Guadalajara, Mexico* (2016).

[16] E. Plagnol. “LISA Pathfinder μ-Thruster System: What we have learnt”. In: *APC Paris* (2017).

[17] Yuri Shtessel et al. “Sliding Mode Control and Observation”. In: Birkhäuser, 2014. Chap. 2.

[18] TERMA. *Star Tracker HE–5AS Datasheet*. 2012.